



**Characterizing the Exhaust Plume of the Three-Electrode
Micro Pulsed Plasma Thrusters**

THESIS

Seo Myeongkyo, Captain, ROKAF

AFIT/GSS/ENY/09-M07

DEPARTMENT OF THE AIR FORCE

AIR UNIVERSITY

AIR FORCE INSTITUTE OF TECHNOLOGY
Wright-Patterson Air Force Base, Ohio

APPROVED FOR PUBLIC RELEASE; DISTRIBUTION UNLIMITED

The views expressed in this thesis are those of the author and do not reflect the official policy or position of the United States Air Force, Department of Defense, or the U.S. Government.

AFIT/GSS/ENY/09-M07

**CHARACTERIZING THE EXHAUST PLUME OF THE THREE-ELECTRODE MICRO
PULSED PLASMA THRUSTERS**

THESIS

Presented to the Faculty

Department of Aeronautical and Astronautical Engineering

Graduate School of Engineering and Management

Air Force Institute of Technology

Air University

Air Education and Training Command

In Partial Fulfillment of the Requirements for the

Degree of Master of Science in Astronautical Engineering

Seo Myeongkyo

Captain, ROKAF

March 2009

APPROVED FOR PUBLIC RELEASE; DISTRIBUTION UNLIMITED

**CHARACTERIZING THE EXHAUST PLUME OF THE THREE-ELECTRODE
MICRO PULSED PLASMA THRUSTERS**

Seo Myeongkyo

Captain, ROKAF

Approved:

Richard D. Branam, LtCol USAF (Chairman)

Date

Richard E. Huffman, Maj USAF (Member)

Date

Dr. William A. Hargus Jc (Member)

Date

Abstract

There are several kinds of space propulsion device such as arcjets, Hall thrusters, ion thrusters and magnetoplasma dynamic thrusters (MPD). They all have their own ranges of performance measured as efficiency, specific impulse and thrust. The magnetoplasma dynamic thrusters have the potential to generate high levels of thrust at very high specific impulses but require a relatively massive power supply. To provide this performance without the penalty of a heavy power supply, these devices are often employed as pulsed plasma thrusters. The pulsed plasma thruster (PPT) is an electric propulsion device using electric power to ionize and electromagnetically accelerate plasma to high exhaust velocity providing the high specific impulse levels, typically using polytetraflouoroethalene (PTFE). PTFE has the advantage of being inert and nontoxic, giving the PPT system an additional benefit of being one of the safest propulsion systems for spacecraft. This research investigated the plume characteristics of a new PPT design, three-electrode micro PPT developed recently by AFRL. The one tested here has a 3.175 mm (1/8") diameter tube. There are three major benefits of using a three-electrode micro PPT. The most important benefits include minimal shot to shot variations, decreasing required voltage and increased controllable firing frequency. Using three concentric electrodes provides very precise impulse bits with a great degree of operability. The thruster was put in a vacuum chamber capable of pressure level as low as 10^{-8} torr to simulate satellite operating environments in space. The importance of studying

micro PPTs is directly related to the satellite design trend toward developing smaller space vehicles, which require precise impulse-bits.

In characterizing these thrusters, particulate velocities in the plume were measured using a stereoscopic approach to get accurate velocity and divergence information. This information directly applies to the performance of these thrusters. Both velocity and angle data were analyzed for normal distributions at each thruster operating condition. The velocity and angle distributions are also compared between operating conditions identifying the energy effect on these distributions. The results show that the three-electrode micro-PPT is more reliable than two-electrode micro-PPT and the operating energy range from 2 to 4.5 Joule is proper value to operate it. This research also shows that the angle distribution is similar to previous mass deposition distributions and the faster particles have shallower angles than that of slower particles. Finally, the energy did not give appreciable effect on angle and velocity distributions and have the Isp value range from 25 to 35 sec of the large particles from the average exit velocity.

Acknowledgments

Most of all, I sincerely appreciate to my thesis advisor, Lt Col Richard Branam for his guidance whenever I encounter the trouble during the research. I also give my thanks to AFIT lab staff, Jay Anderson, Christopher Zickefoose, Wilbur Lacy and Sean Miller for their effort to help me when dealing the lab apparatus. Finally, I've got unique opportunity to get my honorable master's degree because of R.O.K Air Force and my family.

Seo Myeongkyo

Table of Contents

	Page
Abstract	iv
Acknowledgments.....	vi
Table of Contents	vii
List of Figures	x
List of Tables	xiii
I. Introduction	1
I.1. Background.....	1
I.2. Problem Statement.....	2
I.3. Research Objectives/Questions/Hypotheses.....	3
I.4. Methodology.....	3
I.5. Preview	3
II. Literature Review	5
II.1. Chapter Overview.....	5
II.2. History of PPT	5
II.3. Comparison of a standard PPT with micro-PPT (two and three-electrode design)	7
II.4. Optimization issue and modeling for micro PPT	12
II.5. Measuring the Particle velocity and angle distribution of the two-electrode micro-PPT.....	13
II.6. Contamination issue for two-electrode micro-PPT	18
III. Methodology	24
III.1. Chapter Overview	24

III.2.	Vacuum Chamber	24
III.3.	Experimental Setup.....	30
III.3.1.	Power Supply	32
III.3.2.	High Voltage Converter	33
III.3.3.	High Voltage Pulse.....	35
III.3.4.	Wave Form Generator, Synchronization.....	36
III.3.5.	High Speed Cameras	38
III.3.6.	Three-Electrode micro-PPT Tube	42
III.4.	Data Evaluation Method	44
III.4.1.	Determining 3D Velocities.....	47
IV.	Analysis and Results	49
IV.1.	Chapter Overview	49
IV.2.	Operating Energy Range for the Three-electrode micro-PPT	49
IV.3.	Captured Particles	50
IV.4.	Angle Error Correction for Tilted Thruster	57
IV.5.	Velocity Distribution	61
IV.5.1.	Comparing 3D Velocity Distributions with Previous 2D Velocity Distributions.....	61
IV.5.2.	Compare Velocity Distribution with Each Energy Level	64
IV.5.3.	Performance Contributions	66
IV.6.	Angle Distribution	66

IV.6.1.	Comparing Solid Angle (3D) with 2D Angle Distribution	68
IV.6.2.	Comparing Solid Angle Distribution With Different Energy Levels	72
IV.6.3.	Average Velocity Versus Angle Range	74
IV.7.	Summary	76
V.	Conclusions and Recommendations.....	78
V.1.	Overview	78
V.2.	Conclusions	78
V.2.1.	Operability	78
V.2.2.	Velocity and Angle Distribution.....	78
V.2.3.	Performance contribution.....	79
V.2.4.	Energy Effect on Angle and Velocity Distribution.....	79
V.3.	Recommendations	79
V.3.1.	Operability and Circuit Design	79
V.3.2.	Capturing the Particles	80
V.3.3.	Velocity Distributions and Performance Contribution	80
V.3.4.	Angle Distributions	81
	Vita	98
	Bibliography	99

List of Figures

	Page
Figure 1: Standard Pulsed Plasma Thruster	11
Figure 2: Two-electrode micro-PPT ⁷	11
Figure 3: Three-electrode micro-PPT ⁷	12
Figure 4: Consecutive Images Taken at 15400 fps and 20 μ s Exposure Time.....	14
Figure 5: Velocity and Angle Measurements from Images	14
Figure 6: Particle Velocity (Magnitude) Distribution 35 μ s	15
Figure 7: Velocity (Magnitude) Distribution for All Particles	15
Figure 8: Normal Distribution for Particle Angles	16
Figure 9: Angular Distribution for Slow Particles, < 300 m/s.....	17
Figure 10: Angular Distribution for Fast Particles, > 500 m/s.	18
Figure 11: Particle Travel Progress at 28500 fps and 16 μ sec of Exposure Time.....	18
Figure 12: Bowl-shaped Witness Plate Holder	19
Figure 13: Particle size vs. Normalized Particle Count	20
Figure 14: Mass Contribution of Each Particle Size for Various Angular Positions.....	21
Figure 15: Mass Deposition Profile	22
Figure 16: Deposition Rates per Pulse per Steradian.....	22
Figure 17: LabView Operation Panel	25
Figure 18: LabView Operation Panel After Activation.....	25
Figure 19: Turbo Pump Ready.....	26
Figure 20: Vacuum Chamber Initial Pump Down Configuration.....	26

Figure 21: Crossover Pressure Set Point Operation.....	27
Figure 22: Reaching a Set Point.....	28
Figure 23 : GNAT Vacuum Chamber #2 Front View	28
Figure 24: GNAT Vacuum Chamber #2 Back and Side View	29
Figure 25: Relationship of Collector Current and Pressure	30
Figure 26: Test setup.....	31
Figure 27: Agilent E3631A Triple Output DC Power Supply.....	33
Figure 28: Relationship Between Power Supply and High voltage converter.....	34
Figure 29 : Emco Amplifier F series.....	35
Figure 30: High Voltage Pulse, M10k-20 (Front and Rear View)	36
Figure 31: The Agilent 33120A Function Generator.....	37
Figure 32: Comparison Between Original and 90 Degrees Turned Camera Set	40
Figure 33: Cable Connection to High-Speed Camera.....	41
Figure 34: AF Micro-NIKKOR 60mm f/2.8D Lens.....	42
Figure 35 : 3.175 mm (Diameter) Three-electrode micro-PPT Tube	43
Figure 36 : Circuit using two $1\mu\text{F}$ Capacitors Connected and High Voltage Converter ..	44
Figure 37 : Measuring the Physical Length Scale	45
Figure 38: Measuring the Particle Streak Length	48
Figure 39: Three Consecutive Frame at 14,100 fps 40 μsec	54
Figure 40 : Different Focusing Plane (8V 26,500 fps 30 μsec).....	54
Figure 41 : Fast Particles at Each Operating Condition.....	56
Figure 42: Fast Particles.....	57

Figure 43 : Angle Definitions	59
Figure 44 : Velocity Component in Thruster Coordinates.....	60
Figure 45 : Velocity Distribution at 4V (2.2J).....	63
Figure 46 : Comparing Velocity Distribution With Each Energy Level.	65
Figure 47 : Solid angle calculation	67
Figure 48 : Angle distribution at 4V (2J).....	70
Figure 49 : Profile of ion density at 1 μ sec after firing.....	71
Figure 50 : Profile of plume from the main discharge of three-electrode micro PPT	72
Figure 51 : Comparing angle distribution with each energy level.....	74
Figure 52 : Average Velocity Versus Angle.....	75
Figure 53 : Standard Deviation Versus Angle	76
Figure 54: First screen of Motion Pro software when it opens.....	82
Figure 55: After selecting the “Cameras”	82
Figure 56: Screen after clicking the “open”	85
Figure 57 : Velocity Distribution for 5V (2.7 Joule)	87
Figure 58 : Velocity Distribution for 6V (3.4 Joule)	88
Figure 59 : Velocity Distribution for 7V (4 Joule)	90
Figure 60 : Velocity Distribution for 8V (4.5 Joule)	91
Figure 61 : Angle Distribution for 5V (2.7 Joule)	93
Figure 62 : Angle Distribution for 6V (3.4 Joule)	94
Figure 63 : Angle Distribution for 7V (4 Joule)	96
Figure 64 : Angle Distribution for 8V (4.5 Joule)	97

List of Tables

	Page
Table 1: PPT Programs	7
Table 2: micro-PPT operating condition.....	20
Table 3 : Relationship between power supply and high voltage converter	34
Table 4: High Voltage Pulse Generator Specifications	36
Table 5 : Output frequency	38
Table 6: Relationship Between Image Resolution and Max Frame rate	39
Table 7 : XS-4 Camera Specification	40
Table 8 : One pixel error (m/s) in each exposure time	46
Table 9 : Three-electrode micro-PPT Operability Test Results.....	50
Table 10 : Summary of Captured Particles	51
Table 11: Captured Particles Sorted by Frame Rate and Exposure Time.....	52
Table 12 : I_{sp} Contributions for Each Operating Conditions	66

CHARACTERIZING THE EXHAUST PLUME OF THE THREE-ELECTRODE MICRO PULSED PLASMA THRUSTERS

I. Introduction

I.1. Background

There are several kinds of space propulsion device such as arcjets, Hall thrusters, ion thrusters and magnetoplasma dynamic thrusters (MPD). They each have found their niche based primarily on their own specific performance; efficiency, specific impulse and thrust. The pulsed plasma thruster (PPT) is a magnetoplasma dynamic device relying on electronic pulsing to minimize the massive power system requirements of these types of devices. They use the electric power to ionize and electromagnetically accelerate plasma to high exhaust velocity providing the high specific impulse levels. Often, these devices use a solid propellant with polytetraflouoroethalene (PTFE) as a preferred material. PTFE has the advantage of being inert and nontoxic, giving the PPT system an additional benefit of one of the safest propulsion systems for spacecraft. Because of these advantages, PPTs have a long history of reliable space flight operation.¹ The first PPT flight was the Soviet Zond-2 spacecraft in 1964. In the United States, PPT development work for the present solid-state PTFE devices began in the 1960s and led to the first U.S. flight of a PPT aboard the Lincoln Experimental Satellite (LES 6) in 1970. The system performed flawlessly in an East–West station-keeping role over its five-year life. The success of the LES-6 led to consideration of the PPT for other missions. One such mission was the U.S. Navy's NOVA navigation satellites. PPTs were found to be well suitable to provide drag compensation for this mission. Three NOVA spacecraft were

launched between 1981 and 1988. Two PPT systems per spacecraft provided drag make-up propulsion for seven years on each of the three NOVA spacecraft in low earth orbit (LEO). In 1995, NASA Lewis Research Center (now Glenn Research Center) initiated a program with Primex Aerospace Co. (now Aerojet-Redmond Operations) to develop, fabricate, and flight qualify a PPT. The result is the Earth Observer-1 (EO-1) PPT, which performed flawlessly starting in February of 2001.

With the trend in satellite design towards small, low cost, satellite constellations, the need for miniaturizing the PPT (and other thruster systems) is apparent. The U.S. Air Force Research Lab (AFRL) at Edwards Air Force Base undertook an effort to miniaturize the pulsed plasma thruster (two electrode micro-PPT). Subsequently, the lab also developed a three-electrode design in a desire to reduce shot-to-shot variability in the self-triggered device. This design allows for the elimination of the external igniter necessary in two electrode designs. Much work has been accomplished to date to measure the characteristic of PPTs focusing on propellant consumption rate, plasma velocity, plasma density, temperature of propellant surface, and charred Teflon surfaces. These measures result in a means to predict performance in terms of specific impulse, efficiency and thrust.

I.2. Problem Statement

Three-electrode micro-PPTs are a new version of two electrode micro-PPTs devices as mentioned before. Performance predictions and contamination expectations are essential characteristics needed by satellite designers. In order to focus on the thruster specific impulse, thrust and efficiency, measuring the exhaust velocity or impulse bit and

propellant consumption rate is essential. While this is not always possible to measure directly, focusing on the ejected mass from the PPT provides significant information allowing determination of these performance statistics. Specifically, focusing on exhaust angle distribution and velocity of the exhaust particles is the emphasis of this work.

I.3. Research Objectives/Questions/Hypotheses

1. One of our objectives is to build and test three-electrode micro-PPT, vary input voltage to establish operating capabilities
2. Assess the velocity and angle of the particles leaving from a three-electrode micro-PPT and construct distribution functions of particle velocities and exit angles to allow for prediction of contamination and performance impacts
3. Figure out energy effect on velocity and angle distribution.

I.4. Methodology

The three-electrode micro-PPTs were put in a bell jar vacuum chamber. High speed imaging systems captured three dimensional images of the particles from the PPT's exhaust surface to determine velocity. To make a reliable three-electrode micro-PPT circuit, a high voltage pulse device is used to make seed ionization for the intermediate discharge. A function generator provided the signal to high voltage pulse and two cameras at the same time for firing the thruster and taking picture of three dimensional images.

I.5. Preview

The next chapter focuses on the background knowledge of the two and three electrode micro PPT designs and also shows previous tests for the two electrode micro PPT. In

chapter 3, equipment such as the vacuum chamber, high speed cameras, the function generator and the high voltage pulse are described in detail along with the experimental setup for this research. Chapter 4 shows the result of the three-electrode micro-PPT operability and velocity/angular distribution of the particles from the three-electrode micro-PPT design at the different operating conditions. This chapter points out differences in the results with operating condition. The last chapter presents the conclusion of this study and recommendations for future research.

II. Literature Review

II.1. Chapter Overview

In this chapter, we will present the history of PPTs and previous research. Introducing the differences between standard PPTs and micro PPTs is necessary for explaining the concept of a micro PPT and the unique utility of these devices. It is also useful to discuss relevant diagnostics used for PPTs to measure performance and plume characteristic.

II.2. History of PPT

Antropov and Khrabrov in the USSR developed two PPT designs, one with an electromagnetic and the other with a thermal acceleration mechanism.² The latter type proved practical and was the design for the PPT used on the Zond-2 spacecraft in 1964. The first U.S. satellite using PPTs for attitude control was LES-6 on Sept. 26, 1968. This flight unit was a breech-fed design providing $26\mu\text{N}$ of thrust at a specific impulse of 312 s. The success of the PPT on LES-6 led to other missions for these thrusters. In particular, the U.S. Navy's NOVA navigation satellites, operated between 1981 and 1988, using PPTs for drag compensation. The NASA Lewis Research Center (now Glenn Research Center) started a program with Primex Aerospace Co. (now Aerojet-Redmond Operations) to develop the Earth Observer-1 (EO-1) PPT, which performed flawlessly. Due to satellite design trends increasingly moving towards small, low cost, satellite constellations; miniaturizing the PPT (and other thruster systems) was needed. PPTs could be employed to provide formation keeping, maneuvering, orbit maintenance, and attitude control for smaller satellites.

A precise and predictable impulse bit is needed for microsatellites to support missions like formation flying, space based surveillance, space control, and on-orbit satellite servicing. In response to this need, the Air Force Research Laboratory developed a micro pulsed plasma thruster. Micro pulsed plasma thrusters have been developed and tested in two basic designs; triggered micro-PPT and self-triggered micro-PPT. The triggered micro-PPT uses a pulse of energy at the propellant face to drive a surface discharge. The self-triggering micro-PPT uses the high voltage directly to initiate the spark. The transition to a full surface discharge is through a surface breakdown. The triggered micro-PPT and the self-triggered micro-PPT reduced mass by a factor of about 10 and 60 from a standard PPT, respectively. The main failure of a triggered micro-PPT is the high voltage triggering switch. It can be protected through a cautious choice of circuit energy, voltage, and current but still tends to be a weak point in this design. Another major flaw in the triggered design is the occasional trend to gouge out a localized area of propellant. This results from having difficulty in evenly distributing the energy across the propellant face area. This flaw can lead to extra propellant usage. For these reasons, a self-triggering micro-PPT design has advantages as well as simpler electronics and lower mass.

AFRL has focused on propellant ablation rates suggesting the design criteria are to attain a desired steady-state propellant ablation characteristic. The discharge energy to surface area ratio and the current density at the inner electrode have to be sufficient to drive the PPT function properly. The micro-PPT efficiency turns out to be a trade-off between geometry (such as propellant area and inner electrode diameter) and discharge energy. These parameters directly affect the ablation rate characteristics.

While the lab initially developed these thrusters in-house, other work progressed to develop thrusters in the 100W range by CU Aerospace. Teamed with the University of Illinois at Urbana–Champaign and Unison Industries, the PPT-10 and PPT-10.1 were built relying on side-fed propellant systems. These coaxial pulsed plasma thrusters are based on the previous PPT-4 and PPT-7 thruster designs. These thrusters used energy levels between 40 and 80 J generating several mNs of thrust with a specific impulse of 800s. Table 1 presents PPT programs chronologically from Zond-2 in 1964 to Falconsat-3 in 2007.

Table 1: PPT Programs³

Program	Year	Energy	Voltage	Program	Year	Energy	Voltage
Zond-2	1964	50 J	1000 V	TIP-III	1976	20 J	1630 V
LES-6	1968	1.85 J	1360 V	NOVA-1	1981	20 J	1630 V
LES-7	~1970	20 J	?	ETS-IV	1981	2.25 J	1680 V
SMS	~1973	8.4 J	1450 V	MDT-2A	1981	4 J	2000 V
LES-8/9	~1973	20J(15J)	1370 V	NOVA-3	1984	20 J	1630 V
UAP-1	1974	30 J	1450 V	NOVA-2	1988	20 J	1630 V
UAP-2	1974	30 J	1450 V	EO-1	2000	8-56 J	<1700 V
LES-8/9	~1975	20 J	1530 V	Dawgstar	2002	5 J	2770 V
Millipound	1973-80	750 J	2500 V	AF μPPT	2003	1.25-6 J	2500-5400V
TIP-II	1975	20 J	1630 V	Falconsat 3⁴	2007	1.96J	-

II.3. Comparison of a standard PPT with micro-PPT (two and three-electrode design)

Both PPTs are electric propulsion devices utilizing electric power to ionize and accelerate a plasma electromagnetically using solid propellant. The standard PPT consists

of a bar of polytetraflouroethalene (PTFE) propellant, spring, power processing unit (PPU), capacitor, spark plug, anode and cathode (Figure 1). The spring pushes the propellant, the only moving part, to replenish when the propellant face is consumed. A PPU charges a capacitor to voltages using unregulated power from the spacecraft bus. The PPU also supplies a high voltage pulse to a spark plug, used for triggering the discharge. Once the discharge ignites, the energy stored in the capacitor feeds a high current plasma discharge. This discharge ablates and ionizes a small amount of the propellant face and accelerates it to high exhaust velocities using the Lorentz force⁵. The Lorentz force results from the current and the self-induced magnetic field, which can be expressed as below

$$F = qE' = q(E + v \times B) \quad (1)$$

F = Lorentz force (N)

q = Charge of moving particle (C)

E' = Effective electric field (V/m)

E = Applied electric field (V/m)

v = Velocity of particle (m/s)

B = Magnetic field (T)

The current-magnetic field interaction accelerates the ionized plasma. Another component of thrust comes from the thermal expansion of non-ionized vapor resulting in a much lower exhaust velocity.⁶ This exhaust flow is often considered a loss when

considering specific impulse as is the solid particulates exiting the PPT. An ideal thruster would completely vaporize and ionize all of the propellant.

Figure 2 shows a simple schematic of the two-electrode micro-PPT⁷. In this configuration, a capacitor is connected to the coaxial propellant unit. The propellant consists of a central conductive rod functioning as the cathode and an annulus of PTFE encasing the cathode. The anode tube encloses the propellant. The major difference between the standard PPT and the two-electrode micro-PPT lies in the electronics. The micro-PPT uses only one circuit with one DC-DC converter. The capacitor charged by the DC-DC convertor supplies high voltage potential between the anode and cathode. When the thruster discharges, propellant ablates away, ionizes, and accelerates same as a standard PPT. The self-triggered micro-PPT discharge initiates when the electrode voltage exceeds the surface breakdown voltage across the propellant face. Traditional PPTs trigger the discharge using the external igniter plug which supplies a small amount of seed plasma to increase the conductivity across the face of the propellant.

A three-electrode micro-PPT was recently developed by AFRL.⁸ Figure 3 shows the schematic of a three-electrode micro-PPT. The electrodes are referred to as outer, intermediate and center as shown in Figure 3. The center electrode is enclosed by a small annular tube of propellant, which is encased by the intermediate electrode. This intermediate electrode is also enclosed by a larger annular propellant tube, which is then surrounded by the outer electrode tube. The intermediate discharge between the central and intermediate electrode provide seed ionization plasma. This plasma reduces the resistance along the entire face of the propellant. The higher energy for main discharge

between the intermediate and outer electrode follows directly behind this initial plasma formation.

Using the three-electrode design has three major benefits. First, the energy of the main discharge now has minimal shot-to-shot variation decreasing the possibility of carbonization on the propellant face. Second, the seed ionization from the trigger discharge significantly decreases the voltage required on the main discharge to initiate the main pulse. For example, the trigger discharge will use about 1/50 the energy of the main discharge. Three-electrode micro-PPTs need relatively low voltage potentials (below 3000 V) in applications of 6.35 mm (1/4") diameter propellant tubes. Without a three-electrode design, the discharge across a 6.35 mm (1/4") diameter propellant requires up to 40,000 V to initiate the propellant surface ablation. Operating at lower voltages means we can reduce the mass of the electronics and therefore the thruster. A third advantage highlights the robustness of the design. The three-electrode design allows for better controllability. Firing frequency can be increased by decreasing the resistance in the trigger circuit or by increasing the output current of the PPU.

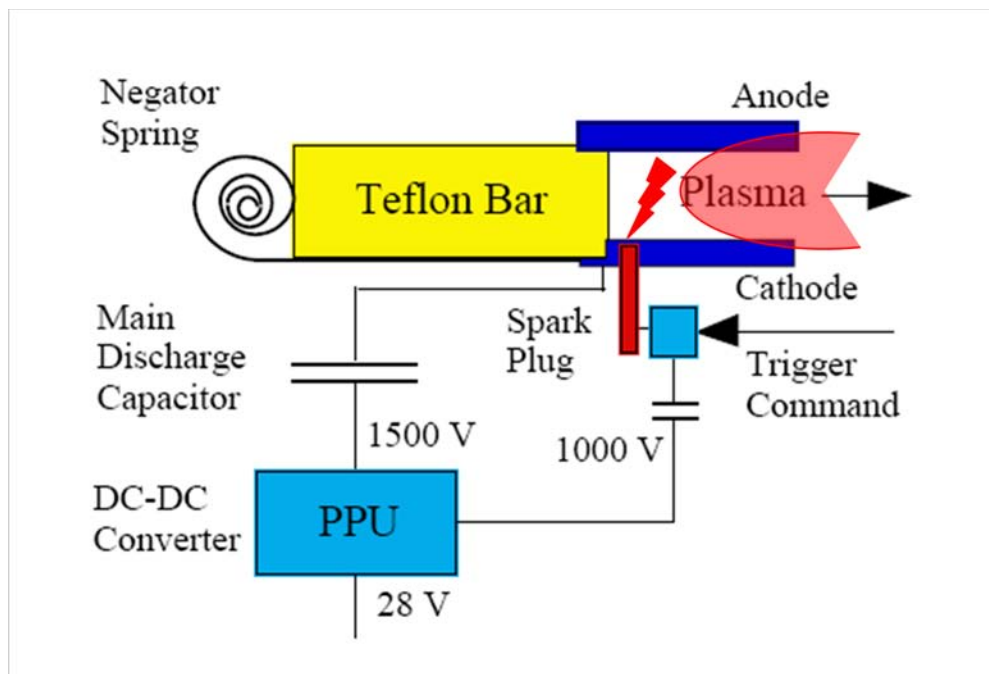


Figure 1: Standard Pulsed Plasma Thruster⁹

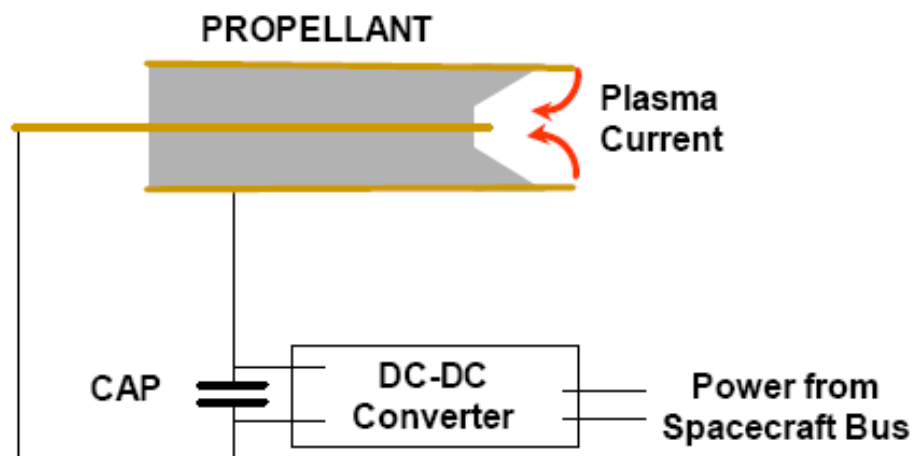


Figure 2: Two-electrode micro-PPT⁷

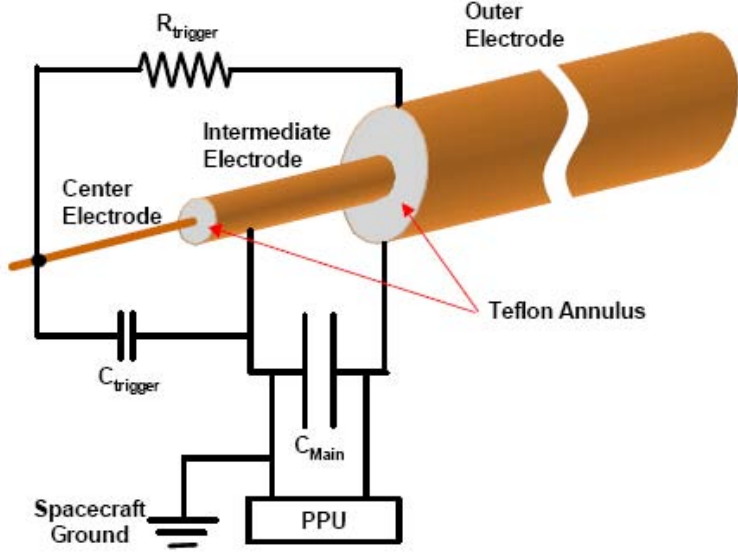


Figure 3: Three-electrode micro-PPT⁷

II.4. Optimization issue and modeling for micro PPT

Micro-PPT operation depends on the energy and propellant tube geometry as mentioned earlier. Discharge uniformity (azimuthal and radial) is considerably affected by the both discharge energy and thruster size. The current constriction and anode spot formation phenomena is related to azimuthal non-uniformity which occurs when the discharge current or thruster tube size surpass some critical value.¹⁰ Discharge non-uniformity results in a much higher ablation rate and decreases the potential specific impulse. In contrast, a small discharge current leads to strong charring and radial non-uniformity, which will eventually lead to thruster failure. The main reason of the charring was initially related to carbon back-flux. Thus, by adjusting the conflicting requirements between large (to prevent charring) and small energy (to prevent current constriction), the thruster geometry and discharge energy can be optimized.

University of Michigan and AFRL have published models for a micro-PPT.¹¹ They developed models including plasma generation, flow and expansion in the near field. They studied the plasma acceleration by the electromagnetic force and magnetic field dispersion into the plume. The propellant surface formed an inverse cone with a peak at the central electrode resulting from maximum temperature and ablation rate at the center of propellant. A comparison between the model and experiment for ablation depth and ablation profile showed similar results.

II.5. Measuring the Particle velocity and angle distribution of the two-electrode micro-PPT

Sakir Tirsı employed a technique taking high-speed images of the exhaust plume from different angles to investigate exhausted particulate velocities.¹² He determined the speed of the particles with these images and characterized the exhaust plume angle with respect to the propellant face. Experiments were conducted at a small vacuum chamber at AFIT. The captured data was evaluated frame by frame. Discernible particles were selected with the purpose to create a velocity profile. Many particles were needed for reliable statistics. Velocities were calculated using two techniques. The first method measured pixel length of the particle streaks in any given image. This pixel length divided by the image exposure time gives a relatively accurate velocity of the particles. The second technique is to capture the same particle in two consecutive frames. This method is useful for the slower particles because of relatively longer times between frames. Figure 4 is an example of three consecutive images of a single discharge. Figure 5 shows an example of how Tirsı used the data to determine velocity and plume angles.

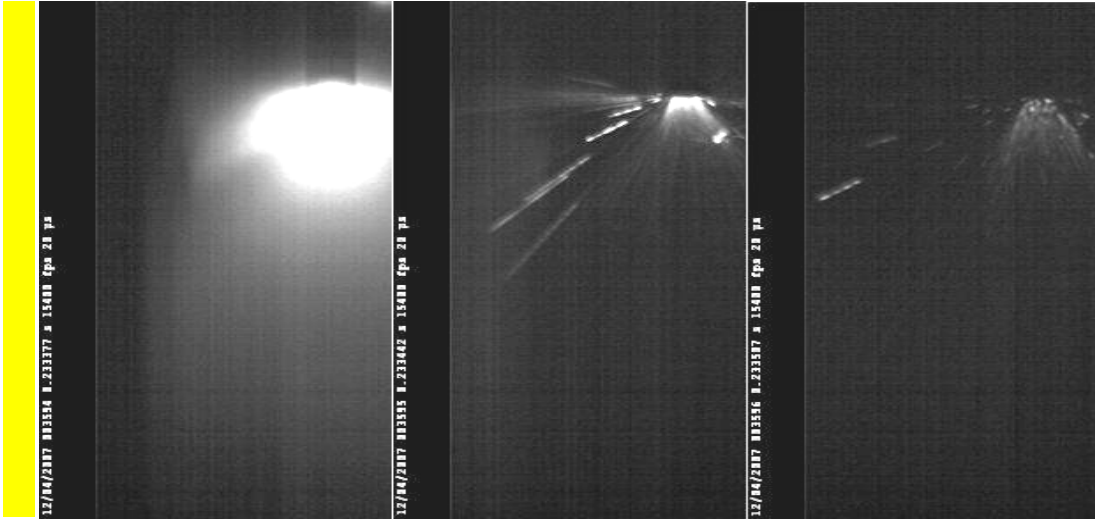


Figure 4: Consecutive Images Taken at 15400 fps and 20 μ s Exposure Time

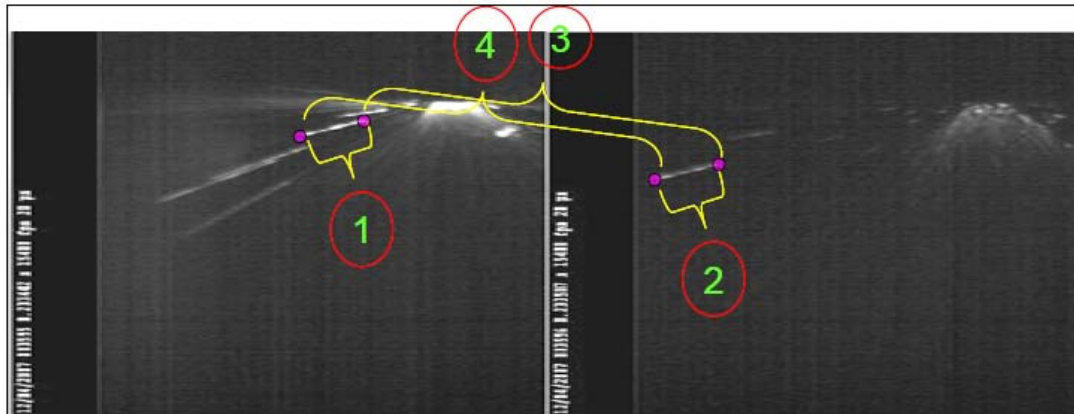


Figure 5: Velocity and Angle Measurements from Images

Figure 6 shows the distribution for the data collected for a 35 μ s exposure time. This distribution follows a Gaussian distribution for all the particles collected (Figure 7). These two figures show different exposure times does not change the distribution relationships, thus this method does not introduce any error into the measurements. For the higher velocity particles, more data is required to get a complete picture. In this work,

the particles faster than 400m/s and 800m/s contributed only 11% and 0.5%, respectively. The data previously collected (Figure 6 and Figure 7) only represents a two dimensional velocity of the particles, a limitation of having images from only one position.

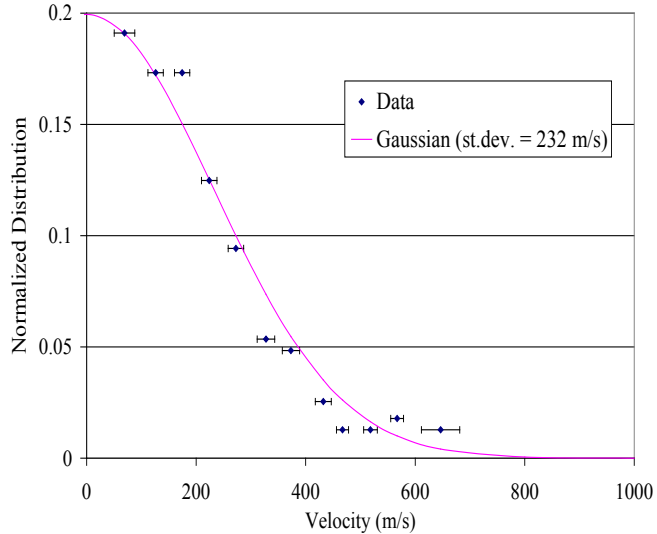


Figure 6: Particle Velocity (Magnitude) Distribution $35\mu\text{s}$

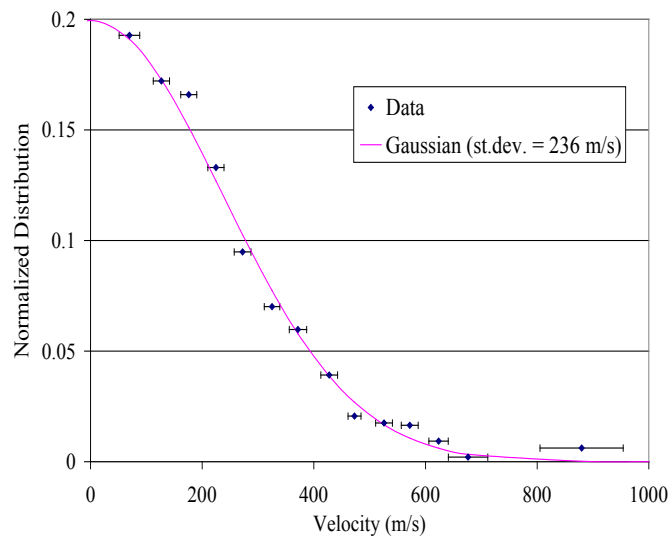


Figure 7: Velocity (Magnitude) Distribution for All Particles

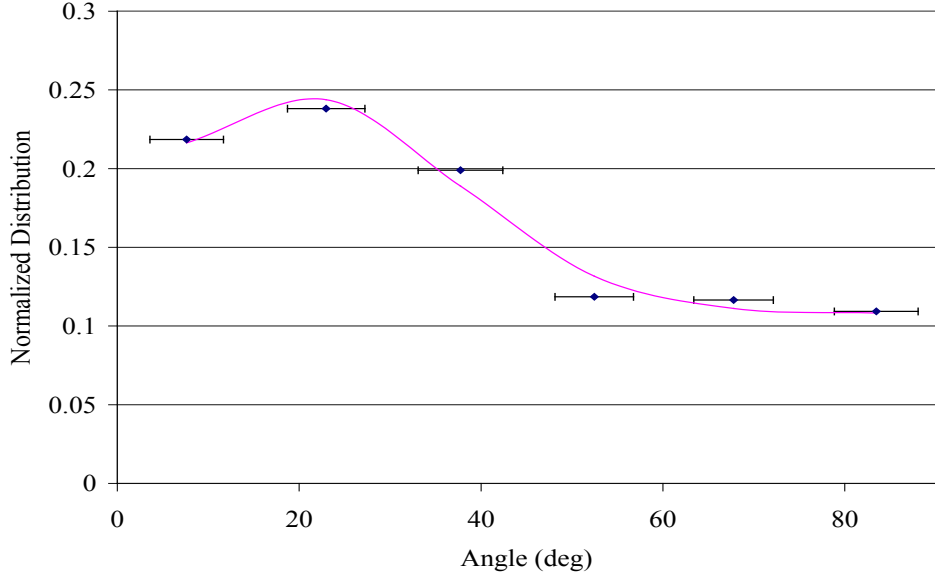


Figure 8: Normal Distribution for Particle Angles

The angle distribution also has been analyzed using the same results (Figure 8). This information shows particle departures were peaking around 30 degrees from the centerline for the self-triggered, two-electrode design. A concern with thrusters of this type is the relationship between the particle velocity and departure angle. Tirsi classified the particles slower than 200 m/s, slower than 300 m/s, faster than 300 m/s and faster than 500 m/s. Figure 9 shows the distribution for slow particles exhibiting the same tendency as seen for the distribution for all angles (Figure 8). This results means the slow particle distribution dominates the distribution for all the particles.

Figure 10 shows faster particles ($>500\text{m/s}$) leave the thruster face with a slightly narrower angle (20 degrees) comparing to the slow particles (25 degrees). In capturing the fast moving particles, Tirsi had to reduce the lapse time of 74 μs between frames to 35 μs . The associated frame rate is 28,500 fps. At higher frame rates, the camera is not able to retain the same resolution, reducing the obtainable capturing area to a resolution

height of only 116 pixels. This restriction hampered the data capturing ability requiring more data captures to provide valuable data. Figure 11 is an example of images taken at these settings (28,500 fps and 16 μ s exposure time). The first image is saturated by the spark. The second and third images show the same particle as it moved away from the thruster, moving at 258 m/s. The fastest particle is in the second image with a velocity of 788 m/s.

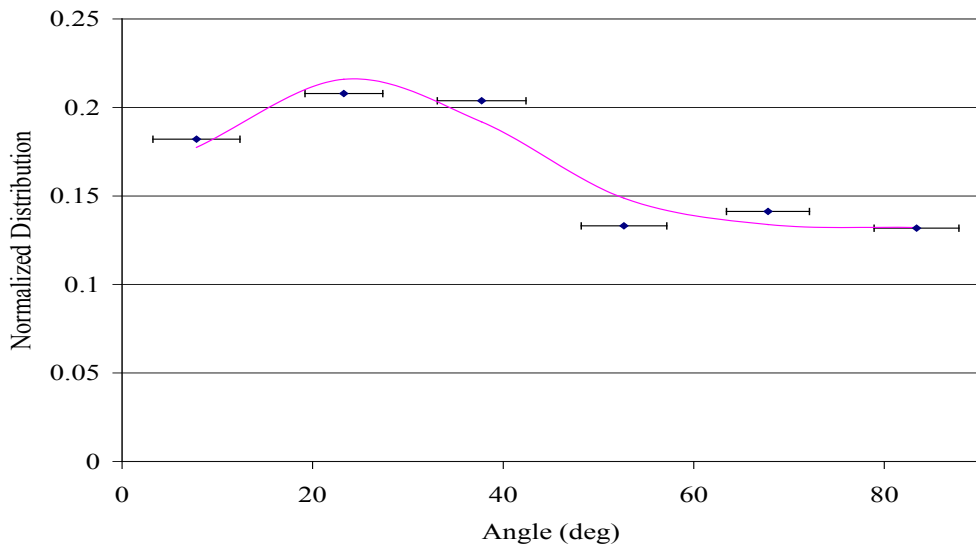


Figure 9: Angular Distribution for Slow Particles, < 300 m/s.

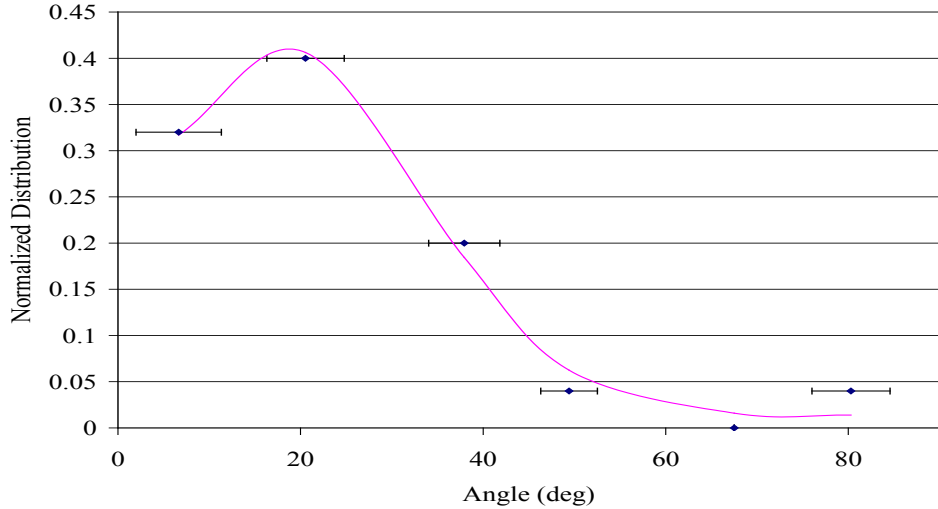


Figure 10: Angular Distribution for Fast Particles, > 500 m/s.



Figure 11: Particle Travel Progress at 28500 fps and 16 μ sec of Exposure Time

II.6. Contamination issue for two-electrode micro-PPT

Ceylan Kesenek employed a two-electrode micro- PPT for characterizing the exhaust plume in the vacuum chamber at AFIT (Air Force Institute of Technology).¹³ The experimental setup used witness plates (Figure 12) placed directly in the exhaust plume in order to capture the mass deposition over a wide angle. The mass deposition on

the witness plates is analyzed using a scanning electron microscope (SEM). The two-electrode micro-PPTs used in this research were developed at the AFRL Electric Propulsion Laboratory at Edwards AFB, CA with modifications to the control circuit developed at AFIT. The DC-DC converter operated over the input voltage range from 1 to 15 V and provided up to 7000 V to the thruster. A thruster stand was used to keep the thruster and witness plates in position. The aluminum witness plates were placed at several different angles at the same radius from the thruster to characterize the plume contamination, ensure radial symmetry and as a check on the experimental setup.

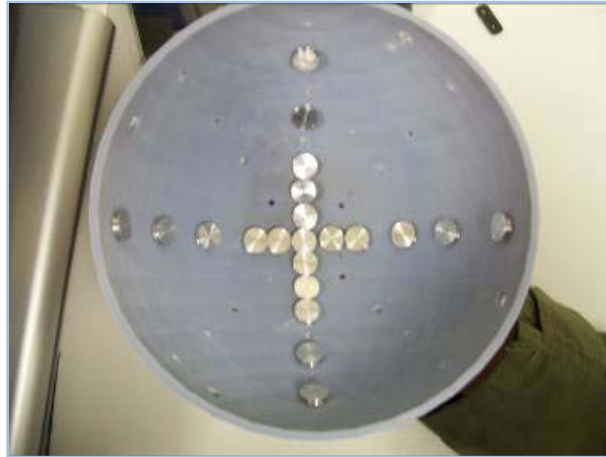


Figure 12: Bowl-shaped Witness Plate Holder

The Scanning Electron Microscope (SEM) was used to examine the witness plates with up to 133x magnification levels allowing particles with a diameter as small as $5 \mu\text{m}$ to be distinguished with sufficient detail. The particles were classified by their diameters providing a means to determine mass deposition as a function of angle. Cesenek's research provided four primary results. First, the operation of the micro-PPTs system was reliable and consistent for up to three hours without any problems. The pulse and pulse

frequency were well controlled. Table 2 provides two- electrode micro PPT operating conditions used in here.

Table 2: micro-PPT operating condition

Test No	Capacitor Capacitance	Input Voltage (Volts)	Vacuum Pressure (torr)	Duration (Hours)	Frequency (Hz)
1	1 μF	3000	10^{-6} - 10^{-7}	1	1
2	1 μF	4000	10^{-6} - 10^{-7}	1	0.5
3	1 μF	5000	10^{-6} - 10^{-7}	3	0.4

Second, particle diameters ranged from 5 - 60 μm . Some smaller particles were observed at higher SEM magnification but did not considerably contribute to the total mass being deposited. The major contribution of mass deposition is from the 30-50 μm diameter size. Results showed the number of particle with smaller diameters were much more abundant than larger ones. The graph shows more particles exist with diameters less than 30 μm than particles with diameters greater than 30 μm (Figure 13).

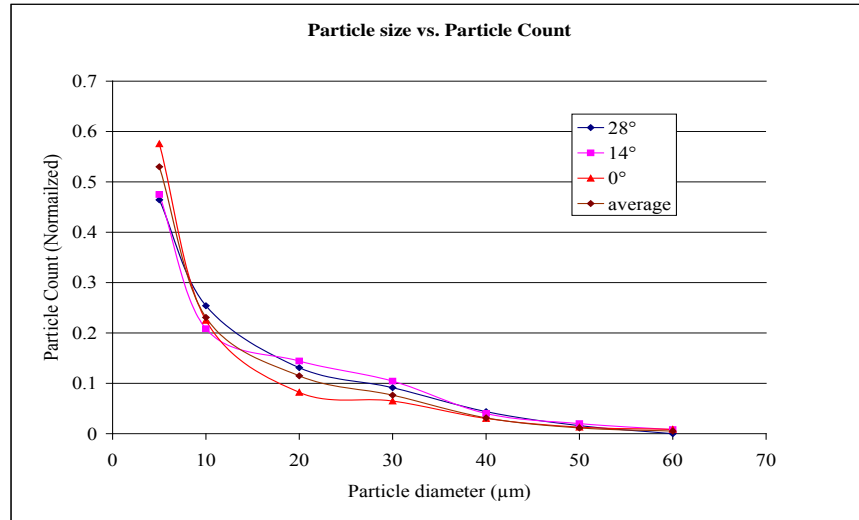


Figure 13: Particle size vs. Normalized Particle Count

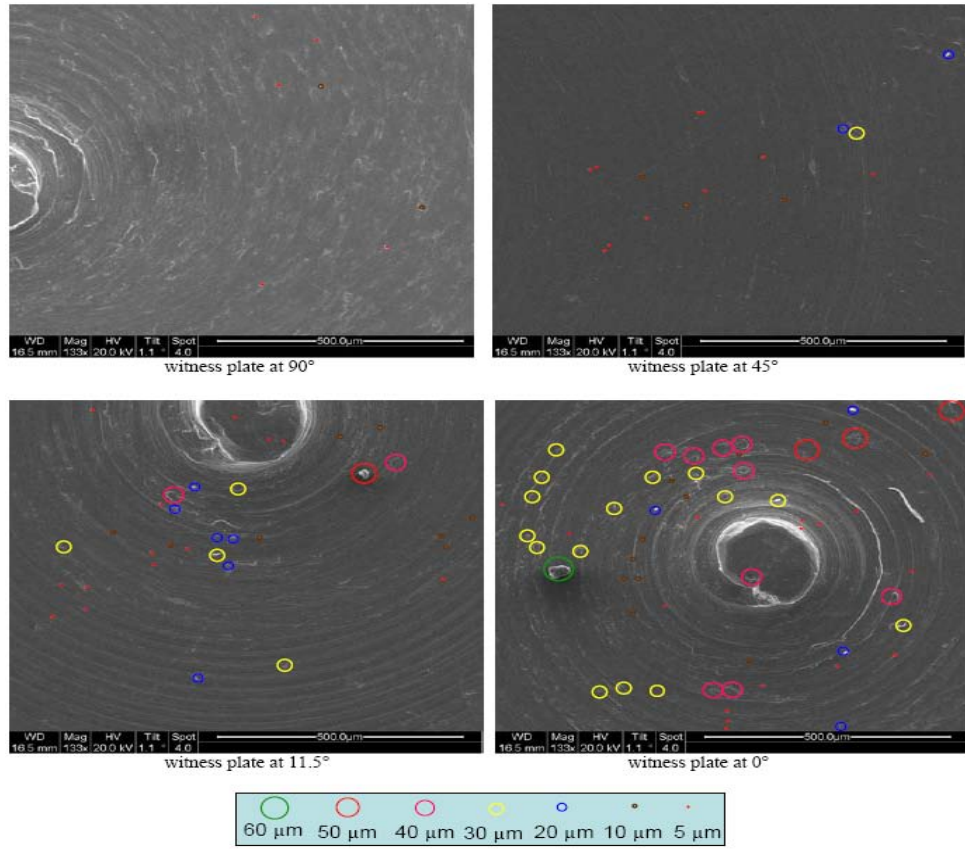


Figure 14: Mass Contribution of Each Particle Size for Various Angular Positions.

The particle size close to the center line tended to be larger (Figure 14). Third, mass deposition profile was created with an average uncertainty of 14%. The mass deposition of the exhaust plume was very high near the axis of the thruster. The majority of mass (93.6 %) was deposited between 0° and 30°. This distribution of the mass can be represented with two distinctly different Gaussian distributions. (Figure 15)

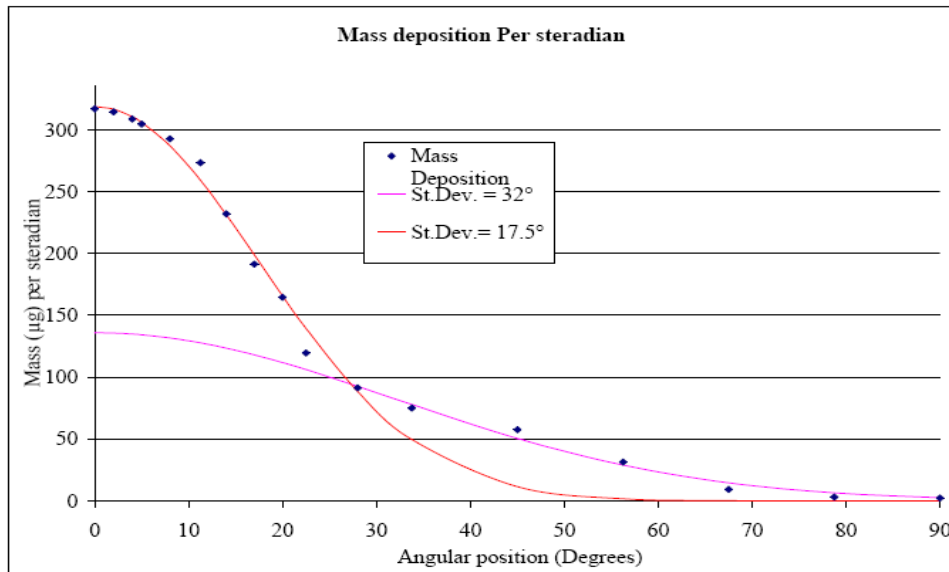


Figure 15: Mass Deposition Profile

Figure 16 shows the mass deposition rates per steradian per pulse versus angular position. When comparing the micro-PPT results here with larger standard PPTs, Kesenek found the mass deposition profile agreed with previous research studies by G. Spanjers, et al, at U.S. AFRL on a much higher powered PPT, 20 J at 1 Hz operation.

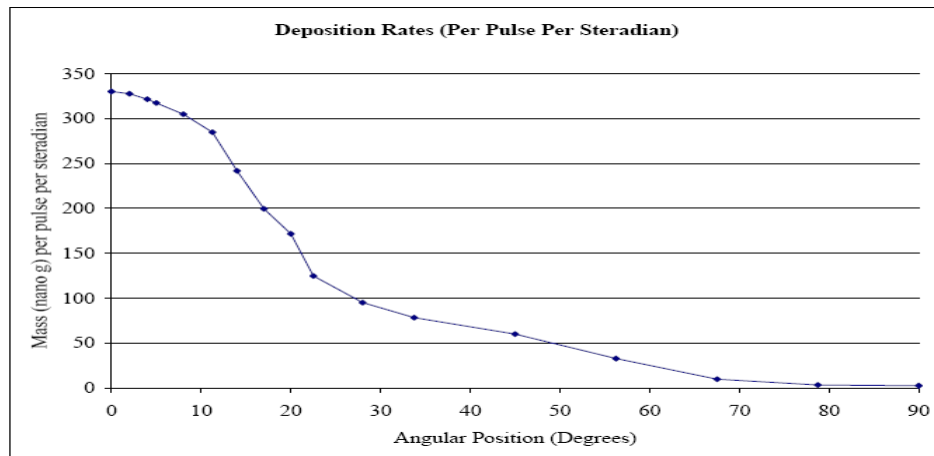


Figure 16: Deposition Rates per Pulse per Steradian

Last, the micro-PPTs were weighted before and after the experiments using a milligram scale with a resolution of 1 mg. The propellant deposited on the surface only accounts for about $4.9 \pm 0.25\%$ of the total mass being ejected from the thrusters. With this information, we can determine the propellant utilization efficiency if we can get information about thrust and particle velocities of the propellant.

III. Methodology

III.1. Chapter Overview

Experimental apparatus and test setup procedure will be introduced in this chapter. Equipment used in this study includes a vacuum chamber, high-speed cameras, a high voltage pulse generator, a function generator and several electronic components to build the micro-PPT circuit for the three-electrode micro-PPT. This chapter describes the micro PPT circuit, how the particles are captured, and data analysis technique used to evaluate them.

III.2. Vacuum Chamber

This research was performed in the Geo orbital Nano thruster Analysis and Testing (GNAT) Lab at the Air Force Institute of Technology (AFIT). They have a vacuum chamber manufactured by Laco Technologies capable of pressure as low as 10^{-8} torr. The vacuum chamber can be operated automatically through a LabView 7.0 program. The vacuum chamber is started by double clicking the LabView icon on the computer monitor after turning on power to the vacuum chamber and computer.

Figure 17 shows the LabView screen after the chamber is activated. There are four main menus; runtime, manual control, configuration and shutdown. The run time menu shows the current vacuum chamber state and is used for starting the vacuum chamber. Manual control provides operation of the vacuum chamber manually. The configuration menu can be used to set the various operating values such as crossover pressure, set point pressure and time scale. These two menus do not need to be employed if the vacuum

chamber is working properly. The shutdown menu is then for stopping the vacuum chamber safely.

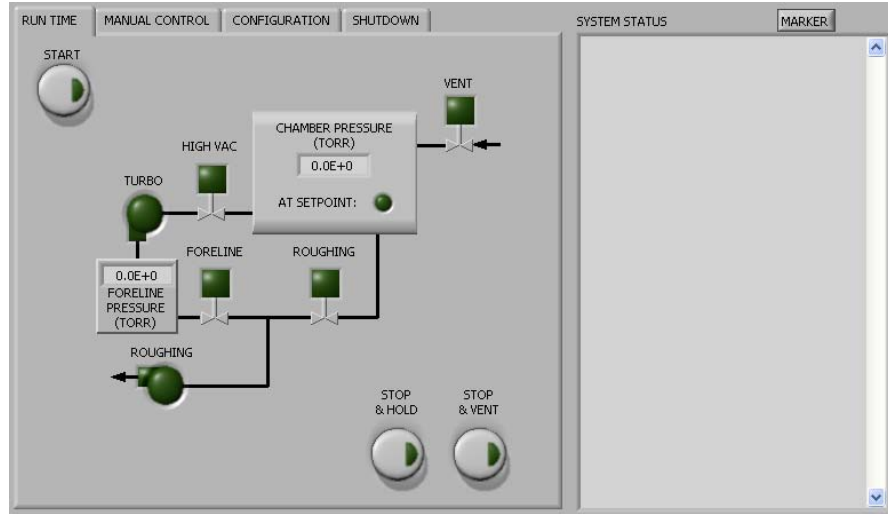


Figure 17: LabView Operation Panel

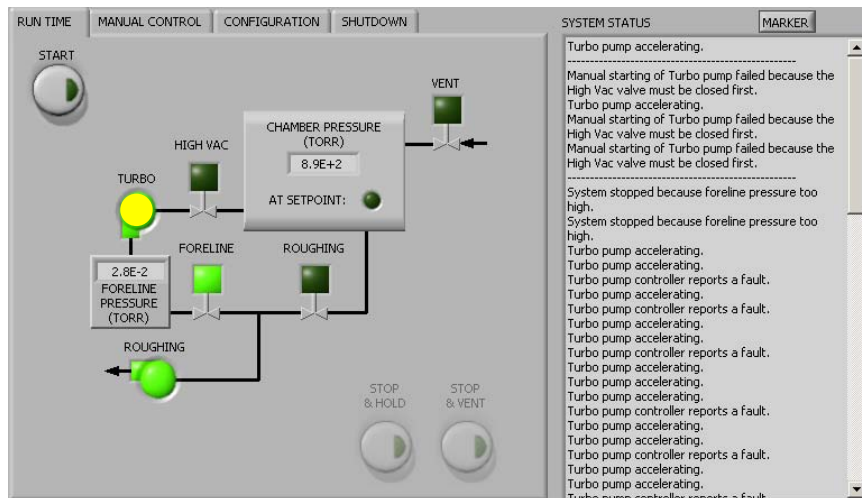


Figure 18: LabView Operation Panel After Activation

Figure 18 shows the LabView screen at startup. The fore line valve opens and the roughing pump starts the initial evacuation of the turbo pump as indicated by the green

lights. The turbo pump light blinks yellow and green while accelerating to operating speeds. A green light indicates when the turbo pump is ready (Figure 19); the fore line pressure drops to the appropriate level.

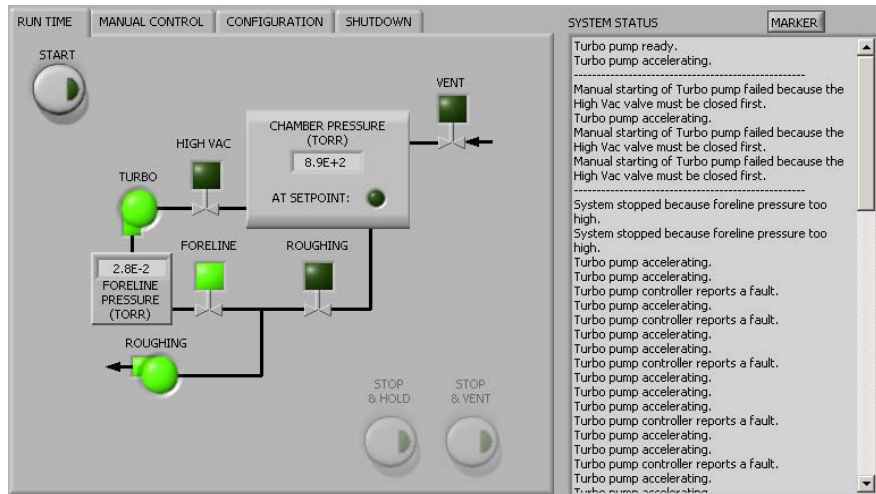


Figure 19: Turbo Pump Ready

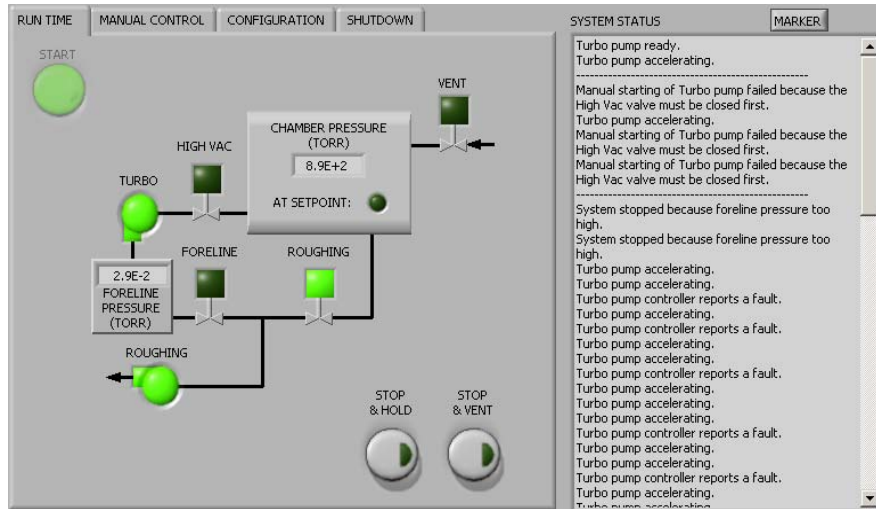


Figure 20: Vacuum Chamber Initial Pump Down Configuration

The fore line valve then closes and the roughing valve opens automatically (Figure 20). The chamber pressure drops off gradually from atmospheric pressures until it reaches the crossover pressure set point, 10^{-3} torr. The chamber pressure drops off rapidly

after reaching the crossover pressure and the turbo molecular pump is engaged. At the crossover, the high vac and fore line valves are opened and the roughing valve closes. (Figure 21)

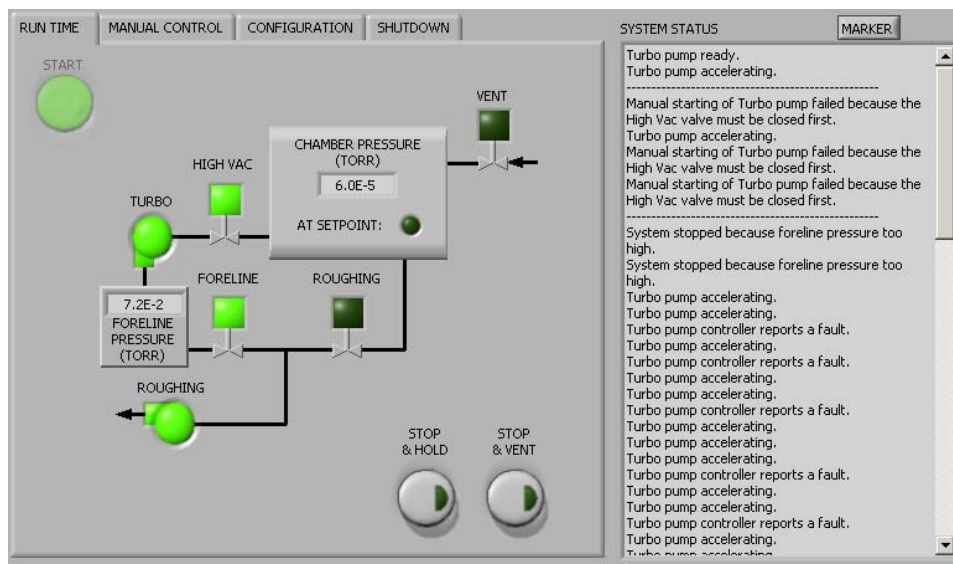


Figure 21: Crossover Pressure Set Point Operation

The research goals and proper thruster operation require simulating a near space environment. The desired chamber pressure to meet this need is 10^{-5} torr. A blue light indicates the chamber pressure has reached the desired research environment (Figure 22). The pressure continues down until the “stop & hold” or “stop & vent” button is hit. The “stop & hold” button is for stopping the pump and holding the current pressure but the pressure does start to go up due to leak paths through the pumps. The “stop & vent” button is for stopping the pump and venting the chamber back to ambient pressure. Both the high vacuum and roughing valves are closed and fore line valve is open when hitting the “stop & hold” button. The same occurs for the “stop & vent” with the addition of the vent valve opening.

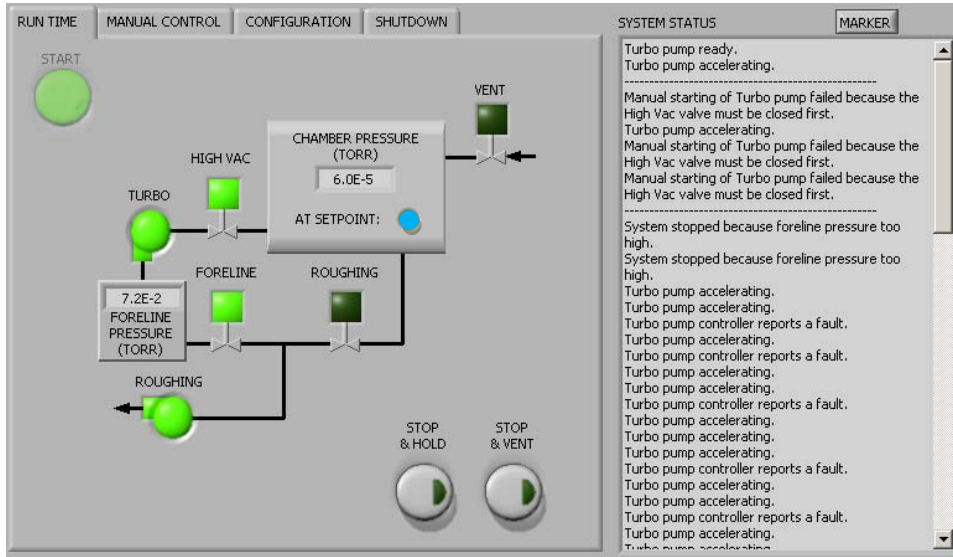


Figure 22: Reaching a Set Point

Figure 23 and Figure 24 show the front and side view of the vacuum chamber used in this research.

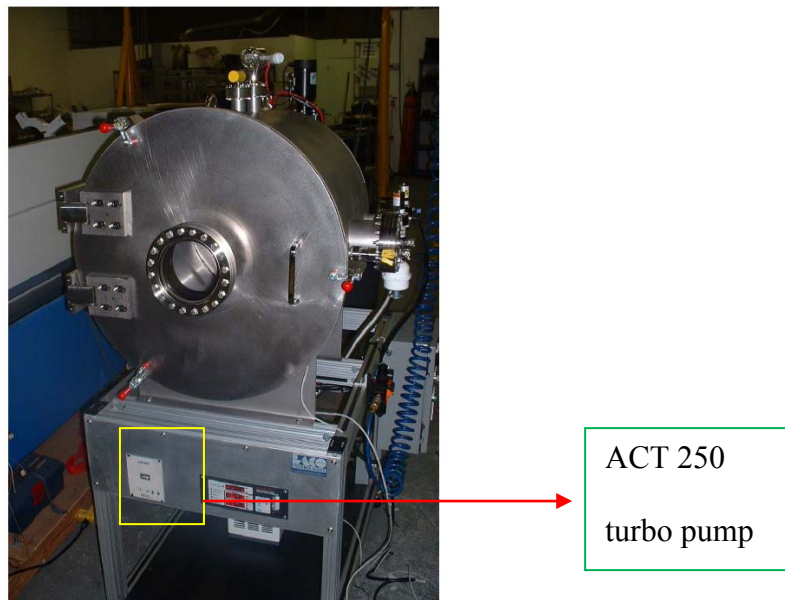


Figure 23 : GNAT Vacuum Chamber #2 Front View

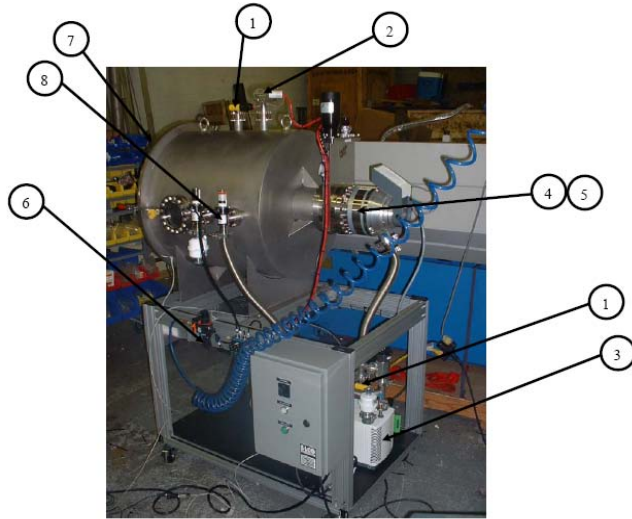


Figure 24: GNAT Vacuum Chamber #2 Back and Side View

Number 3 in Figure 24 is the roughing pump (pumping speed of $27 \text{ m}^3/\text{h}$)¹⁴. This pump can achieve an ultimate pressure without purge of $3 \times 10^{-2} \text{ mbar}$ ($2.25 \times 10^{-2} \text{ torr}$). The turbo pump, (4 and 5 in the figure) provides pumping speeds up to 400 l/s and an ultimate low pressure of $5 \times 10^{-10} \text{ mbar}$ ($3.75 \times 10^{-10} \text{ torr}$)¹⁴. The ion gauge (2 in Figure 24) measures low pressure using ionization current which decreases with the decrease in the pressure. Figure 25 shows the relationship between pressure and the collector current for the ion gage. This gauge has a linear relationship below 10^{-3} torr . The ion gauge takes responsibility for accurate pressure readings when the chamber pressure drops below 10^{-3} torr .

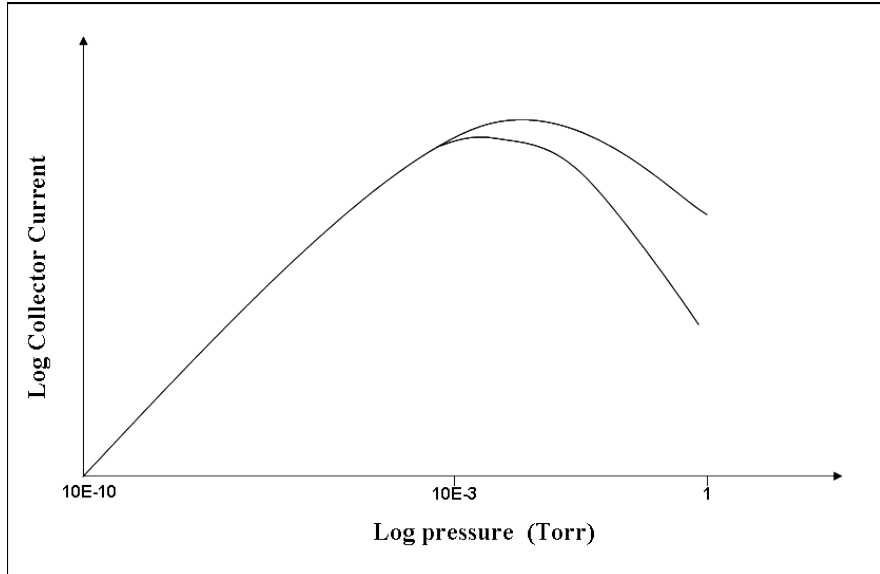


Figure 25: Relationship of Collector Current and Pressure

III.3. Experimental Setup

The high speed particles are captured with two high-speed cameras from two different perspectives to quantify the velocity and angle in 3D space. In order to determine these performance parameters accurately, assembling the necessary components is critical: vacuum chamber, high-speed cameras, high voltage pulse generator, function generator and some electronic components such as a high voltage converter, capacitors and the three-electrode micro-PPT tube. This section explains how each component was connected for this test setup. A quick review of each key apparatus will be described as well. Figure 26 shows a schematic of the experiment setup. The HV pulse is for seed ionization, so it connects with the intermediate electrode and center electrode. The power supply and high voltage converter connect with the outer electrode and center electrode for the main discharge. We used two 1.0 μ F capacitors to provide enough energy for the main discharge. The three-electrode micro-PPT tube is placed into

the holder in the vacuum chamber. To determine three dimensional performance, two cameras are placed at specific angles to one another. One is in front of the chamber, the other is placed at 90 degree to the front aimed at the thruster through a side window. The function generator will trigger the HV pulse and the two cameras when triggered giving the images from both cameras capturing the pulse event.

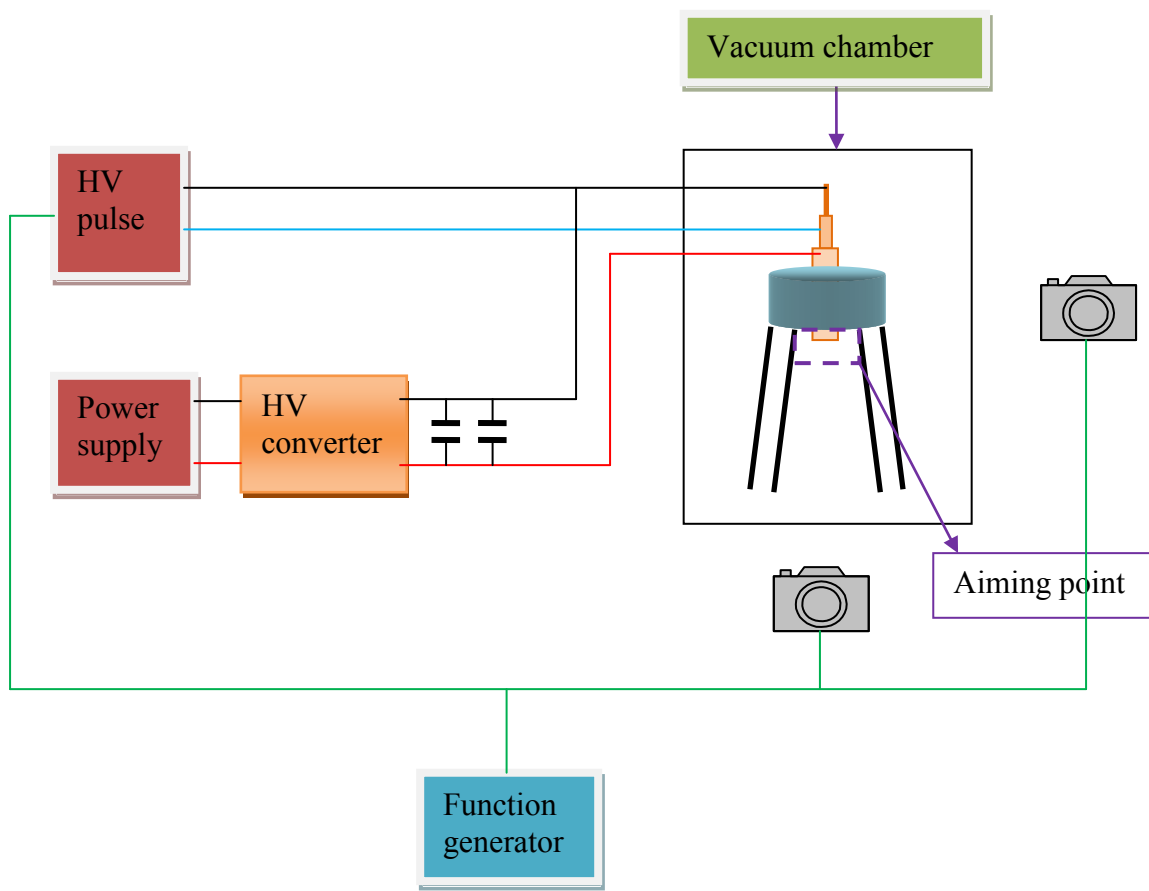


Figure 26: Test setup

The biggest issue in this test setup is synchronization of the equipment. When all equipment is working well and connected properly, the test produced very accurate results. Individually, the equipment such as vacuum chamber, camera and thruster worked well but often proved a bit more temperamental when installed together. One

significant issue was the thruster operation after installed in the vacuum conditions. The high vacuum removed the air normally providing the thruster just enough conductivity across the face to actuate in the lab. Besides the difficulty with getting it to fire, the high voltage lines would often find a short path to ground out to the chamber. Additional care and equipment was needed to ensure high-voltage feed through were properly insulated.

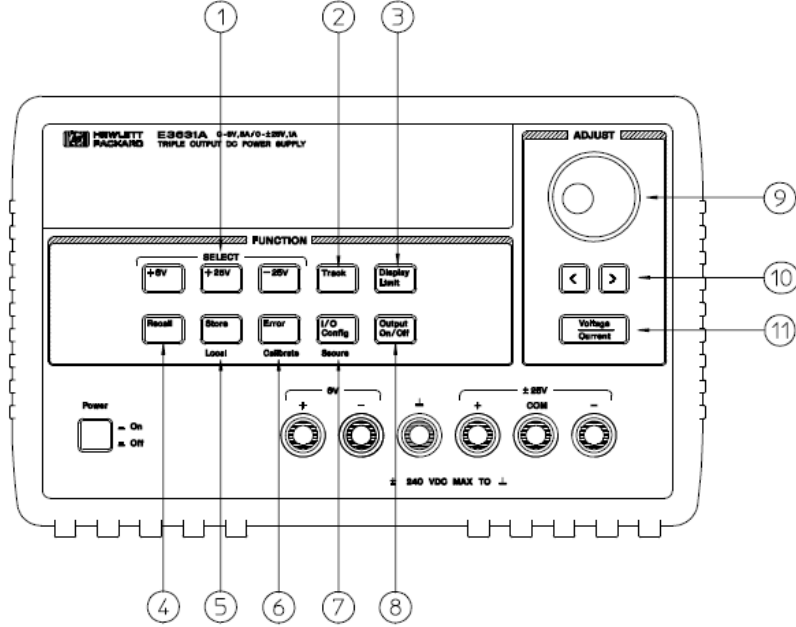
The cameras proved to be sensitive to operation as well. One camera showed an error message when too close to the vacuum chamber, possibly being affected by the high voltage pulse generator. The high voltage affected this specific camera but the second camera (same make and model) did not have this problem. However, the first camera worked well when it was moved farther from the vacuum chamber.

In determining sound operation of the equipment together, settings for the function generator for triggering the intermediate discharge and cameras needed to be varied over a wide range. Finding the right voltage settings to trigger the equipment did not take a lot of time but was essential in providing a smooth operation.

III.3.1. Power Supply

The Agilent E3631A power supply (Figure 27) features a combination of programming capabilities and a linear power supply performance making it ideal for the three-electrode micro-PPT application. The triple power supply delivers 0 to ± 25 V outputs rated at 0 to 1 A and 0 to +6 V output rated at 0 to 5 A. The ± 25 V power also provides a tracking output to power operational amplifiers and circuits requiring symmetrically balanced voltages.¹⁵ To supply the DC power to the circuit, the power supply is set to 25 V (#1 and #8 in Figure 27) and then the voltage level is adjusted using

the resolution selection key (#10) and control knob (#11). This research explored voltage input settings from 1 V to 8 V in 1 V increments.



1 Meter and adjust selection keys	6 Error/Calibrate key
2 Tracking enable/disable key	7 I/O Configuration / Secure key
3 Display limit key	8 Output On/Off key
4 Recall operating state key	9 Control knob
5 Store operating state/Local key	10 Resolution selection keys
	11 Voltage/current adjust selection key

Figure 27: Agilent E3631A Triple Output DC Power Supply

III.3.2. High Voltage Converter

The three-electrode PPT uses a high voltage discharge to ablate the propellant. The EMCO F series (Figure 29) provides 100 VDC to 12,000 VDC (positive or negative polarity) at 10 Watts continuous output power at an adjustable rate based on input voltage¹⁶. Table 3 and Figure 28 show the relationship between power supply and high

voltage converter. The output capability of the pulse generator was measured in the lab to confirm performance and ensure it was capable of providing enough energy to ignite the PPT. This hardware was used from many tests but often did not provide enough energy to the PPT discharge. An alternative circuit was also employed to allow for higher energy discharges.

Table 3 : Relationship between power supply and high voltage converter

Input Voltage	1	2	3	4	5	6	7	8
Output Voltage	290	760	1100	1400	1640	1840	1990	2110

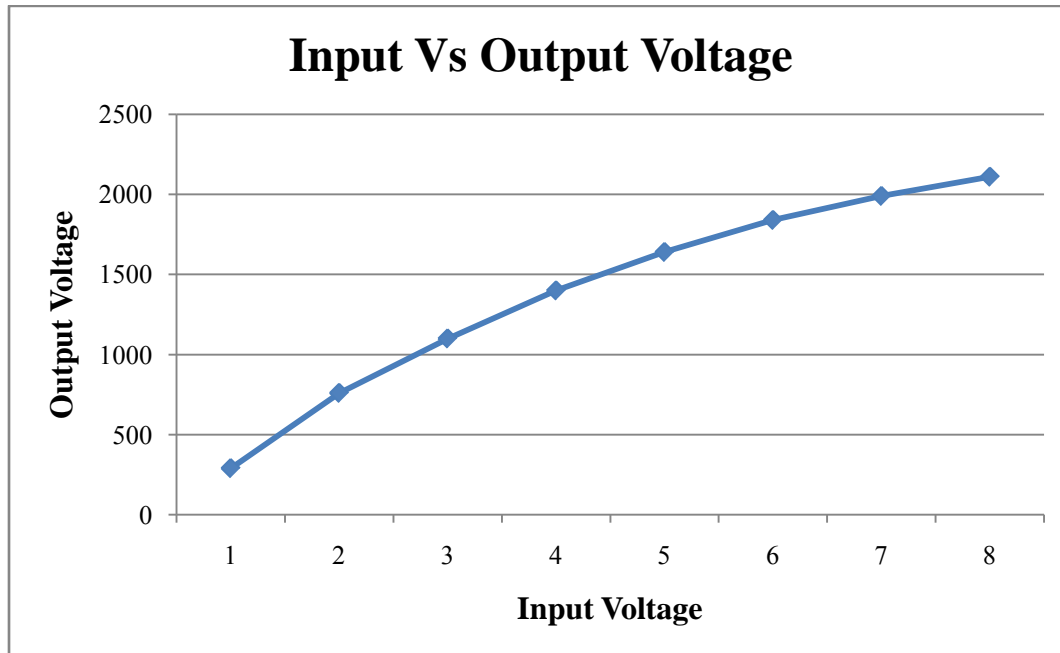


Figure 28: Relationship Between Power Supply and High voltage converter



Figure 29 : Emco Amplifier F series

III.3.3. High Voltage Pulse

To trigger the three-electrode PPT design, a high voltage pulse generator provided enough energy resulting in seed ionization plasma between the inner most two electrodes¹⁷(Figure 30). Table 4 shows some of the specifications for the high voltage pulse. The voltage output, pulse repetition rate and pulse width can all be adjusted to operate at optimal conditions for the test.

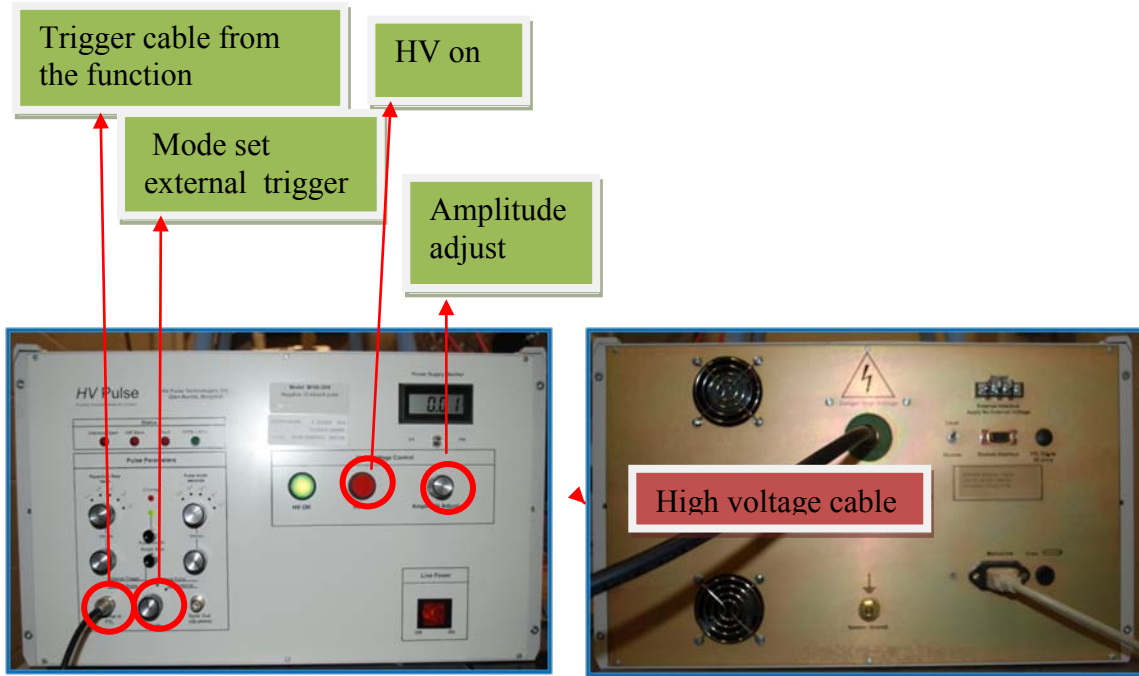


Figure 30: High Voltage Pulse, M10k-20 (Front and Rear View)

Table 4: High Voltage Pulse Generator Specifications

Parameter	External Load	
	None	10,000 Ω / 40 pF
Amplitude (kV)	0.5 to 10	0.5 to 10
Rise Time (ns)	< 150	< 500
Fall Time (μ s)	< 5	< 2
Width (50 %) (μ s)	3 to 1,000	1 to 100
Max Repetition Rate (Hertz)	> 6,000	> 600
Maximum Duty (%)	> 2	> 0.2

III.3.4. Wave Form Generator, Synchronization

To ensure accurate data capture, the cameras had to be synchronized with each other as well as with the pulse event. The Agilent 33120A is high performance function generator with built in arbitrary waveform capability, suitable for convenient use on a

laboratory workbench and ideal for this test configuration.¹⁸ This function generator can produce square, sine, triangle and ramp wave forms. The ramp wave proved to be an effective trigger for the high speed cameras (XS-4) and the voltage pulse generator (M10k-20) in this research.

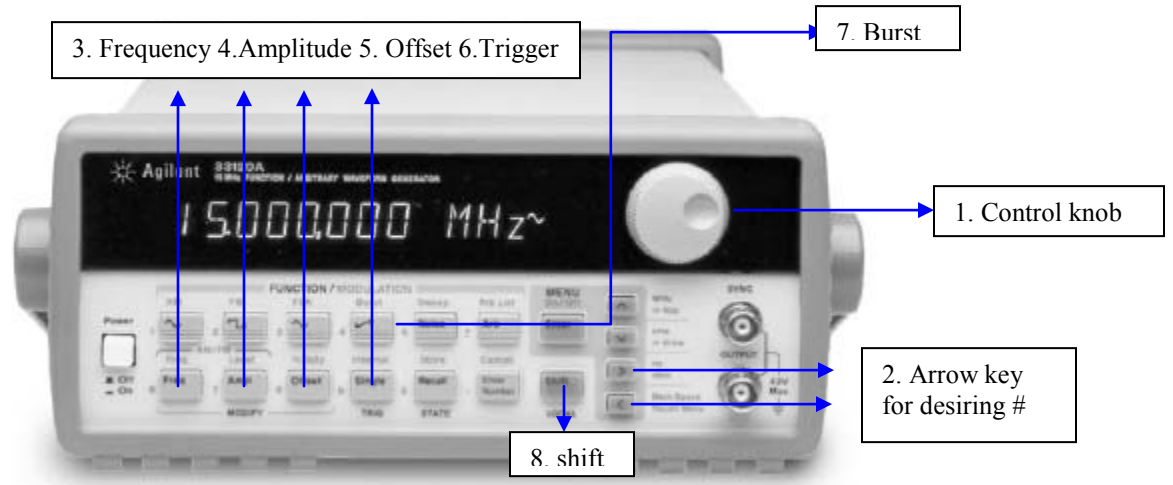


Figure 31: The Agilent 33120A Function Generator

The maximum frequency of the Function Generator depends on the wave form (Table 5). Output amplitude of the voltage ranges from 100 mV to 20 V. This research sets the frequency at 1 Hz with 5 V amplitudes. The single trigger is then independent of frequency. A voltage of only 2.5 V is enough for both the high-speed camera and HV pulse to trigger.

Table 5 : Output frequency

Wave form	Minimum frequency	Maximum frequency
Sine	100 μ Hz	15 MHz
Square	100 μ Hz	15 MHz
Triangle	100 μ Hz	100 kHz
Ramp	100 μ Hz	100 kHz

III.3.5. High Speed Cameras

The Motion Pro XS-4 camera features a USB 2.0 (480 Mbps) digital interface and Giga Ethernet (1000 Mbps) providing high-speed rate of transfer to a desktop or laptop computer with a single cable. The camera captures the motion of objects at ultra-high speeds.¹⁹ It has 4 GB internal memory and provides maximum resolution of 512 H x 512 V. At the full resolution (512x512 pixels), the camera can capture images as fast as 5,145 frame per second (fps). The frame rate is important in this research because particle speeds are on the order of 500 to 1000 m/s. The frame rate can be increased by reducing the image resolution. Table 6 shows the relationship between image resolution and maximum frame rate. The camera trades increased frame rate with vertical pixel size providing a means to capture axially traveling particles at good resolution in the primary axis of travel while increasing the frame rate capture. The first row figures in Figure 32 shows the vertical pixel reduced from 512 to 128 keeping the horizontal pixel value the same increasing frame rates by about 4 times more. Properly orienting the camera can improve data capture in the region of interest (ROI). If the camera is aligned vertically with the thruster, reducing the vertical pixels to capture high-speed particles results in not capturing useful information. The vertical image region is too narrow. Most of particles

exit the ROI as shown in the third figure in the first row of Figure 32. This is why the cameras were aligned horizontally. The second row of figures in Figure 32 shows the ROI capturing high-speed particles more effectively. The specification of XS-4 camera is shown in Table 7.

Table 6: Relationship Between Image Resolution and Max Frame rate²⁰

Image Resolution (pixels)	Max Frame Rate (Hz)
512H x 512V	5,145
512H x 256V	10,241
512H x 128V	20,288
512H x 64V	39,822
512H x 32V	76,790
512H x 16V	143,307
512H x 8V	252,794
512H x 4V	409,053

Camera Set	Camera appearance	Image appearance at full resolution 512 H x 512 V (5145 fps)	Image appearance at 512 H x 128 V (20,288 fps)
Original set			

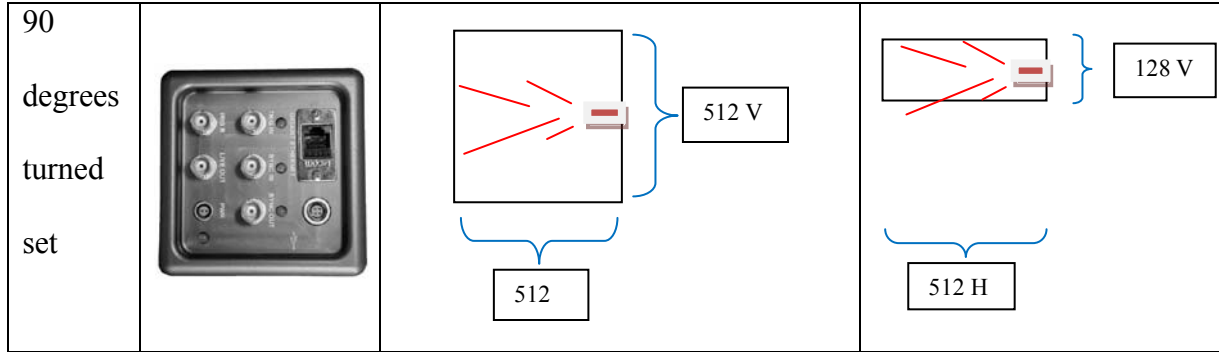


Figure 32: Comparison Between Original and 90 Degrees Turned Camera Set

Table 7 : XS-4 Camera Specification²⁰

Pixel Depth	10 bits
Resolution	512 H x 512 V pixels
Pixel Size	16 μ x 16 μ
Center to Center Spacing	16 μ
Pixel Fill Factor	40 %
Dynamic Range	59 dB
Trigger Mode	Integral (continuous), external (edge-low, edge-high, pulse low and pulse high)
Minimum Inter-frame Rate	100 ns
Trigger and Synchronization	CMOS level (3.3 V) via BNC connection
Digital interface	USB (480 Mbps), Giga Ethernet (1000 Mbps)

The cameras were triggered and therefore connected differently than in previous research. Using sync in and sync out on one camera setting it as master and the other camera as slave proved problematic and did not trigger properly. In this configuration, only the master camera was able to take the image. Therefore, each camera was connected directly to the function generator and triggered simultaneously. The power

lines and USB cables are connected to each camera as well to complete the data transfer from the cameras to the computer (Figure 33). Camera operating procedures for this research are explained in detail in Appendix A.

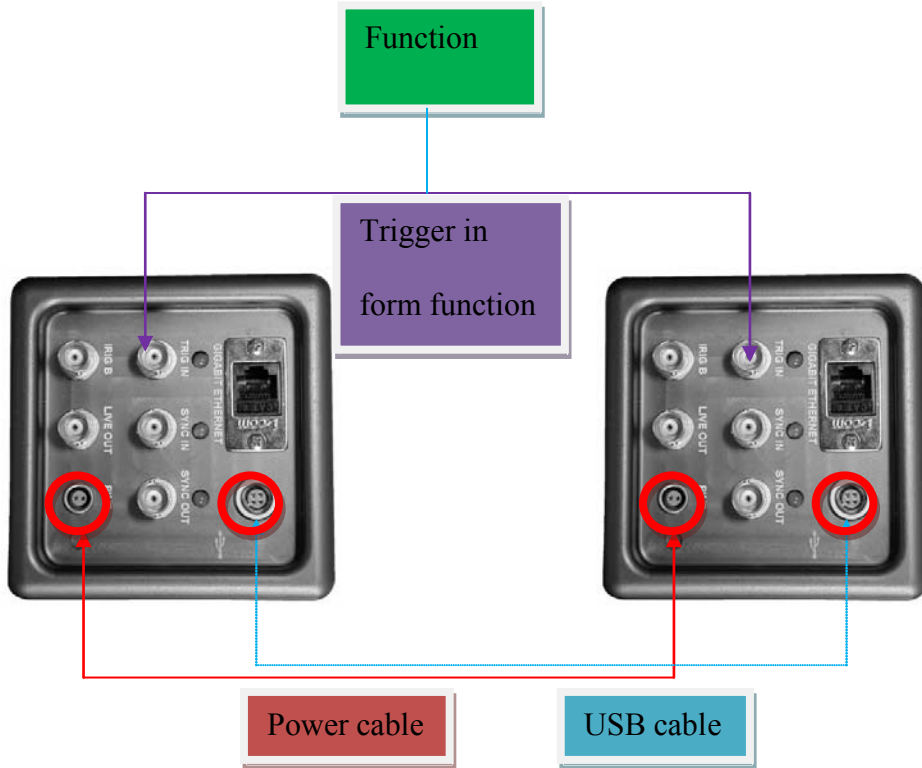


Figure 33: Cable Connection to High-Speed Camera

The lens used in this test was an AF Micro-NIKKOR 60mm f/2.8D which has a 60 mm focal length and the aperture scale is f/2.8 (maximum) to f/32 (minimum)(Figure 34).



Figure 34: AF Micro-NIKKOR 60mm f/2.8D Lens

III.3.6. Three-Electrode micro-PPT Tube

The micro PPT tube used in this research is a 3.175 mm (1/8”), three-electrode design. Figure 35 shows the three-electrode micro-PPT tube geometry. The three-electrode design has two inner electrodes with a much smaller spacing than the main outer electrode. We have already described the two and three-electrode micro-PPT designs in chapter 2 with Figure 2 and Figure 3. Three-electrode micro-PPT has three main benefits when comparing to two-electrode designs. The three-electrode micro-PPT has minimal shot to shot variation decreasing the possibility of carbonization on the propellant face and requires less voltage potential to initiate the main discharge, relying on seed ionization from the intermediate discharge. It can also control the firing frequency easily by simply increasing or decreasing the operation frequency of the input power. However it has more complex circuitry than the two-electrode designs as shown in Figure 3.

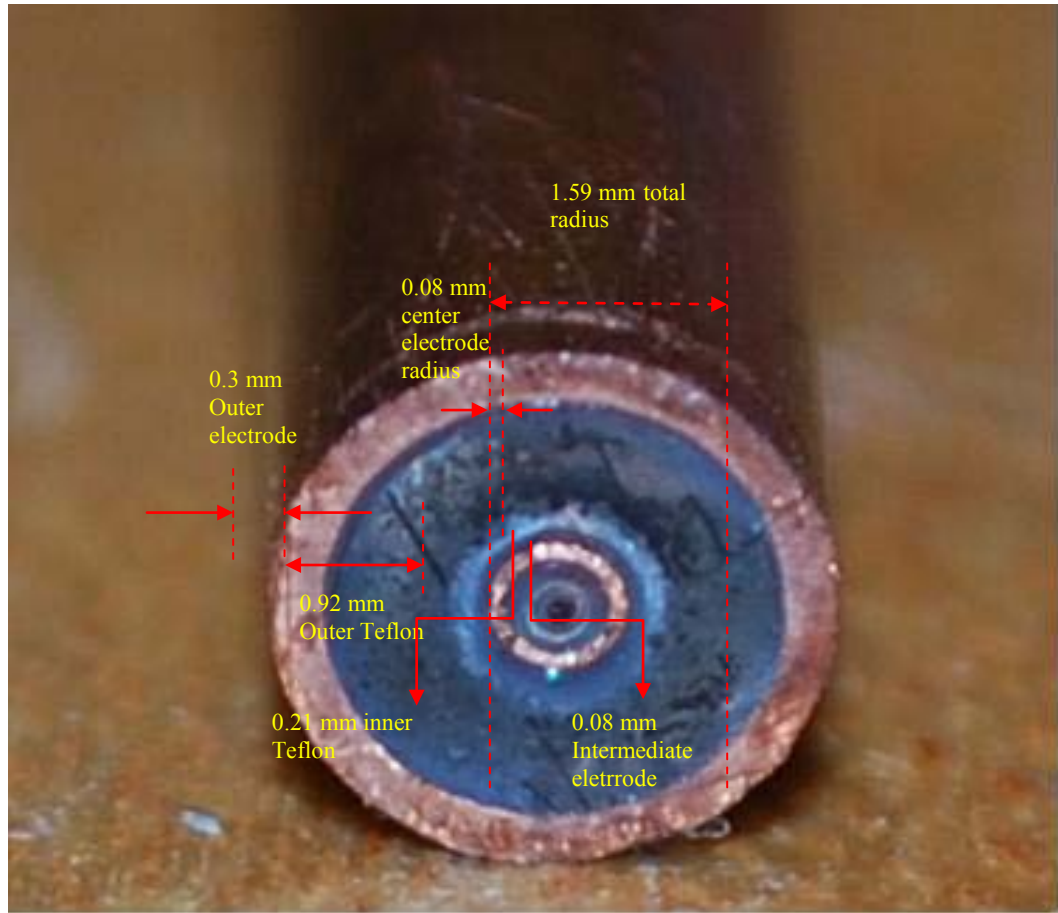


Figure 35 : 3.175 mm (Diameter) Three-electrode micro-PPT Tube

Operating conditions for this geometry can be determined directly. Assuming 10^4 amps current and the PPT can theoretically produce 10,000 m/s exhaust velocity in the ionized gas (as found from previous research), capacitance falls in the range of 0.32 to 1.6 μF using the equation $C = Q_0 / V_0 > 0.0016 / V_0$ for a voltages in the range of 1,000 to 5,000 V. The time scale for a micro-PPT is on the order of 1.59×10^{-7} for the two electrode micro-PPT test. The initial charge storage of $Q_0 \approx J\tau > 0.0016$ coulomb is required to sustain the pulse through the discharge. Using these operating conditions, the discharge energy was as high as 6.5 joules according to equation;

$$W = \frac{1}{2}CV^2 \quad (2)$$

Where, V is 3,600 V of surface breakdown voltage and C is a 1 μF capacitor¹². In this research, input voltages ranged from 4 to 8 V. The corresponding discharge energy was 2 joule at 1400 V (4V input) and 4.5 joule at 2110 V (8V input) (Figure 36, showing the circuit consists of high voltage converter and two 1 μF capacitors).

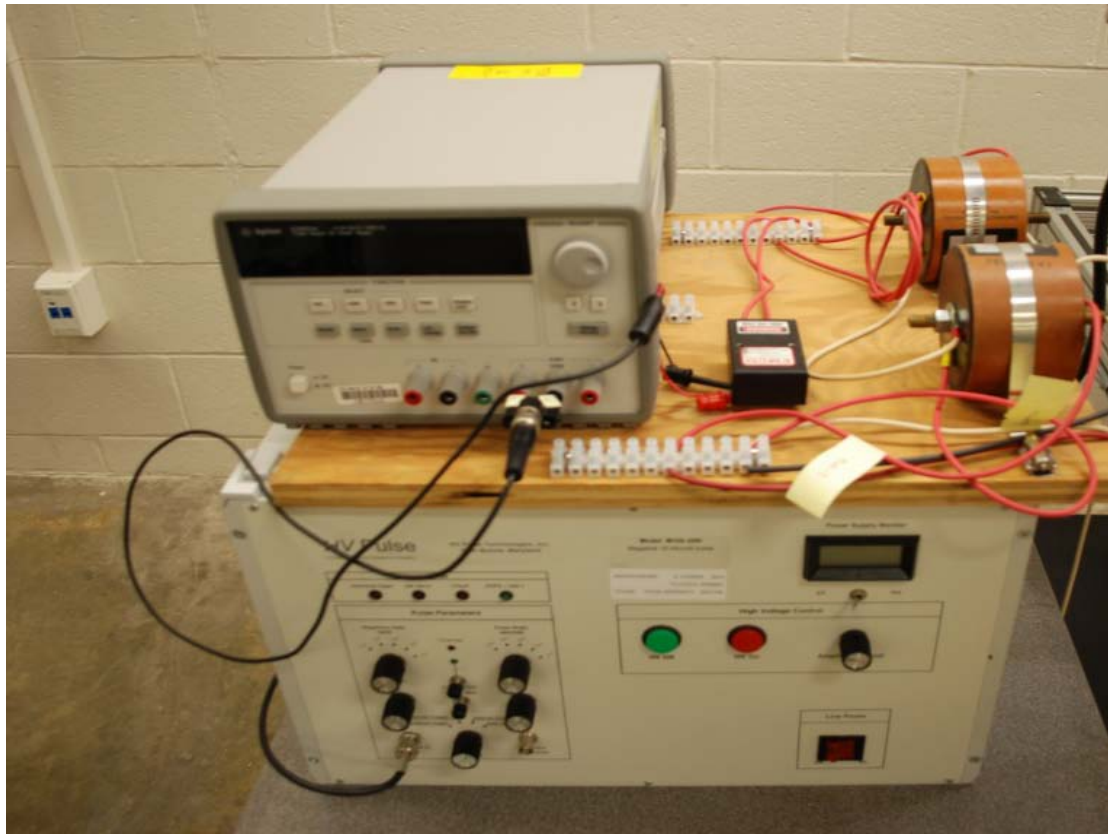


Figure 36 : Circuit using two 1 μF Capacitors Connected and High Voltage Converter

III.4. Data Evaluation Method

The start and end coordinates of each particle streak were measured using image software to determine the length of streak for each particle. After measuring the pixel numbers of the particle streak in the picture, the results were converted from pixel length

to physical length. The procedure to determine the physical scale for a single pixel involved two independent methods to increase fidelity in the measured value. One way is simply using a ruler placed in the focal plane at the PPT. The other is using the PPT tube diameter as a reference, converting the known dimension into pixels. For this configuration, the ruler showed 59 mm corresponds to 512 pixels (Figure 37), resulting in one pixel equating to 0.115 mm. With this information and the image exposure time, the velocity of the particles can then be calculated. As an example, the velocity of a particle moving through 256 pixels corresponds to 29.5 mm. If the exposure time is set at 30 μ sec, the velocity is 983 m/s.

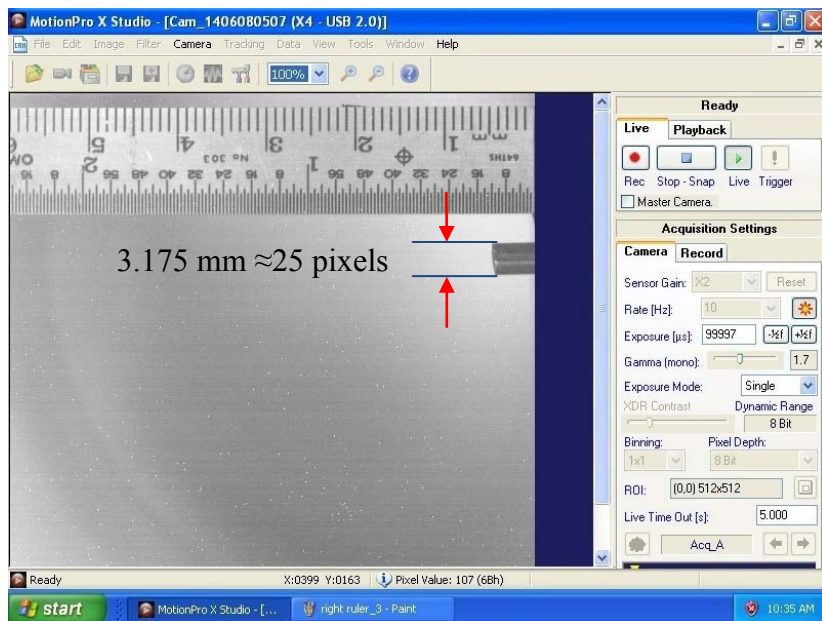


Figure 37 : Measuring the Physical Length Scale

The PPT tube measured about 25 pixels across. The physical diameter of the tube is 3.175 mm giving a one pixel dimension of 0.127 mm. There difference in the two methods resulted from a distance change from the camera to the PPT between

experimental events. Knowing the changes in the actual location of the cameras allows us to correct for any variations due to pixel/length changes. Added to this potential systemic error, using the tube diameter had to be carefully handled. The light around the outer electrode often saturated many pixels and could cause erroneous measurements of the number of pixels in one diameter. The variations of the physical pixel scale from test to test were captured and applied appropriately to ensure no unnecessary error was introduced into the final results. With this precaution, introduced error due to pixel resolution can then be quantified. Table 8 shows the average tube cross distance (pixel) and one pixel error (m/s) for each exposure time. All particles have less than a possible variance of 10 m/s for one pixel except 10 μ sec case which account for 1.2% of total particles.

Table 8 : One pixel error (m/s) in each exposure time

Frame rate	exp. time	# of particles	average X length of tube (pixel)	average Y length of tube (pixel)	x_z plane one pixel error (m/s)	y_z plane one pixel error (m/s)	Percentage # of particles
14100	20	121	22.6	22.9	7	6.9	2.4
	30	494	22.6	22.9	4.7	4.6	9.9
	40	118	22.6	22.9	3.5	3.5	2.4
	Subtotal	733					14.7
24500	10	62	23.9	24.6	13.3	12.9	1.2
	20	100	23.9	24.6	6.6	6.5	2
	30	21	23.9	24.6	4.4	4.3	0.4
	37	97	23.9	24.6	3.6	3.5	1.9
Subtotal		280					5.6
26500	14	98	25.6	25	8.9	9.1	2
	20	157	25.6	25	6.2	6.4	3.1
	24	622	25.6	25	5.2	5.3	12.5
	25	309	25.6	25	5	5.1	6.2
	30	1925	25.6	25	4.1	4.2	38.6
	34	583	25.6	25	3.6	3.7	11.7
Subtotal		3694					74

31500	28	95	-	-	-	-	-	1.9
50502	16	189	23.3	24.7	8.5	8	3.8	
Total		4991						100

III.4.1.Determining 3D Velocities

Converting the 2D images into 3D velocities requires identifying the same particles in the two different images. In the following image, a red particle trace shows how a particle moving away from the thruster will be captured by each of the cameras. The front and side cameras will capture the image shown by the orange lines. If we use representative lengths as shown in Figure 38 for an example, the length of the particle path in the front camera image is $\sqrt{3^2 + 5^2}$ and the right side camera image is $\sqrt{2^2 + 5^2}$. The actual path taken by the particle (red streak) length will be $\sqrt{3^2 + 2^2 + 5^2}$. The images from the front and side cameras will have the same vertical length if the two cameras have same exposure times. With the use of some vector math, the velocities of all distinguishable particles can then be determined by simply dividing the path length by the exposure time. The total number of particles captured from each camera was 4991 for all operational conditions, approximately 1000 particles for each power setting.

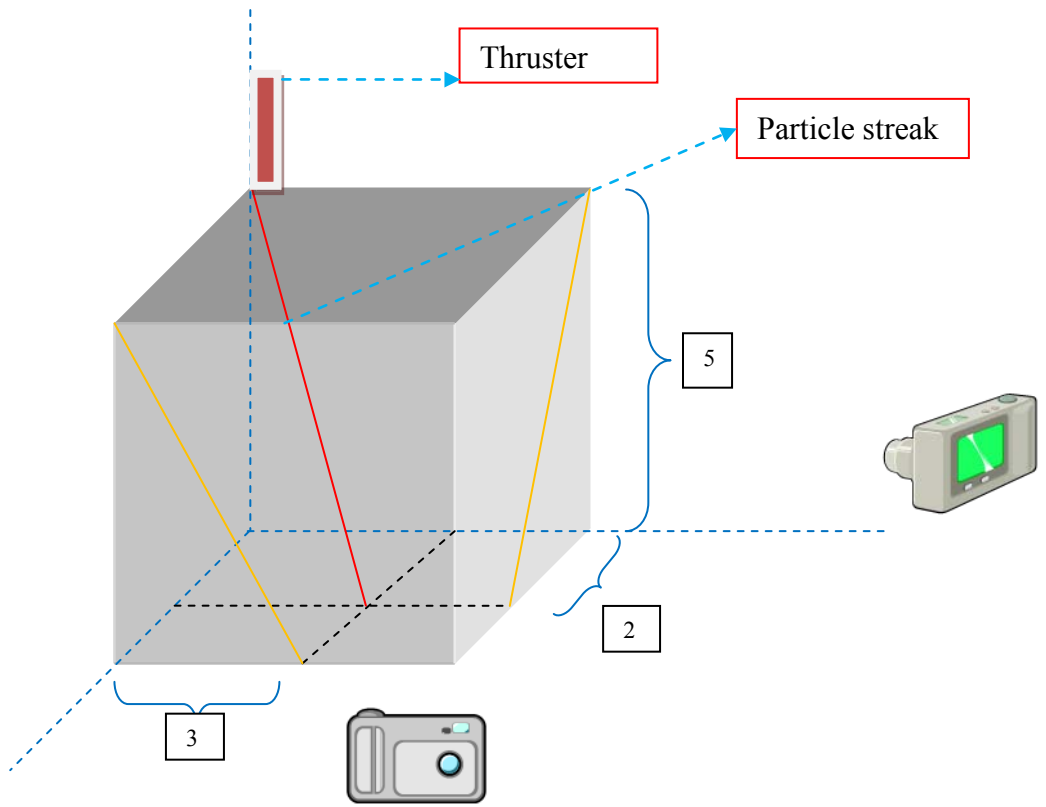


Figure 38: Measuring the Particle Streak Length

IV. Analysis and Results

IV.1. Chapter Overview

The operating range for a reliable three-electrode micro-PPT was tested. Particle data from each camera varying the energy level was analyzed for velocity and angle distribution. The velocity and angle distribution for each energy level was compared to find out the effect of energy on the velocity and angle distribution. Thruster performance (I_{sp}) for each energy level is determined from this result showing which operation results in the highest contribution to I_{sp} . Error corrections for accurate data are included in this discussion.

IV.2. Operating Energy Range for the Three-electrode micro-PPT

The HV pulse generator (Model name: M10k-20) provided the intermediate discharge energy for three-electrode micro-PPT primarily because it only contributes 0.002 Joule to the operation of the thruster but can be easily controlled (8,000 V output volt and 50 pF capacitor). The main discharge energy level ranged from 0.1 Joule (1V input voltage) to 4.5 Joule (8 V input voltage) for operating the three-electrode micro-PPT. The micro-PPT did not function at the lowest energy levels from 0.1 Joule to 0.6 Joule in spite of the consistent delivery of the seed ionization from the HV pulse generator. It simply emitted a small spark from intermediate discharge. At 1.2 Joule (3 V input voltage), the micro-PPT fired with a blue light but ejected particles were not evident because the supplied energy was insufficient to produce particles and potentially enough thrust-producing plasma to be useful. Particles were captured with the cameras over the energy range from

2 Joule to 4.5 Joule. The thruster was exercised over 1,000 times for each energy level without any problem when triggered from the function generator. The maximum input voltage employed was 8 V, 2,110 V output volts (4.5 Joule equivalent energy). Since the current power supply is limited to an input voltage of just 10.0 V. Additionally, there exists some danger to the electronic circuit above 8 V. One high-voltage converter was destroyed when operated at the highest voltage of our power supply.

Table 9 : Three-electrode micro-PPT Operability Test Results

Input (V)	1	2	3	4	5	6	7	8
Output (V)	290	760	1100	1400	1640	1840	1990	2110
Energy (Joule)	0.1	0.6	1.2	2	2.7	3.4	4	4.5
Work or not	Not	Not	Work but weak	Work	Work	Work	Work	Work

It was also noticed firing the thruster was easier in the atmosphere rather than at vacuum conditions. The thruster failed to fire at vacuum conditions on several occasions even though it worked at atmosphere with the same energy. For example, the two-electrode micro-PPT worked weakly using the HV pulse generator (0.002 Joule) in atmosphere but it did not work in the vacuum chamber at pressures below 10^{-5} torr causing significant delay in capturing the data.

IV.3. **Captured Particles**

Table 10 shows the particle numbers captured by each camera at the different operating conditions such as energy, camera frame rate and exposure time. The pictures were taken with frame rates ranging from 14,100 to 50,502 fps and exposure time range from 10 to 40 μ sec but the bulk of the data was taken at 26,500 fps (74%) and 20 to 30

μsec exposure time (77 %) as shown in Table 11. The number of total particles captured for each camera was 4991, approximately 1,000 particles at each energy level with various frame rates and exposure times.

Table 10 : Summary of Captured Particles

Main Discharge Voltage (V)		Energy (J)	Camera Frame Rate (fps)	Camera Exposure Time (μs)	Number of Particles
Power Supply (V)	Voltage (V)				
4	1400	2	26500	24	295
			26500	30	494
			26500	34	205
Subtotal					994
5	1640	2.7	26500	20	157
			26500	25	218
			26500	30	639
Subtotal					1014
6	1840	3.4	24500	10	62
			50502	16	189
			14100	20	121
			24500	20	100
			14100	30	294
			24500	30	21
			24500	37	97
			26500	30	117
Subtotal					1001
7	1990	4	14100	30	200
			14100	40	118
			26500	25	91
			26500	34	61
			31500	28	95
			26500	30	450

Subtotal					1015		
8	2110	4.5	26500	14	98		
			26500	24	327		
			26500	34	317		
			26500	30	225		
Subtotal					967		
Total					4991		

Table 11: Captured Particles Sorted by Frame Rate and Exposure Time

Frame Rate (fps)	Number of Particles	Exposure Time (μ s)	Number of Particles
14100	733	10	62
24500	280	14	98
26500	3694	16	189
31500	95	20	378
50502	189	24	622
Total	4991	25	309
		28	95
		30	2440
		34	583
		37	97
		40	118
		Total	4991

The exposure time and frame rate were varied to ensure faster particles were being captured. The higher frame rate reduces the pixel resolution size and is therefore not always the best setting for capturing distinguishable particles. The distinguishable particles are easiest to distinguish just after the spark event. The spark duration can be found from the time setting (using frequency setting) of the HV pulse generator, which

provides a seed ionization.. Figure 39 shows three consecutive pictures starting with a firing of the PPT. In the first frame the only thing visible is the light from the spark event. The streaks are then captured in the second frame of the X_Z plane. If the camera was set at a higher frame rate (for example, 20,000 fps which has 50 μ sec duration between frames), then some streaks (#1 in the second frame) may not be captured, (frame rate time interval is 31 μ sec in this case).

Another problem was capturing the particles with both cameras, Figure 39 and Figure 40. There are two reasons why particles would be missed by one or the other camera. First, a time difference between the two cameras in actually capturing images, although the same second frame should coincide due to the trigger, Figure 39. A sign indicating the particles were not taken at the same time is the light in the second frame. The second frame in X_Z plane appears later in time past the firing than the Y_Z plane. The second introduced error in capturing the same particles with the two different cameras is different focusing planes for each camera, even when there is no time difference between the cameras. Particles often have a shallow angle to the thruster centerline in one plane (for example, X_Z plane) but have a steeper angle in the other plane (for example, Y_Z plane) or vice versa. For instance, Particles #2 and #3 in the second frame in Y_Z plane cannot be found in the second frame in the X_Z plane in Figure 40.

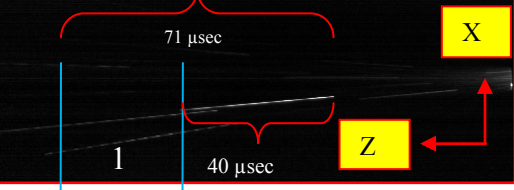
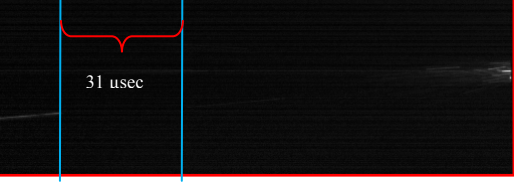
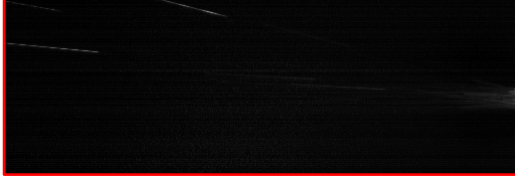
	X_Z plane	Y_Z plane
1 st frame		
2 nd frame	 <p>71 μsec</p> <p>40 μsec</p> <p>1</p> <p>Z</p> <p>X</p>	 <p>Y</p> <p>Z</p>
3 rd frame	 <p>31 μsec</p> <p>1</p>	

Figure 39: Three Consecutive Frame at 14,100 fps 40 μ sec

	1 st frame	2 nd frame
X_Z plane	 <p>1</p>	 <p>2</p>
Y_Z plane	 <p>1</p>	 <p>2 & 3</p>

Figure 40 : Different Focusing Plane (8V 26,500 fps 30 μ sec)

Figure 41 shows fast particles captured by both cameras for each energy level. To determine three-dimensional velocity, the particles must be captured by both cameras.

There is a time difference between the two cameras in many cases, Figure 41. However, we can determine the same particles in the different images by simply comparing the axial length. For images at the same exposure time, the axial length will be the same for the particles taken at different positions. This is the method described in the 3D velocity evaluation methods in chapter 3.

Condition & Velocity	Image : X_Z plane & Y_Z plane
4V 26500fps 30 μ sec	
1001 m/s	
5V 26500fps 20 μ sec 774m/s	 

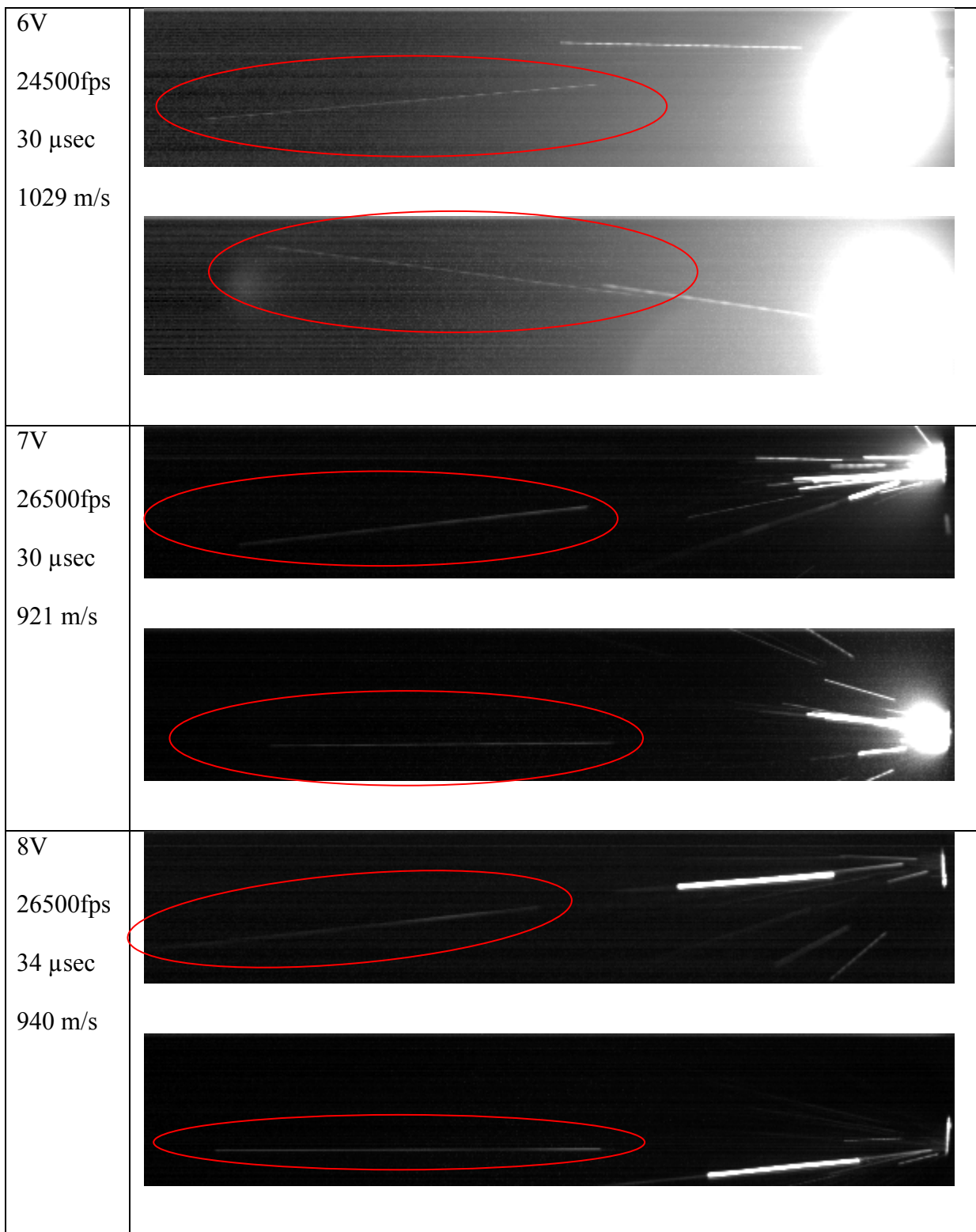


Figure 41 : Fast Particles at Each Operating Condition.

Also, some cases had very fast particles that could not be distinguished due to the number of particles captured by one camera as shown in Figure 42.

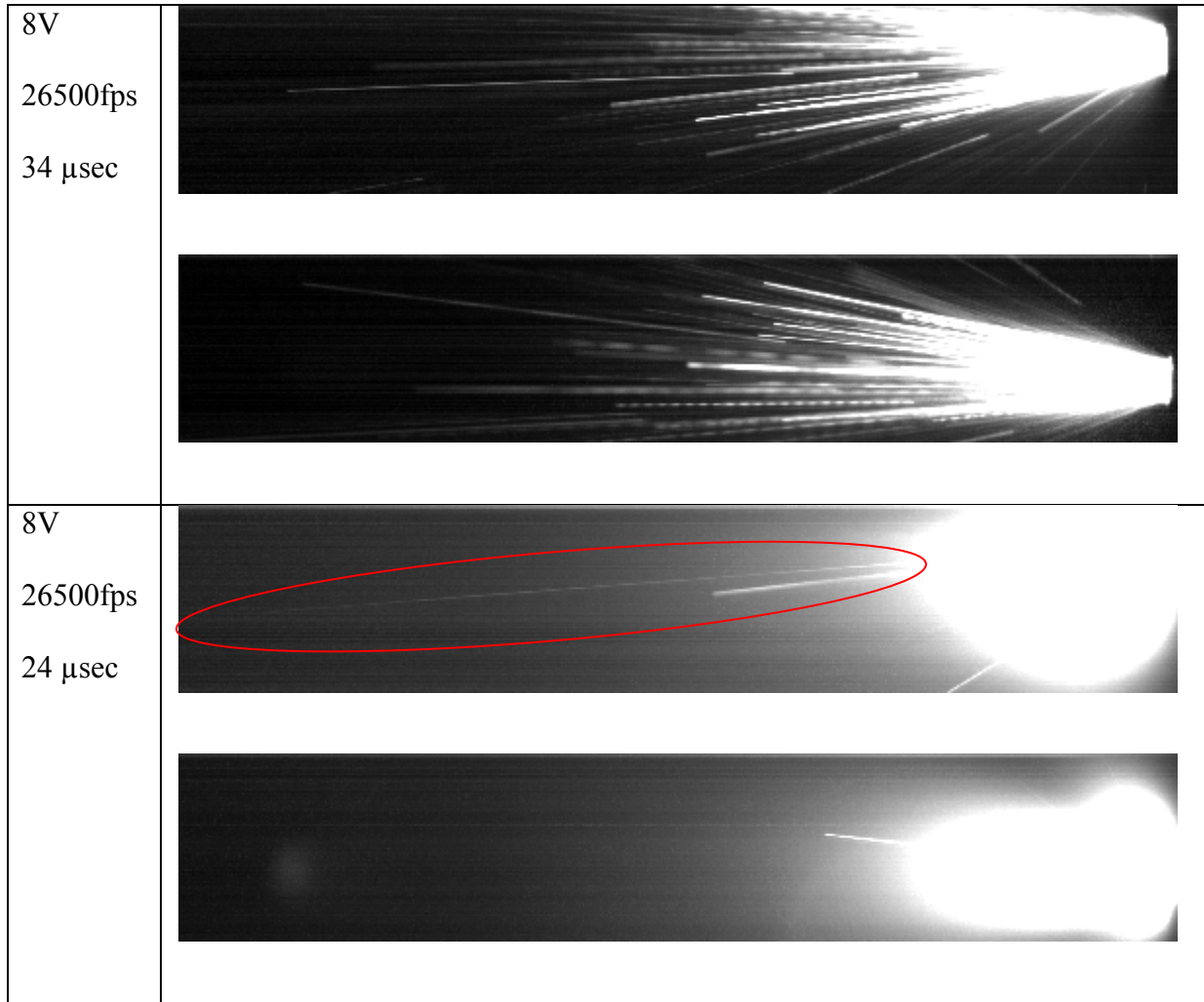


Figure 42: Fast Particles

IV.4. Angle Error Correction for Tilted Thruster

The thruster axis was tilted a slightly ($2 - 3^\circ$) from the picture axis. The thruster axis in the X_Z plane was tilted to the right and the thruster axis in Y_Z plane was tilted to the left from the picture axis when looking at the pictures with the thruster at the top of the image. The sign of the angle is defined as positive angle left and negative right from the

centerline of the image with the thruster at the top of the image. For quantifying the velocities and taking into account this slight misalignment of the thruster with the image, four angles are defined. Angle α for the X_Z plane and β for the Y_Z plane are the actual particle trajectory (red line) angle from the thruster Z axis (dotted line). , The angle the particle path forms with the image Z axis (black line) is designated angle θ and angle γ is the angle between the image Z axis and the thruster Z axis as shown in Figure 43.

	Positive angle streak	Negative angle streak
X_Z Plane		

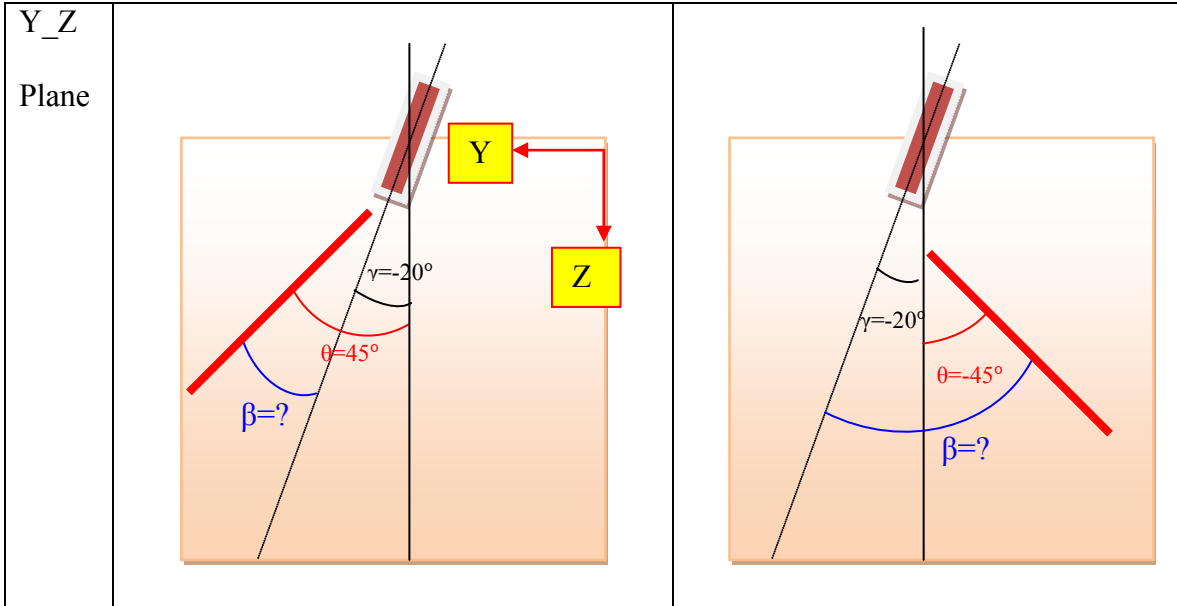


Figure 43 : Angle Definitions

In case of a positive particle streak angle in X_Z plane (left upper figure), the streak angle (θ) is positive and the image Z axis (γ) is also positive because it is left of the thruster Z axis. We want to know the angle between the particle path and the thruster Z axis (α for X_Z plane and β for Y_Z plane). So the path angle (α) is $\theta + \gamma$ (in the first example, 65°). In the case of a negative particle streak angle in the X_Z plane (right upper figure), the particle has a negative path angle (α) and a positive image Z axis angle (γ) from the thruster. So, the actual particle path angle (α) from the thruster become $\theta + \gamma = (-45^\circ) + 20^\circ = -25^\circ$. The X_Z plane exhibited only positive γ angles in this research. In contrast, Y_Z plane was captured with negative γ angles. Particle streak angles (θ) were positive and the image Z axis was negative in the left bottom figure corresponding to β of $\theta + \gamma = 45^\circ + (-20^\circ) = 25^\circ$. Particle streak angles were negative and image Z axis was also negative in the right bottom figure ($\beta = \theta + \gamma = -45^\circ + (-20^\circ) = -65^\circ$).

The particle velocities are then resolved from these angles and measured velocities from the images. Designations used for the actual particle velocities are V_x , V_y , V_z , V_{x_z} , V_{y_z} , $V_{x_y_z}$. In the image reference frame, intermediate names used were $V_{x \text{ image ref}}$, V_y image ref, V_z image ref, V_{x_z} image ref, V_{y_z} image ref and $V_{x_y_z}$ image ref. Velocity with respect to the image are then determined as $V_{x_z \text{ image ref}}$ (red streak) can then be used to calculate V_x and V_z components with respect to the thruster, $V_{x \text{ thruster ref}}$ and $V_{z \text{ thruster ref}}$ in Figure 44.

	Positive angle streak	Negative angle streak
X_Z Plane	<p>Diagram illustrating the velocity component in the X-Z plane for a positive angle streak. A red arrow labeled $V_{x_z \text{ picture ref}}$ represents the measured velocity. A dashed blue arrow labeled $V_{x \text{ picture ref}}$ represents the velocity component along the X-axis. A dashed red arrow labeled $V_{z \text{ picture ref}}$ represents the velocity component along the Z-axis. A solid red arrow labeled $V_{z \text{ thruster ref}}$ represents the velocity component along the Z-axis of the thruster. A dashed red arrow labeled $V_{x \text{ thruster ref}}$ represents the velocity component along the X-axis of the thruster. The angle between the X-axis and the thruster axis is labeled θ. The angle between the Z-axis and the thruster axis is labeled γ.</p>	<p>Diagram illustrating the velocity component in the X-Z plane for a negative angle streak. Similar to the positive angle streak diagram, it shows the measured velocity $V_{x_z \text{ picture ref}}$ (red arrow), velocity components $V_{x \text{ picture ref}}$ (dashed blue arrow) and $V_{z \text{ picture ref}}$ (dashed red arrow), and the thruster velocity components $V_{z \text{ thruster ref}}$ (solid red arrow) and $V_{x \text{ thruster ref}}$ (dashed red arrow). The angle θ is between the X-axis and the thruster axis, and the angle γ is between the Z-axis and the thruster axis. The angle α is the angle between the Z-axis and the measured velocity vector $V_{x_z \text{ picture ref}}$.</p>

Figure 44 : Velocity Component in Thruster Coordinates.

We know the angle α equals $\theta + \gamma$. So the $V_{x \text{ thruster ref}}$ and $V_{z \text{ thruster ref}}$ are determined as below.

$$V_{x, \text{thruster ref}} = V_{x_z, \text{picture ref}} \sin \alpha \quad (2)$$

$$V_{z, \text{thruster ref}} = V_{x_z, \text{picture ref}} \cos \alpha \quad (3)$$

It can also apply to Y_Z plane.

$$V_{y,thruster\ ref} = V_{y_z,picture\ ref} \sin \beta \quad (4)$$

$$V_{z,thruster\ ref} = V_{y_z,picture\ ref} \cos \beta \quad (5)$$

IV.5. Velocity Distribution

The radial and axial velocity components as well as magnitude of all particles is calculated using physical particle path length and exposure time as mentioned in chapter 3. The data is sampled using an average velocity with proper ranges for each velocity component and approximated with a normalized distribution using a Gaussian function. Added to the error quantified from the data analysis technique and system bias, variations are quantified from the statistical distribution of the results. Normalized distributions for each data set were fit to the data by varying the mean (b), scale (a) and standard deviation (c) of Gaussian function:

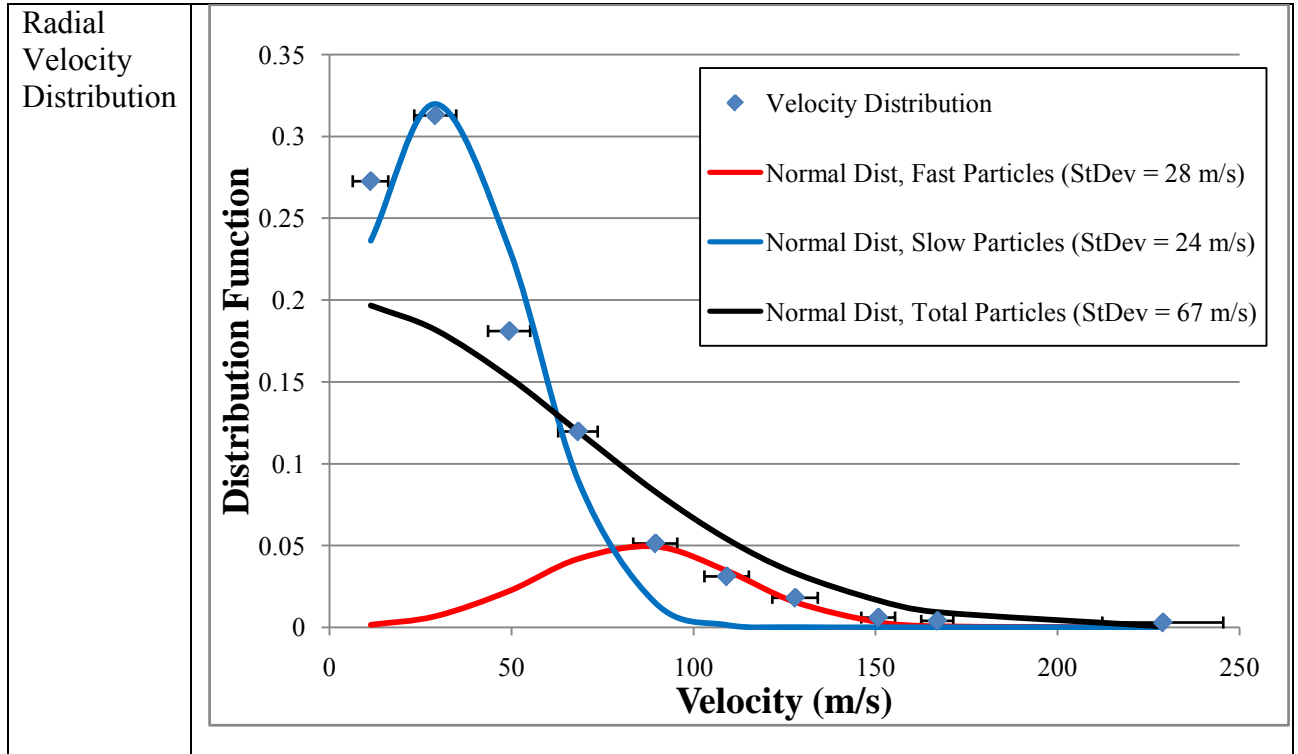
$$f(x) = ae^{\frac{-(x-b)^2}{2c^2}} \quad (7)$$

The scale (a) represents the height of the curve's peak while mean (b) is the position of the center, and (c) changes the width of the bell shaped graph²¹.

IV.5.1. Comparing 3D Velocity Distributions with Previous 2D Velocity Distributions

The velocity distribution at 4V input voltage (2J) is shown in Figure 45. The distribution of the velocity for the radial components is similar to the distribution for the velocity magnitude and axial distribution but with smaller standard deviations for the Gaussian distributions as shown in Figure 45. These results agree with previous result for the 2D velocity distributions. The velocity distributions exhibit two distinct regions. One region, for velocity magnitude distribution (below 300 m/s) appears to follow a trend

with a 110 m/s standard deviation. Higher speed particles (above 300 m/s) have a standard deviation of 130 m/s. Previous results only exhibited one normal distribution. The same trend was present at all operating conditions. The other Figures for each energy level will be presented in Appendix B.



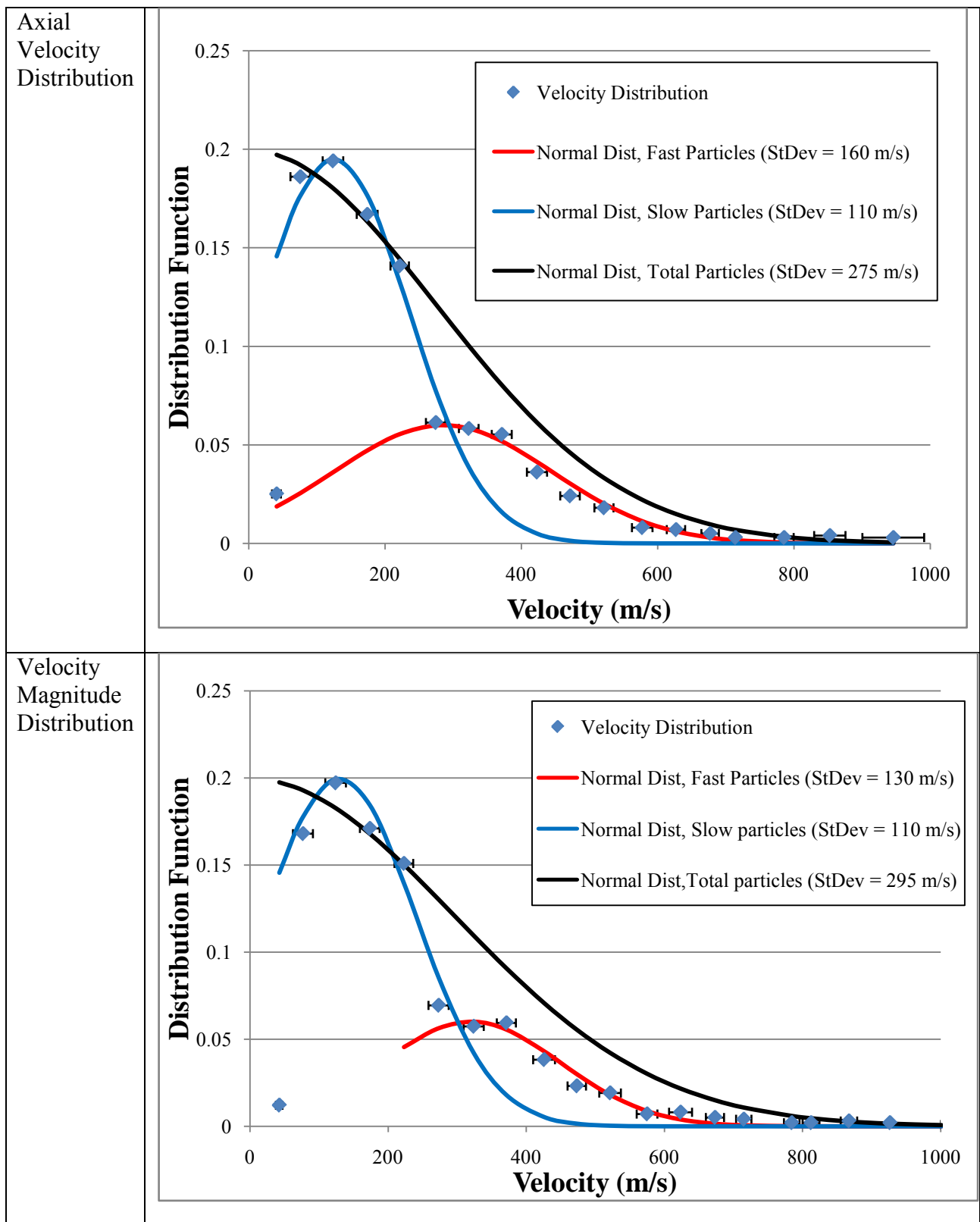
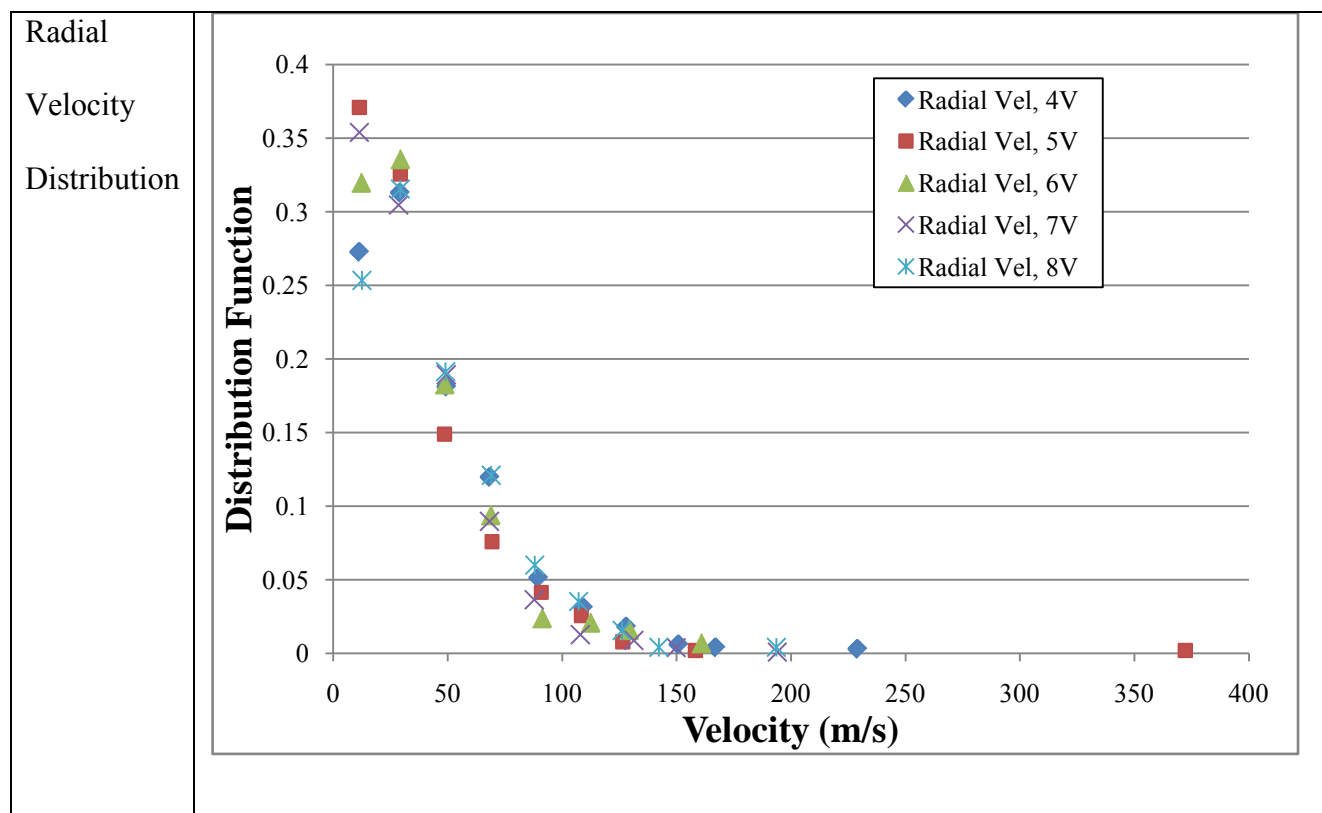


Figure 45 : Velocity Distribution at 4V (2.2J)

IV.5.2. Compare Velocity Distribution with Each Energy Level

The velocity distributions will be compared with each energy level for each velocity component. As shown in Figure 46, it looks similar to other velocity data which means the energy does not directly affect the velocity distribution of the emitted particles. The particles are being ejected by the expansion of the gas at the surface but the high speed ionized gas is not adding any further momentum to these particles.



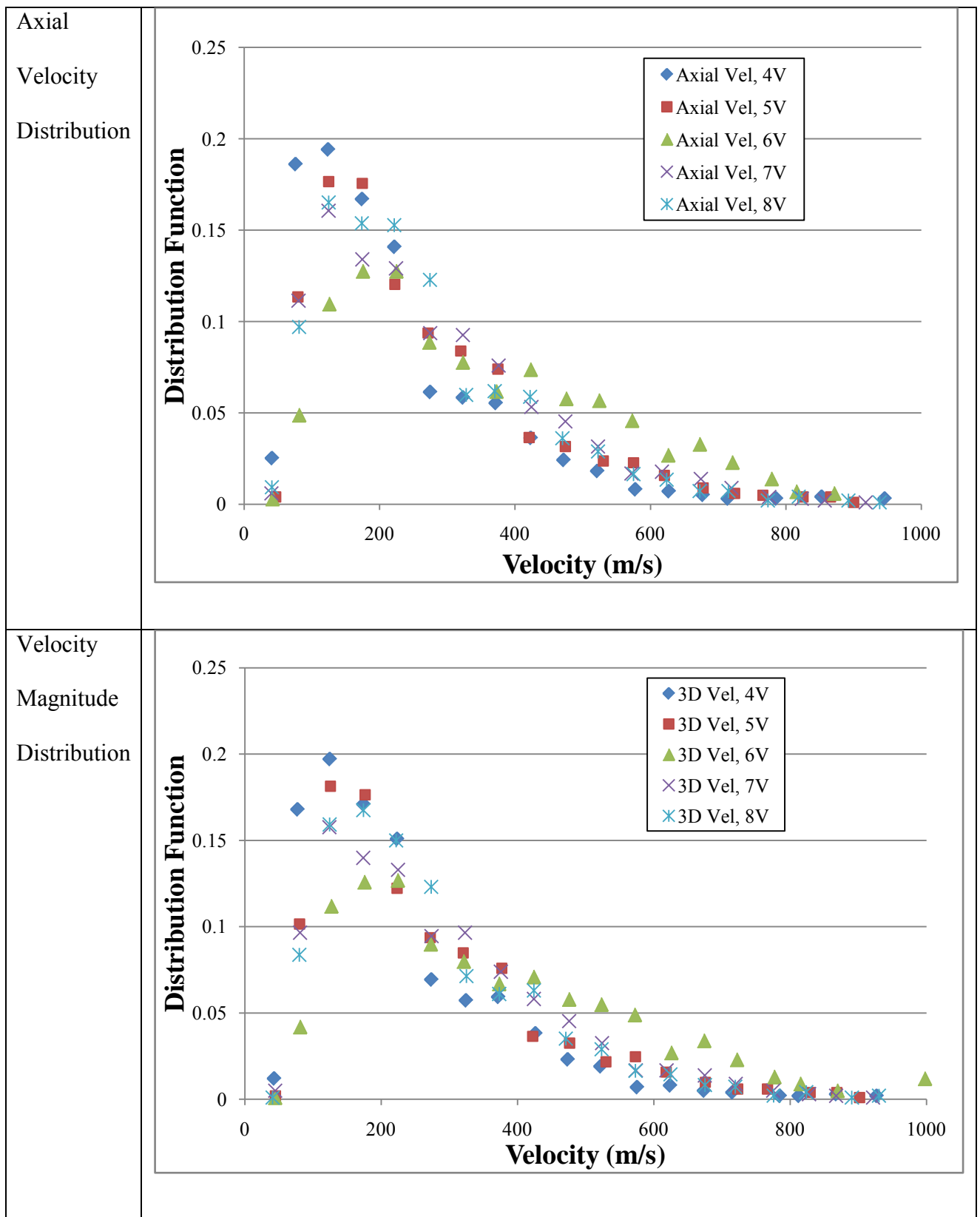


Figure 46 : Comparing Velocity Distribution With Each Energy Level.

IV.5.3. Performance Contributions

One can calculate specific impulse (I_{sp}) values with known gas exit velocity.

When assuming the particles which have an axial direction velocity component contribute the total thrust, I_{sp} contributions can be estimated from the average axial velocity using the following equation:

$$I_{sp} = \frac{v_{ex}}{g_0} \quad (8)$$

Table 12 shows the average velocity and I_{sp} contribution for each energy level. As shown in the table, the maximum I_{sp} , 35 sec, occurs at 3.4J. Even though this might suggest an optimal operation for this thruster, the variation in the measurements and the statistical variance in the results suggest only the solid particulates being ejected provide an additional 25 – 35 seconds of I_{sp} .

Table 12 : I_{sp} Contributions for Each Operating Conditions

Input voltage (Energy)	4 V (2 J)	5 V (2.7 J)	6 V (3.4 J)	7 V (4.0 J)	8 V (4.4 J)
Average axial velocity (m/s)	215	256	345	270	258
I_{sp} (sec)	22	26	35	28	26

IV.6. Angle Distribution

The solid angles of the particles were also analyzed using the same velocity data. Solid angles can simply be determined from the velocity components. We know all velocity components such as radial and axial components with respect to the thruster from the velocity data. Solid angle is determined directly from the trigonometric function:

$$\Omega = \tan^{-1}(V x_y \text{ thruster_ref} / V z \text{ thruster_ref}) \quad (9)$$

The solid angle (Ω) is 36° using the example equation $\tan^{-1}((2^2+3^2)^{1/2} / 5)$ in Figure 47.

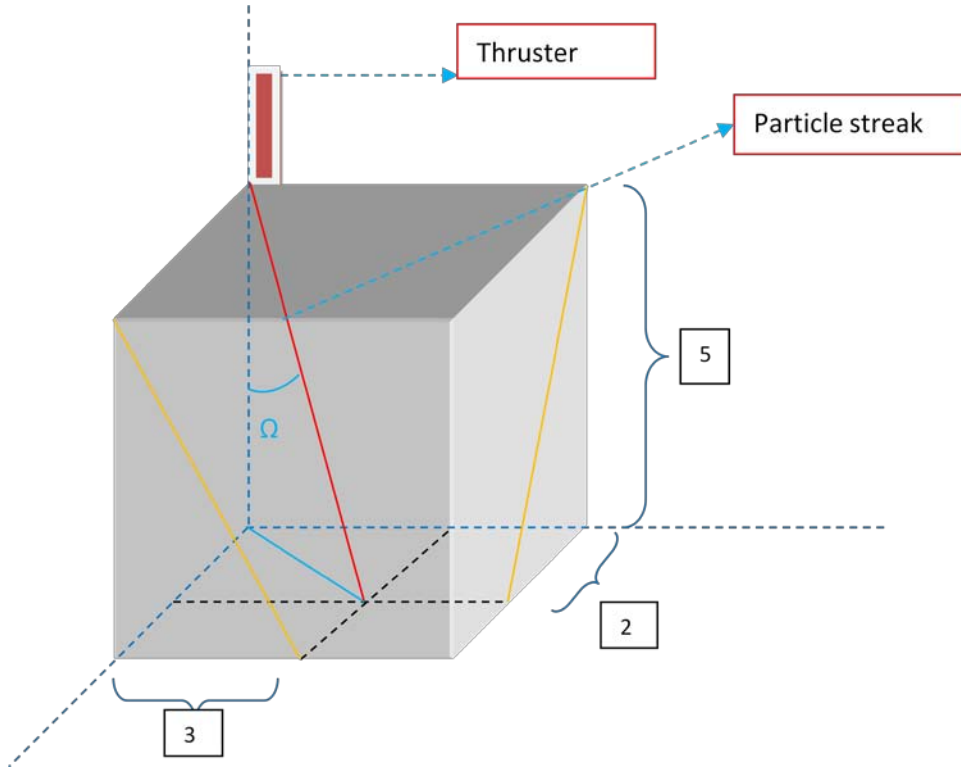


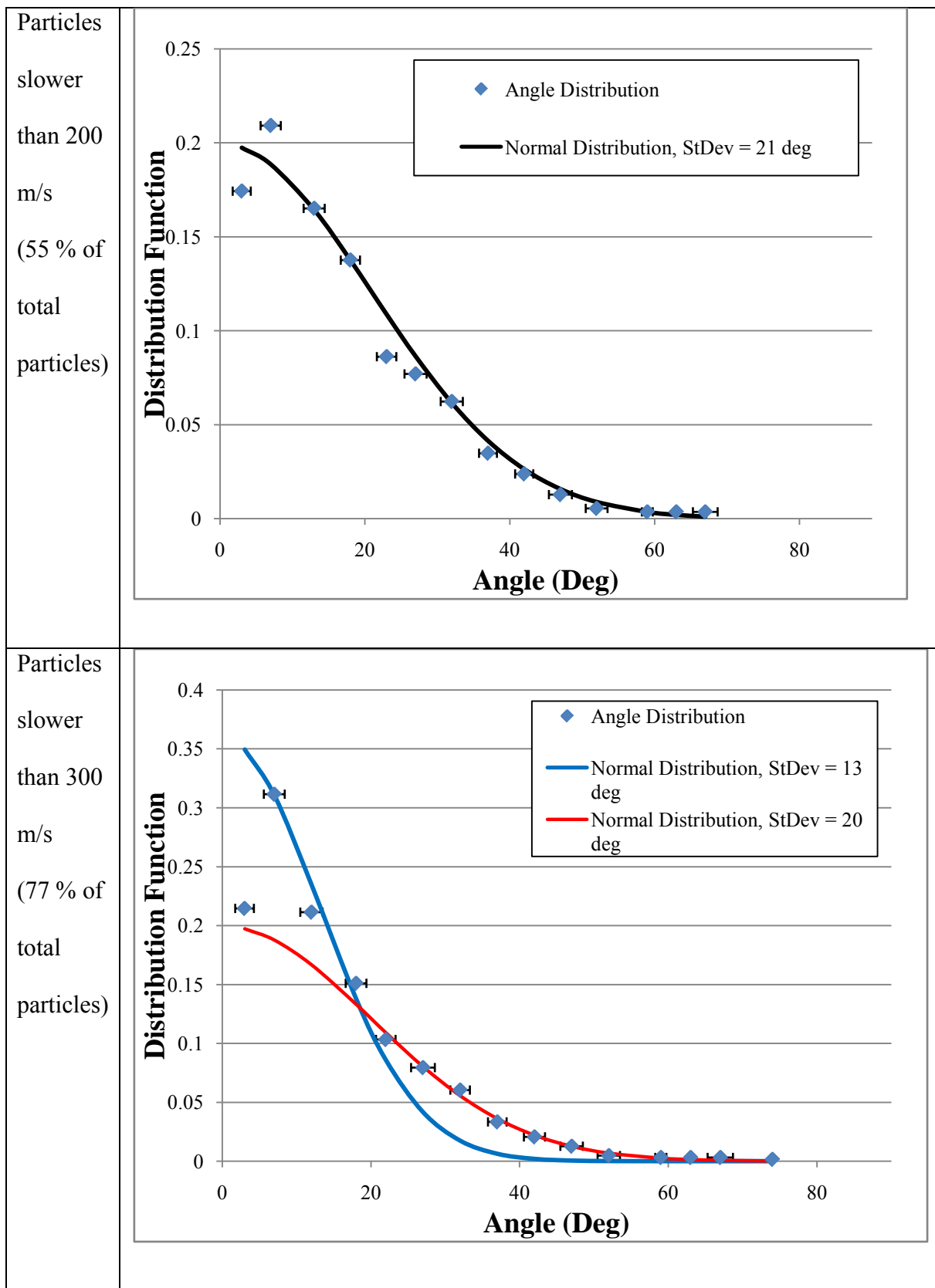
Figure 47 : Solid angle calculation

The angles were sampled similarly to the velocity data to create distribution functions using average values of proper ranges, 5 degrees per range in this study. Normal distributions for the angle data were made using the same technique as for velocity distribution. The graph was also adjusted using parameter a , b and c to fit the sampling data.

IV.6.1. Comparing Solid Angle (3D) with 2D Angle Distribution

The solid angle distributions are shown for the particles slower than 200 m/s, slower than 300 m/s and faster than 300 m/s at 4V input voltage in Figure 48. Other angle distributions for other energy level will be shown in Appendix C.

The result matches previous results based on mass deposition tests with a two-electrode micro-PPT as shown in Figure 14, Figure 15 and Figure 16 in chapter 2. However, this research is different from these results in that the angle distribution peaks around 45 degrees for slow particles as shown in Figure 9. The particle count peaks at around 10 degrees when all particles are considered in this research. A significant difference between previous and present research is the data was obtained for different micro-PPT designs. Previous research used a two dimensional result for the two-electrode micro-PPT. However, the data here is obtained from three-dimensional space and three-electrode micro-PPT in this research. There is also a difference of energy operating conditions used for each test but the energy is not affecting the angle distribution which will be explained next.



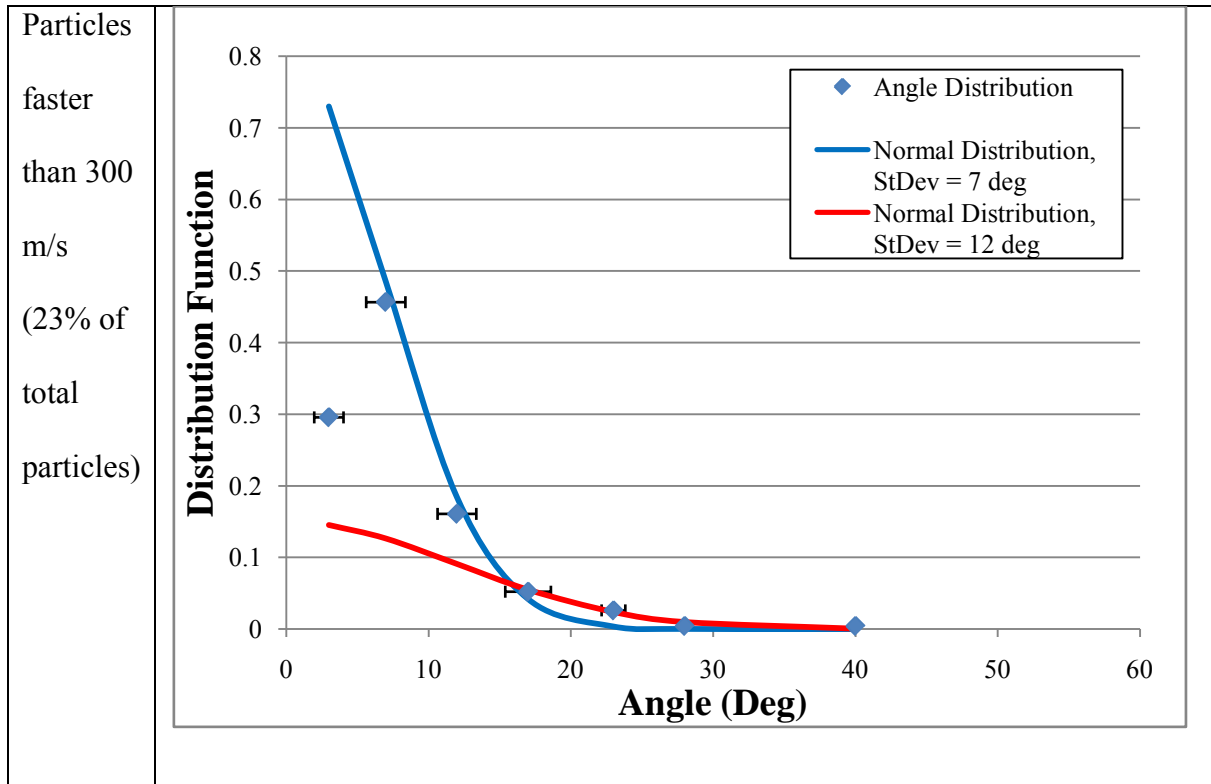


Figure 48 : Angle distribution at 4V (2J)

The normal distribution fit to the results suggests the particle counts peak at 0 degree but the data show a reduction of the number of particles below 10 degrees. The design of the thruster is the primary reason for this relationship. The three-electrode micro-PPT has three electrodes. The center and intermediate electrodes provide the intermediate discharge. This discharge will generate gas at this surface along the centerline which will start to expand before particles and gas from the main discharge are generated. This expanding gas will naturally push the particles away from the thruster centerline. Michael Keidar and Iain D. Boyd developed a model for the plasma plume in near field of this type of thruster. They used the two electrode micro PPT for their working example. The electromagnetic ($j \times B$) acceleration is the main mechanism in this thruster. Therefore, the near-field plasma plume is a crucial part of the thrust generation

process²². These researchers showed results of Carbon and Fluorine (components of this propellant) ion density decreasing with radial distance as shown in Figure 49.

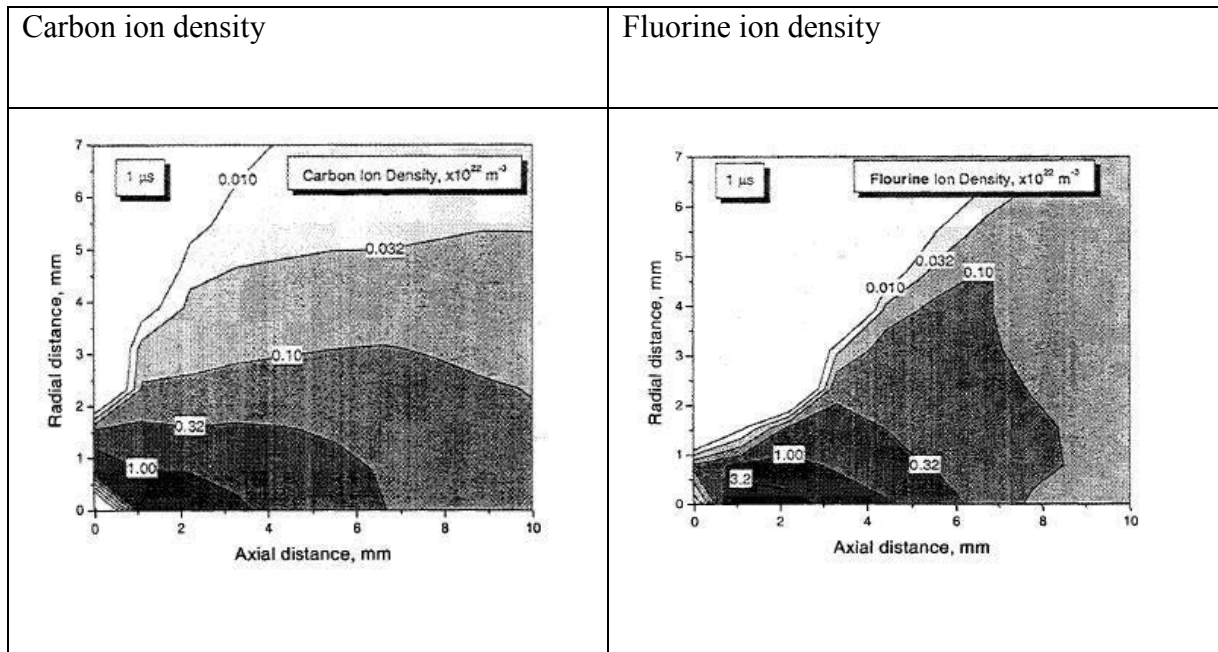


Figure 49 : Profile of ion density at 1 μ sec after firing²²

From the result of the plume profile of the two-electrode micro-PPT, one can expect the plume of the three-electrode micro-PPT as shown in Figure 50 to behave similarly. Particles from main discharge will be deflected in a similar fashion as the plume of the thruster expands, Figure 50.

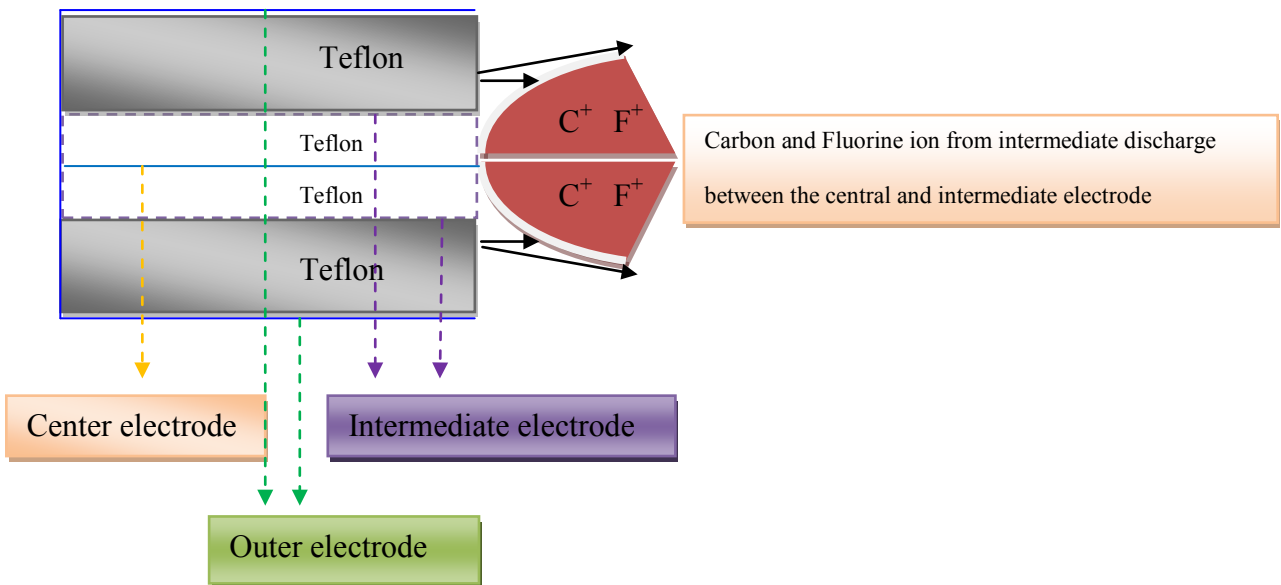
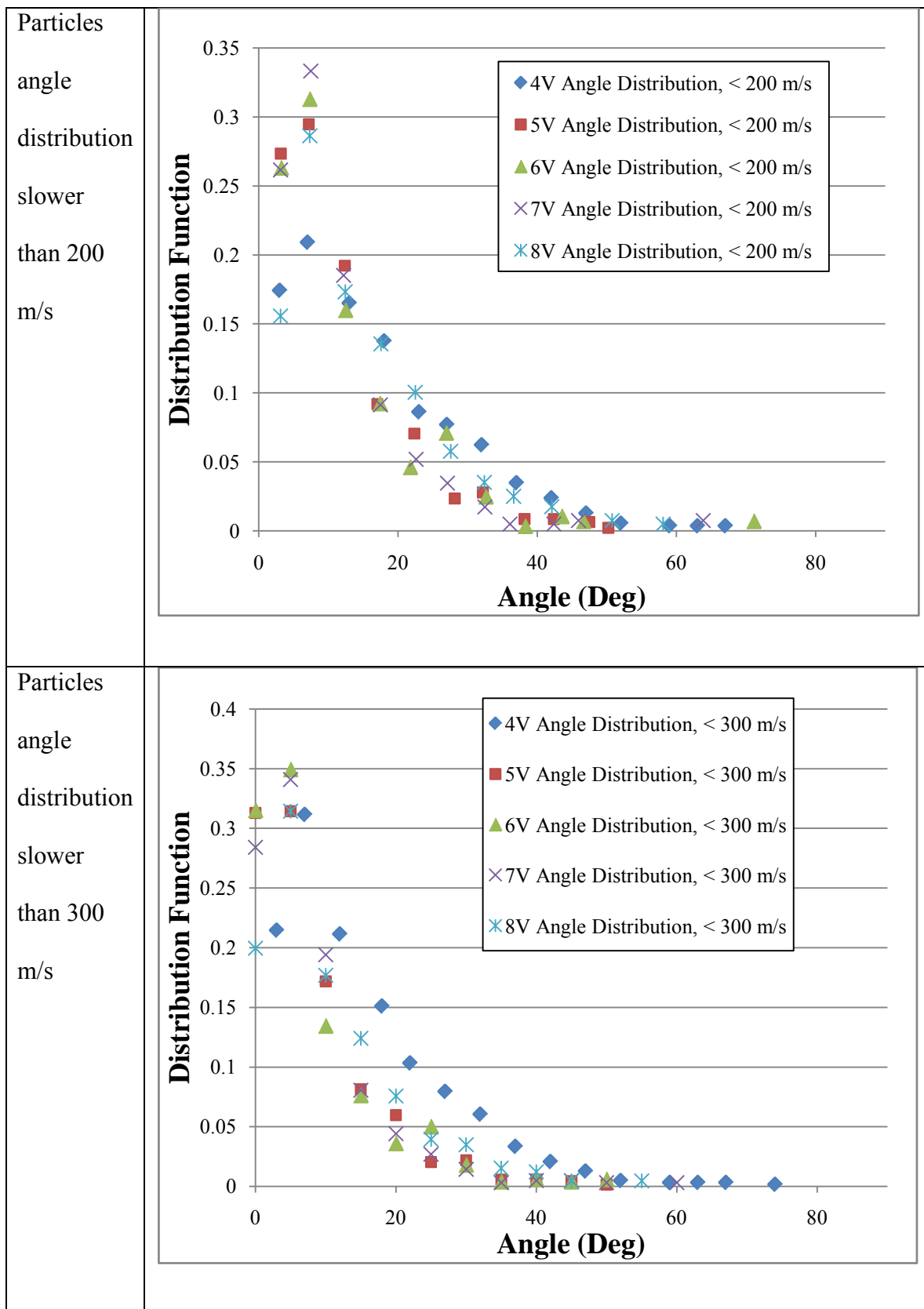


Figure 50 : Profile of plume from the main discharge of three-electrode micro PPT

IV.6.2. Comparing Solid Angle Distribution With Different Energy Levels

The angle distributions are compared at different energy levels in Figure 51.

These profiles also have similar profiles to each other suggesting energy does not affect the angle distributions appreciably at these operating conditions, the same conclusion as that of velocity distributions.



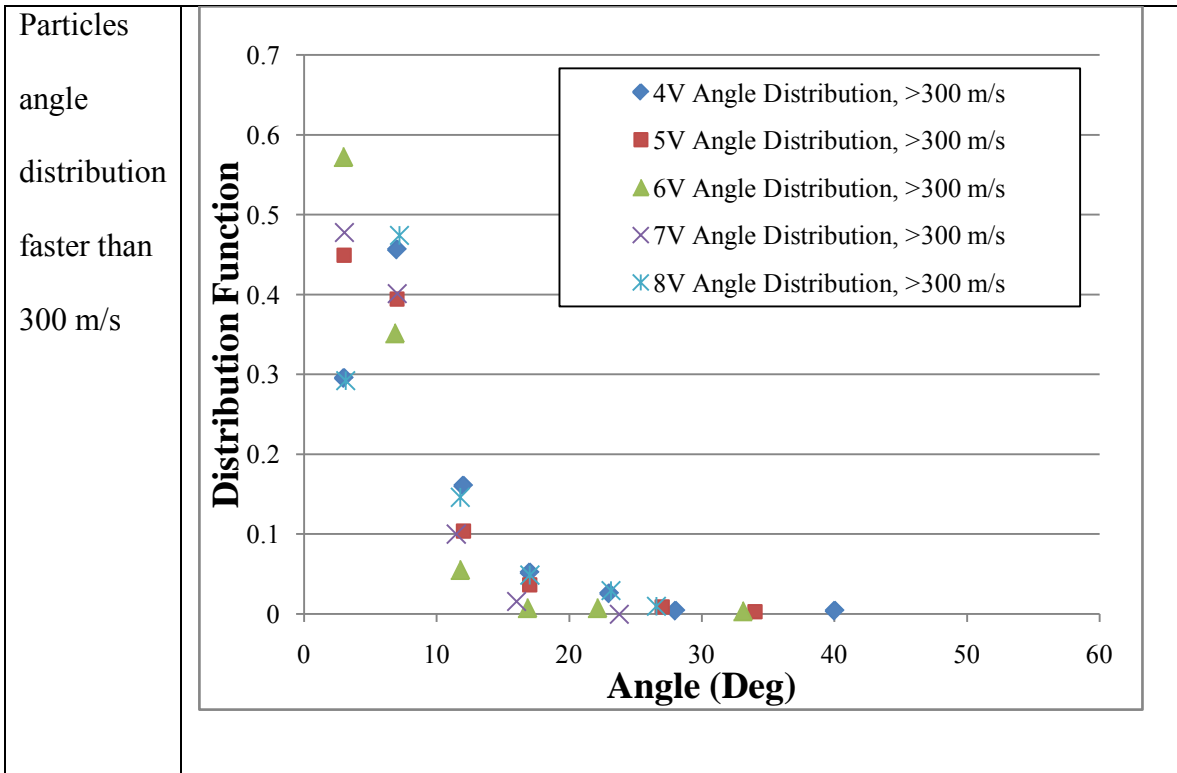


Figure 51 : Comparing angle distribution with each energy level.

IV.6.3. Average Velocity Versus Angle Range

To explore the relationship between particle velocity and angle distribution, average velocity versus angle range for each operating condition was calculated and shown in Figure 52. The data shows the shallow angles have higher average velocities. One can also see the average velocity profiles of each energy level are similar to each other

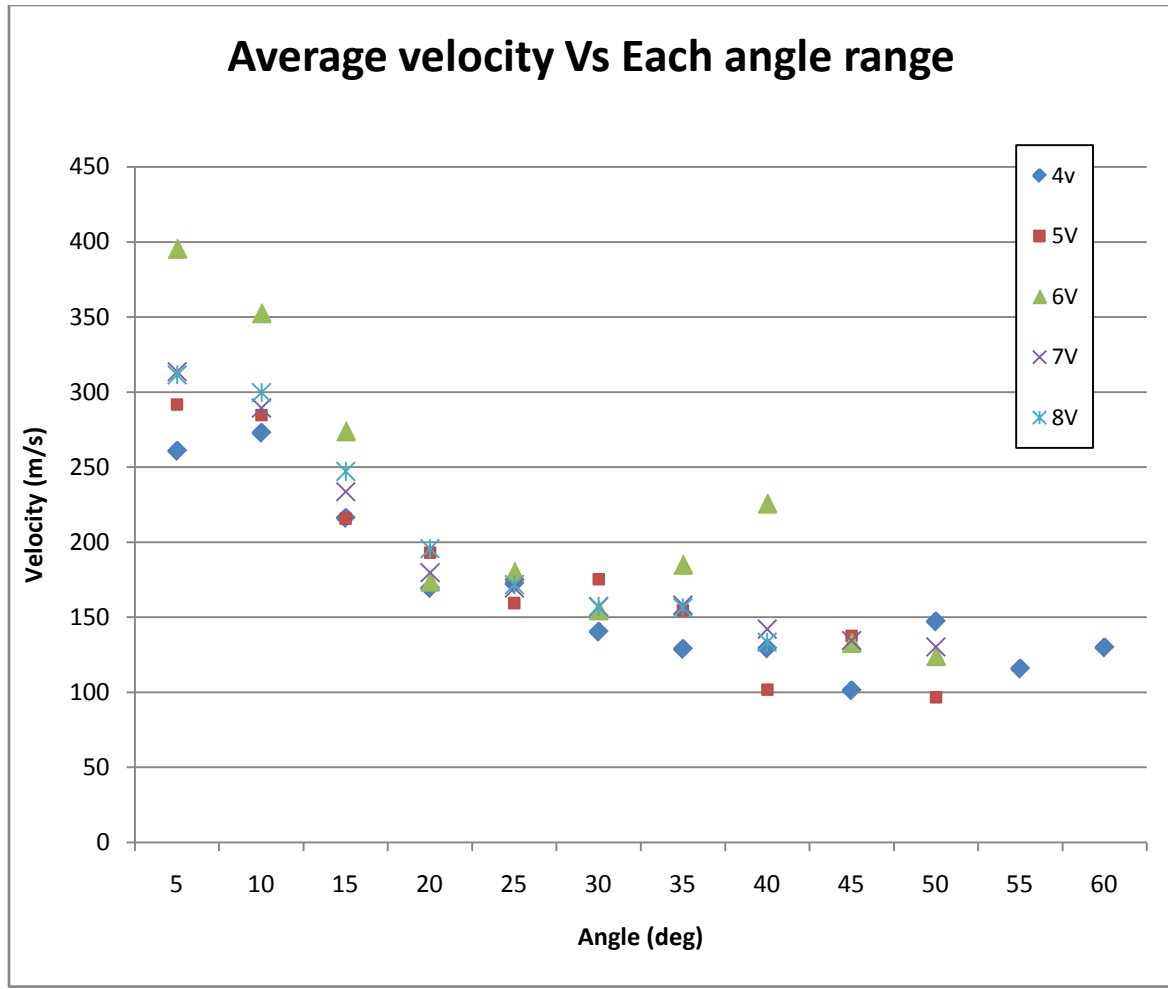


Figure 52 : Average Velocity Versus Angle

The velocity standard deviation of these particles for each angle range was also examined. Figure 53 shows the particle's standard deviation of velocity as function of angle. The standard deviation shows particles exiting closer to the centerline (shallow angles) have larger values for standard deviation as we expected suggesting the velocity for these particles are varies over a wider range. One can also see standard deviation of velocity does not depend on discharge of energy for the thruster. The fastest particles exit closer to the center line as can be seen from the results and the standard deviation of the velocity distribution. The larger standard deviation for the particles exiting near the

centerline suggest both slow and fast particles are exiting near the centerline, at shallower angles. The relatively lower velocity variance at more divergent angles (steeper angles from the centerline) suggests only slower particles are present.

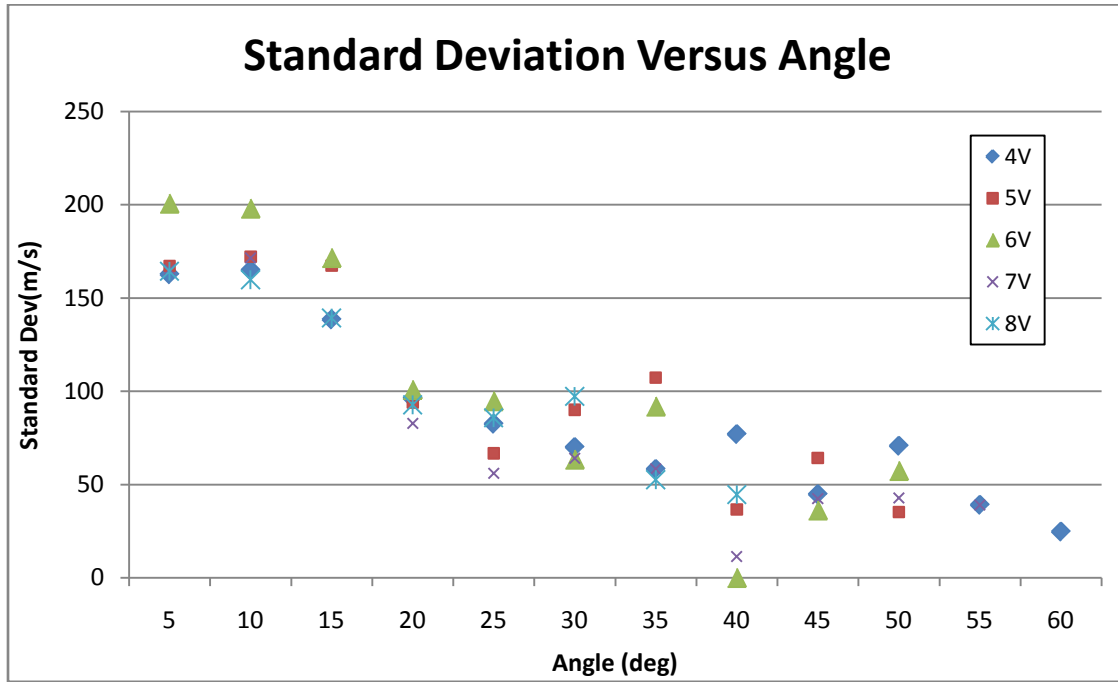


Figure 53 : Standard Deviation Versus Angle

IV.7. Summary

Both intermediate and main discharge energy levels are important to operate the reliable three-electrode micro-PPT. This research used only one intermediate discharge energy level, 0.002 Joule and varied the main discharge energy level from 0.1 to 4.5 Joule. The main discharge energy ranged from 2 to 4.5 Joule and provided good results for firing the PPT. Velocity and angle distributions were analyzed for each energy level using the particle data from the high-speed cameras. The data shows the angle and velocity distributions were not appreciably affected by energy levels explored by this

research. However, the particles do contribute to I_{sp} . Particle counts for the angle range from 0 to 10 degrees is not the highest distribution in a three-electrode micro-PPT, a different result from previous mass deposition profile results using a two-electrode micro-PPT.

V. Conclusions and Recommendations

V.1. Overview

Conclusion for the three-electrode micro-PPT operability, velocity and angle distribution and energy effects on this distribution will be summarized. The performance contribution from particle velocity and relationship between velocity and angle will be concluded. To get a more reliable data and for future work, some recommendation are also provided.

V.2. Conclusions

V.2.1. Operability

The three-electrode design was tested to determine if it is more reliable than a two-electrode micro-PPT or not. When using the three-electrode micro-PPT, it proved more reliable than a two-electrode design. Three-electrode micro-PPTs worked whenever the seed ionization (using 0.02 Joule intermediate discharge energy) was triggered and the main discharge energy was sufficient (4 V input, 2 Joule). A two-electrode micro-PPT was operated intermittently for this research as high as an energy level of 4.5 Joule. The energy range for a reliable thruster operation was from 2 Joule to 4.5 Joule in this research.

V.2.2. Velocity and Angle Distribution

Velocity distribution helps understanding the contribution to thrust provided that the mass consuming rate is known. It also provides the particle behavior and potential

vehicle contamination. The faster particles have shallower angles than slower particles and the standard deviation of shallower particles is higher than the steeper particles.

This research showed similar results for angle distributions to previous mass deposition distributions. From the point of view of a contamination issue, it supports the previous conclusion that sensitive equipment such as solar array, optical instrument and star tracking cameras should not be placed within 60 degrees of this type of thruster.¹³

V.2.3. Performance contribution

The solid particulates being ejected from the three-electrode micro-PPT provide an additional 25 – 35 sec of I_{sp} when varying the energy levels.

V.2.4. Energy Effect on Angle and Velocity Distribution

The velocity and angle distributions did not show significant effects from a varying energy operating condition.

V.3. Recommendations

V.3.1. Operability and Circuit Design

Further studies are needed to optimize seed energy to determine the minimal energy consumption for this device. Typically, the trigger discharge energy is about 2% of the main discharge energy level⁸. The seed energy was set at 0.002 Joule (8 kV output voltage and 50 pF capacitor) for this research, far below the 2% (0.1 – 0.2 % of the main discharge energy in this research). The seed energy can be varied by adding an external capacitor to the same HV pulse generator input.

V.3.2. Capturing the Particles

A better camera able to capture a larger plume area can improve the results and increase the number of particles captured with the same interrogation area. Limited area for the image decreases the data accuracy for both velocity and angle distributions. It was difficult to capture the same particles from the both camera. Being able to synchronize both cameras easily will also reduce errors introduced from frame rates and exposure times which means the particles have same positions (coordinates) and same length in Z direction at the same frame.

V.3.3. Velocity Distributions and Performance Contribution

Particle Image Velocimetry (PIV) could also be used to automate the process of converting observed particles to velocities. Automatic software saves a lot of time converting the raw data to particle velocity if available. This well developed ability can capture more particles and provide more reliable data.

Tests to quantify mass consumption rate will also provide a missing piece of the performance equation;

$$F = (\dot{m} \times V_{exit}) \quad (10)$$

Where, F is thrust, \dot{m} is propellant consumption rate and V_{exit} is propellant exit velocity.

The contribution to I_{sp} in this research is small when comparing to total PPT I_{sp} values for thrusters such as the LES 8/9's 1000 sec or NOVA's 850 sec²³. Actual thruster I_{sp} values can be adjusted, though, by the contributions measured here. A measured thrust value from a torsional balance will give more quantifiable ways to determine propellant exit

velocity of the micro-PPT and the contribution from the average value of particle's velocity after measuring the propellant consumption rate.

V.3.4. Angle Distributions

More tests using three-electrode micro-PPT focusing on mass deposition rate as well will provide valuable information contamination issue. This research focused on providing accurate data for axial image along with the thruster. For contamination standpoint, focus on radial image of the particles becomes very important. For that, it needs the particles capturing using the camera set of right upper side in Figure 32.

Appendix A: Camera Operation

To operate the cameras, make sure all cable connections are good and open the Motion Pro software. Select the “Cameras” in Figure 54 and click the “open” in Figure 55. All connected cameras will appear in the box.



Figure 54: First screen of Motion Pro software when it opens

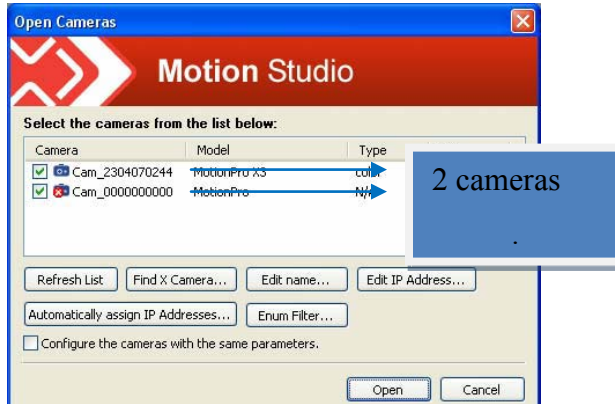


Figure 55: After selecting the “Cameras”

There are four main menus as shown in Figure 56; live, playback, camera and record. The live menu provides functions such as record, live, stop and trigger. The “Trig” button can only be activated after hitting the “Rec” button when the record mode is selected as “circular” or “BROC”. The “Live” button in live mode is for real time play

of the object, which is used for previewing the thruster with low light mode before taking pictures to set up the experiment. The “Rec” button in live menu can be used for activating the trigger when everything is ready for taking picture. The only thing left for taking pictures is hitting the “trig” key on the function generator, then the “trig” button in live menu will be executed.

The playback menu may be used for reviewing the image saved in the camera. To get the desiring images, camera and record menus should be set properly. There are several options in the camera menu such as sensor gain, reset, rate, exposure, gamma, exposure mode and ROI as shown in Figure 56. Sensor gain is for selecting a gain value ranging from “-6 dB” to “+3 dB”. For this research “no gain” is employed throughout. The pulse event generates sufficient light for particle capture. If a device IO control error message appears, clicking the reset button may be helpful. The reset button restores the camera from the error condition. To select a new frame rate value, use the rate drop-down list. If the current exposure is too large for the selected rate, the program automatically adjusts it to an acceptable value. In this tab, the exposure time and f-stop values can be set. The ROI button is important to note again because of the relationship between the maximum frame rate of the camera and the number of rows in the ROI. In record menu, there are three record modes; normal, circular and Burst Record on Command (BROC). Normal mode records when the “Rec” button in live menu is set. The camera waits for “trig” button in live menu to complete the acquisition of the image in Circular and BROC modes. The difference between Circular and BROC is that memory is divided into sub-segments in BROC mode. The camera acquires images in a circular mode in sub-

segments. When the “trig” button is set, the camera completes the acquisition of images and starts acquiring in a specified sub-segment until the memory is filled. BROc mode is very useful if the trigger is supplied to the camera and thruster repeatedly. Initial attempts using BROc mode with the trigger set to 1.0 Hz did not provide the desired results.

When triggering the two cameras using BROc, one camera took one picture but the second camera took two images, providing a difference in the actual time of the different images. The cause was not identified but the speculation is that one camera is more sensitive than the other when receiving the signal from function generator trigger. The research employed the circular mode effectively, but did require researcher interaction, clicking the “Rec” button in live menu, “trig” button in function generator and saving it on the computer for every single shot. .

The frame option in the record menu is the number of frames to be recorded to the camera memory in a single acquisition. The values can be set from one up to a maximum number depending on the amount of free memory since single event captures occurred over millisecond time frame, most tests only capture 20 frames per event. In BROc mode, the number of frames is then further divided into each sub-segment. For instance, if the number of frames is set to 1000 and the BROc length is set to 100, the camera will acquire 10 sub-segments.

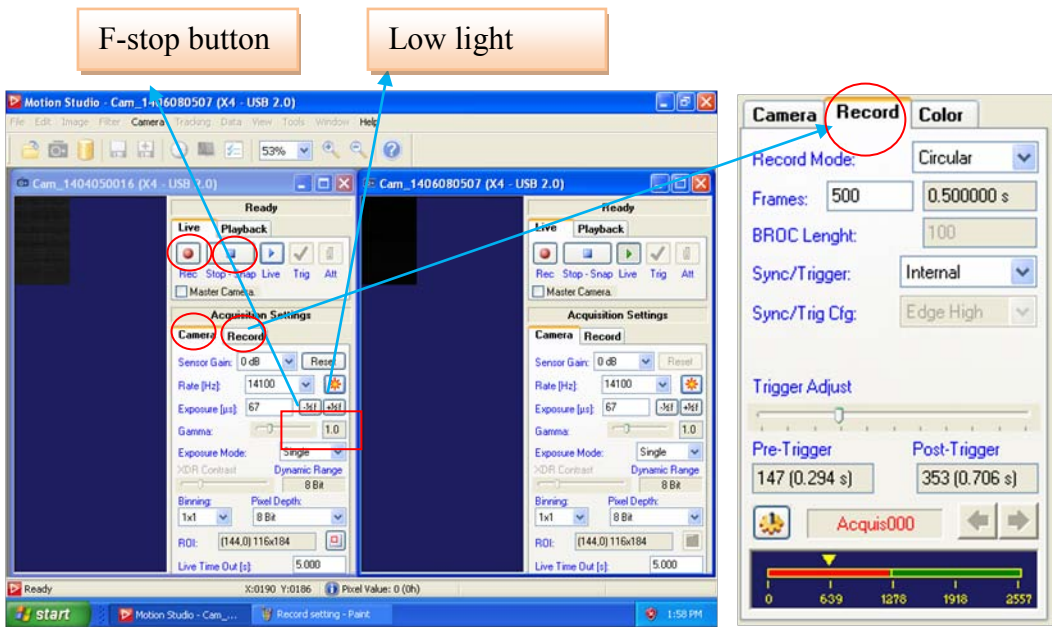
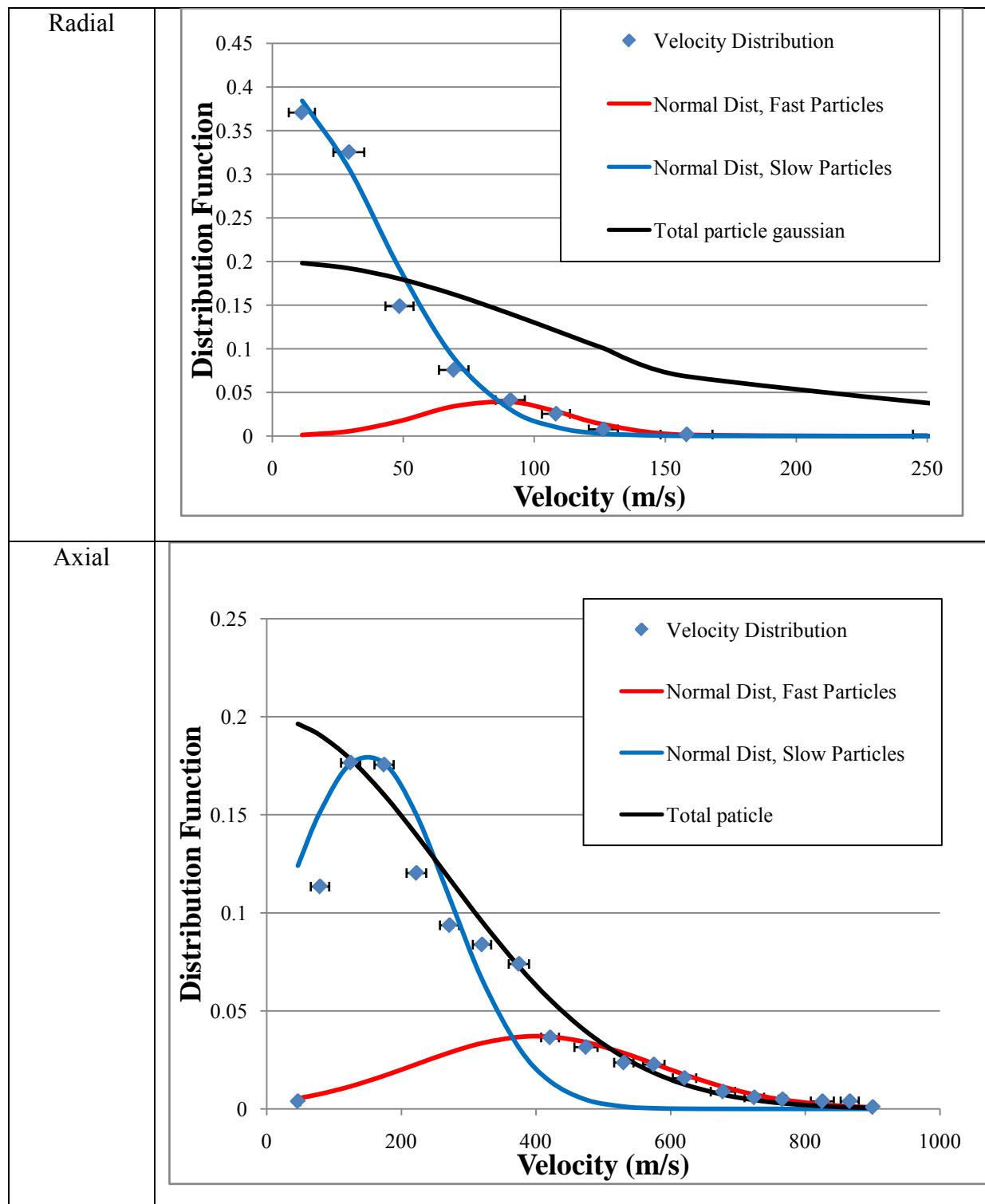


Figure 56: Screen after clicking the “open”

Appendix B: Velocity Distribution for Each Energy Level

5V (2.7 Joule)



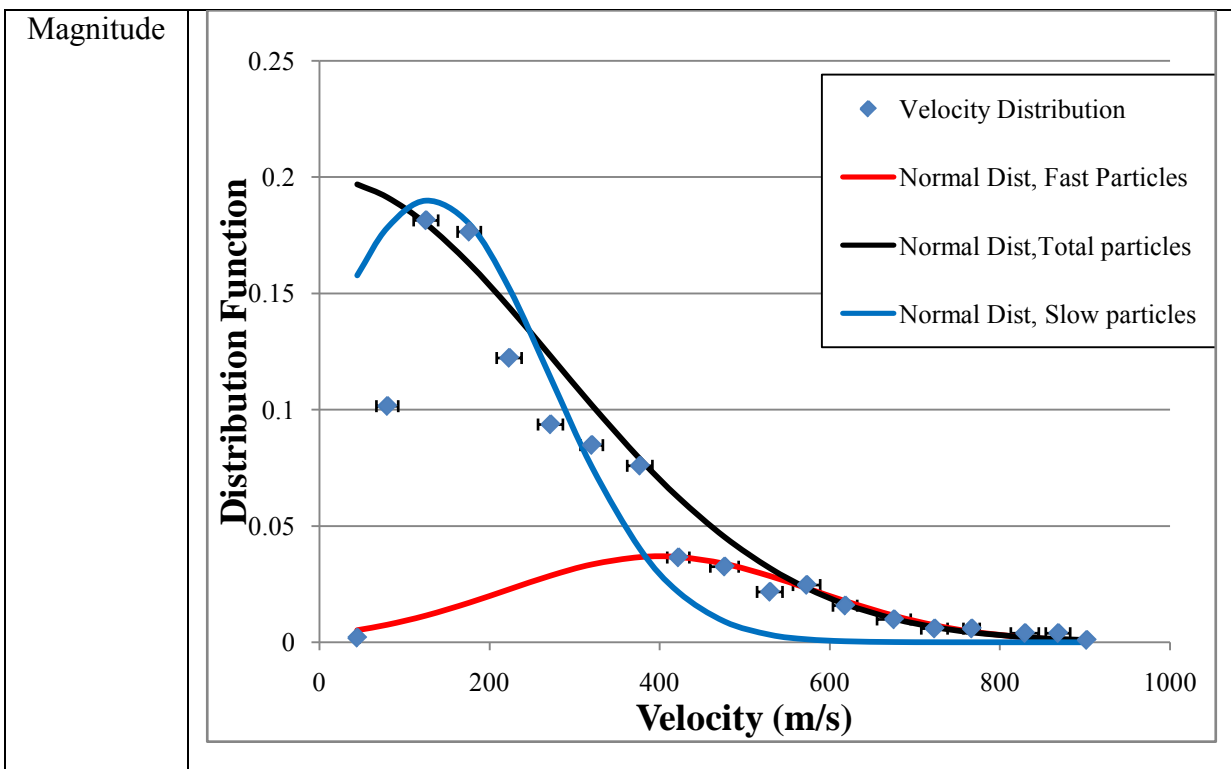
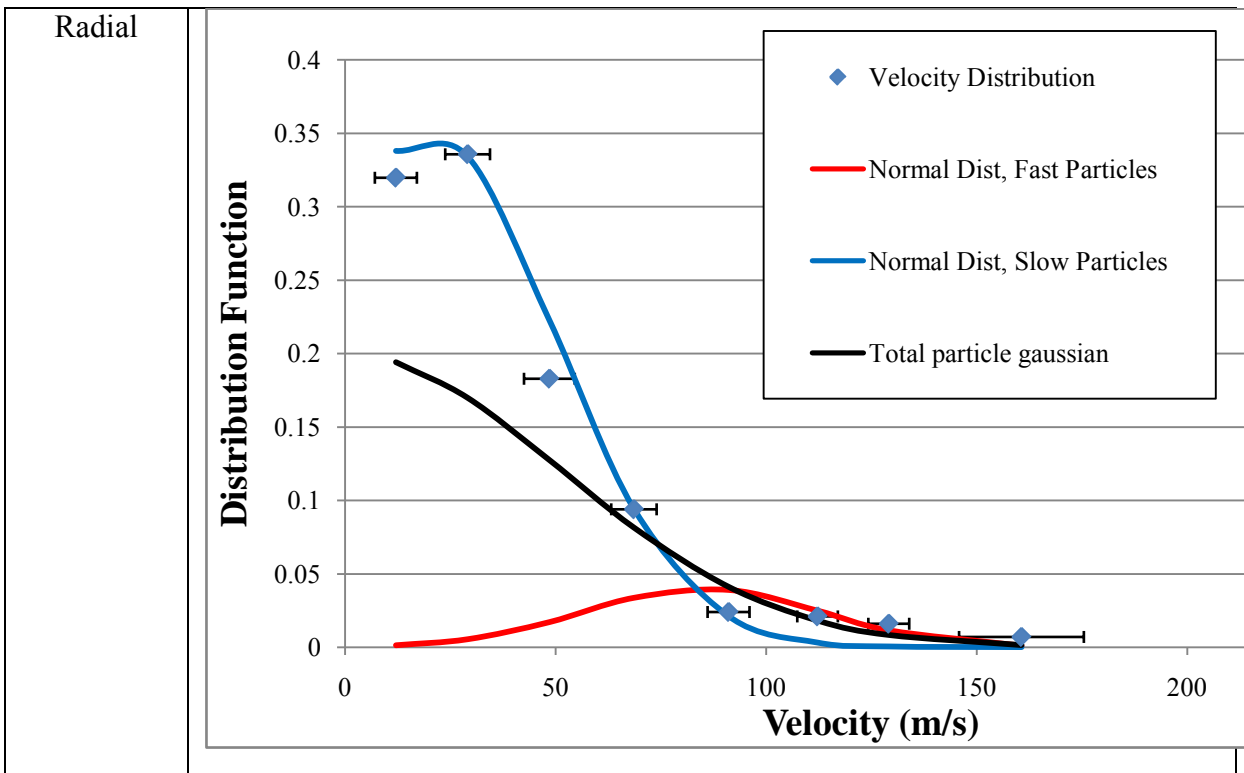


Figure 57 : Velocity Distribution for 5V (2.7 Joule)

6V (3.4 Joule)



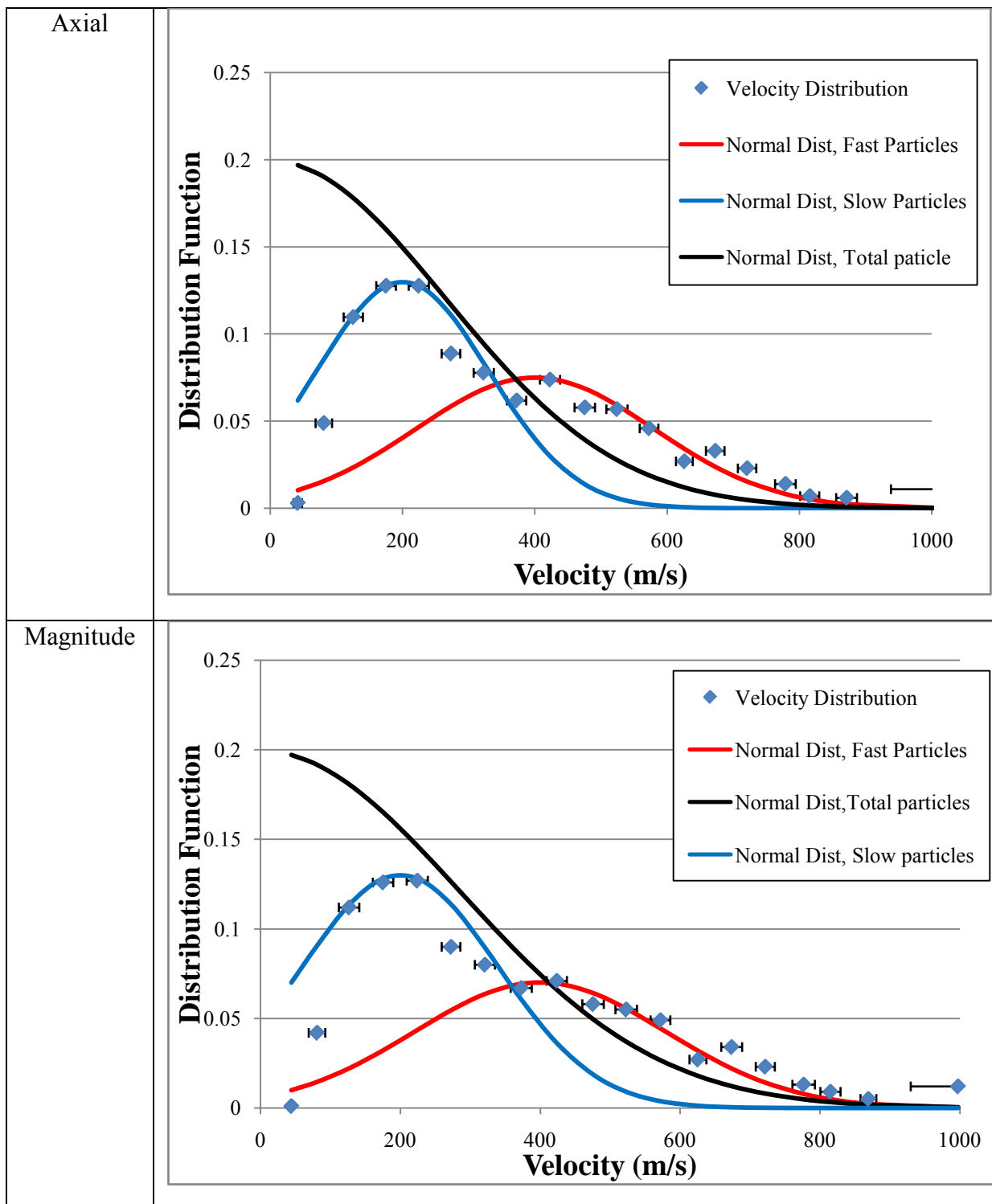
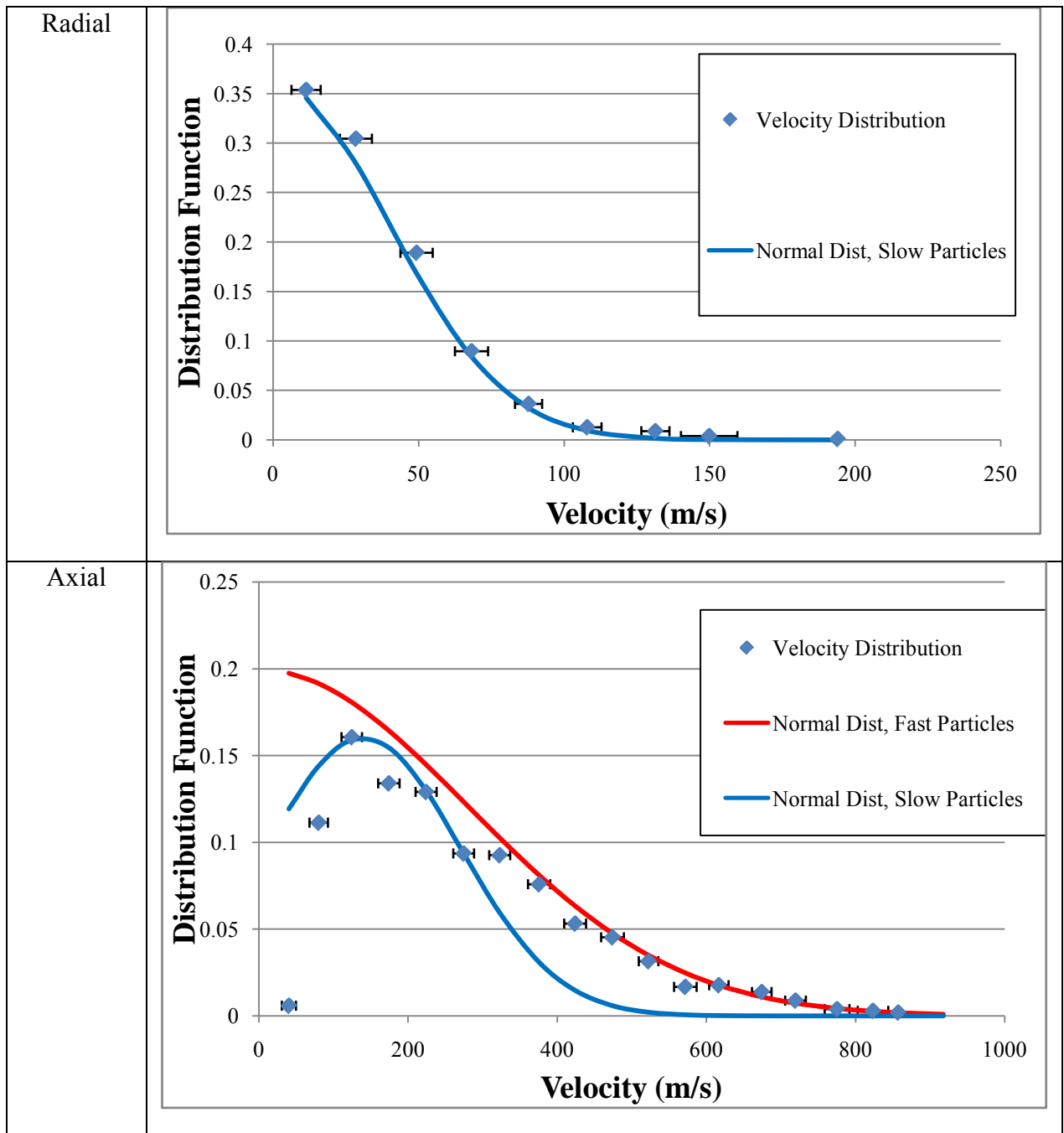


Figure 58 : Velocity Distribution for 6V (3.4 Joule)

7V (4 Joule)



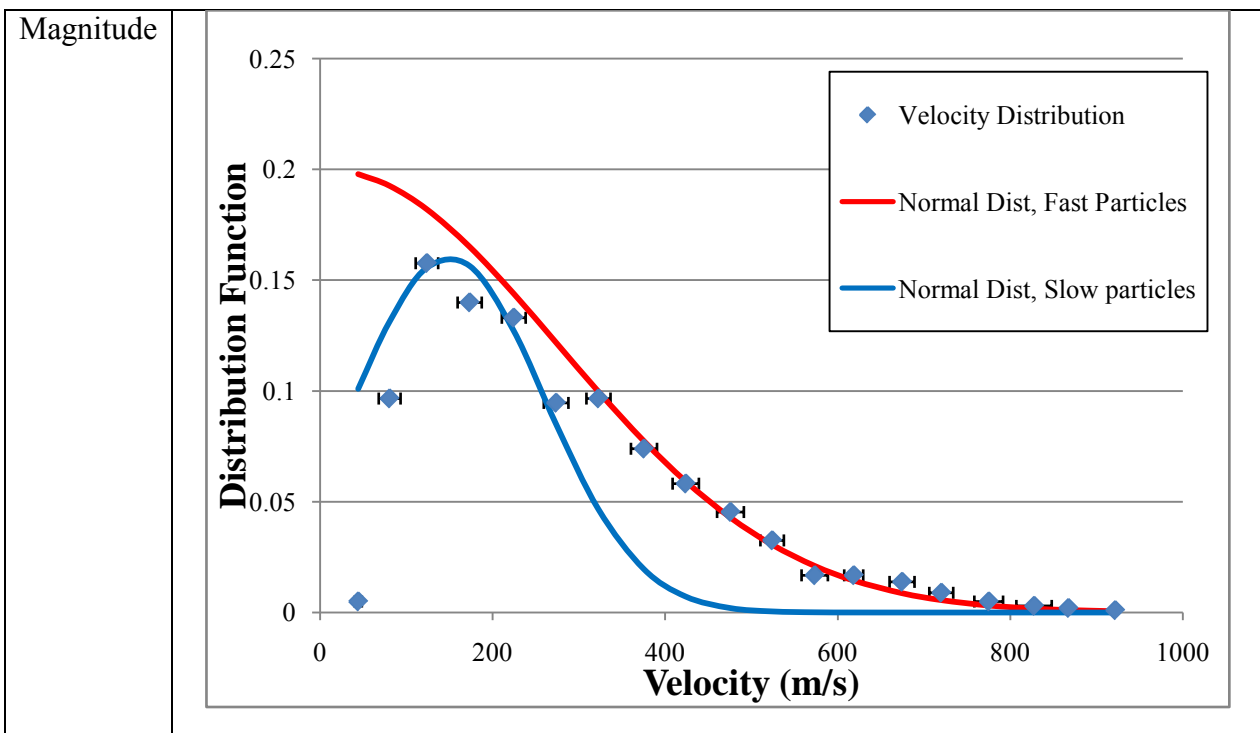
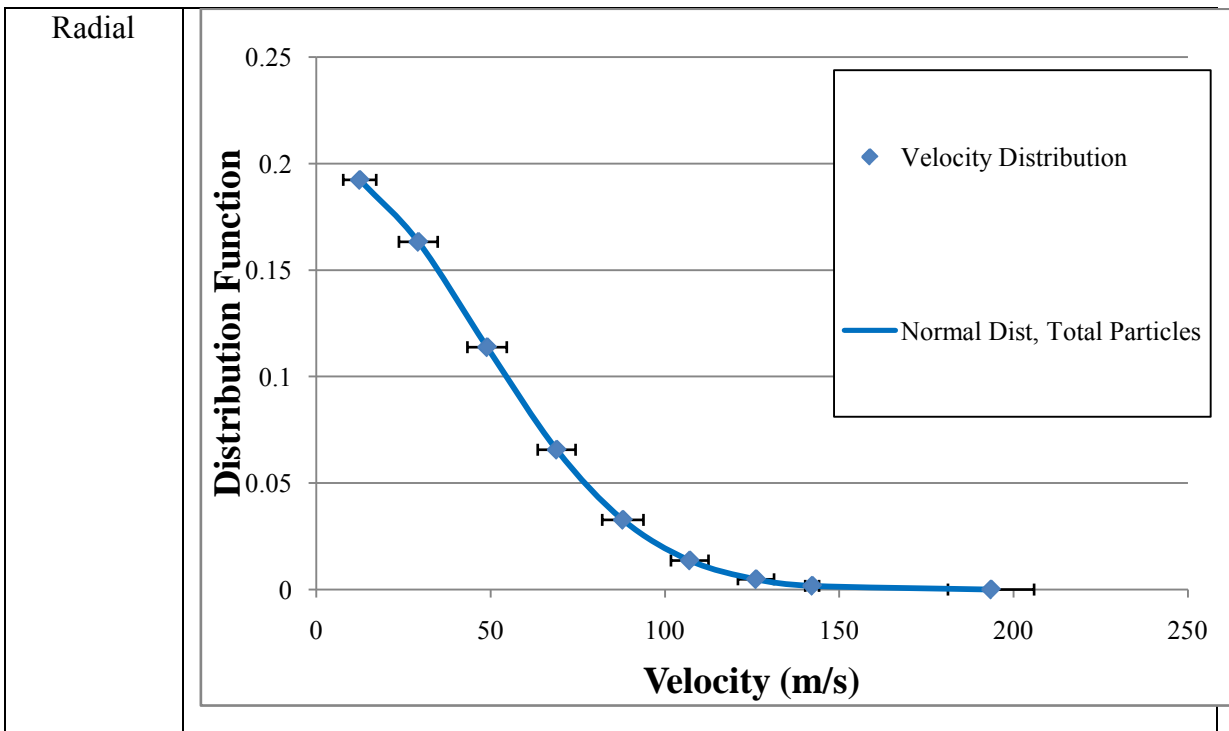


Figure 59 : Velocity Distribution for 7V (4 Joule)

8V (4.5 Joule)



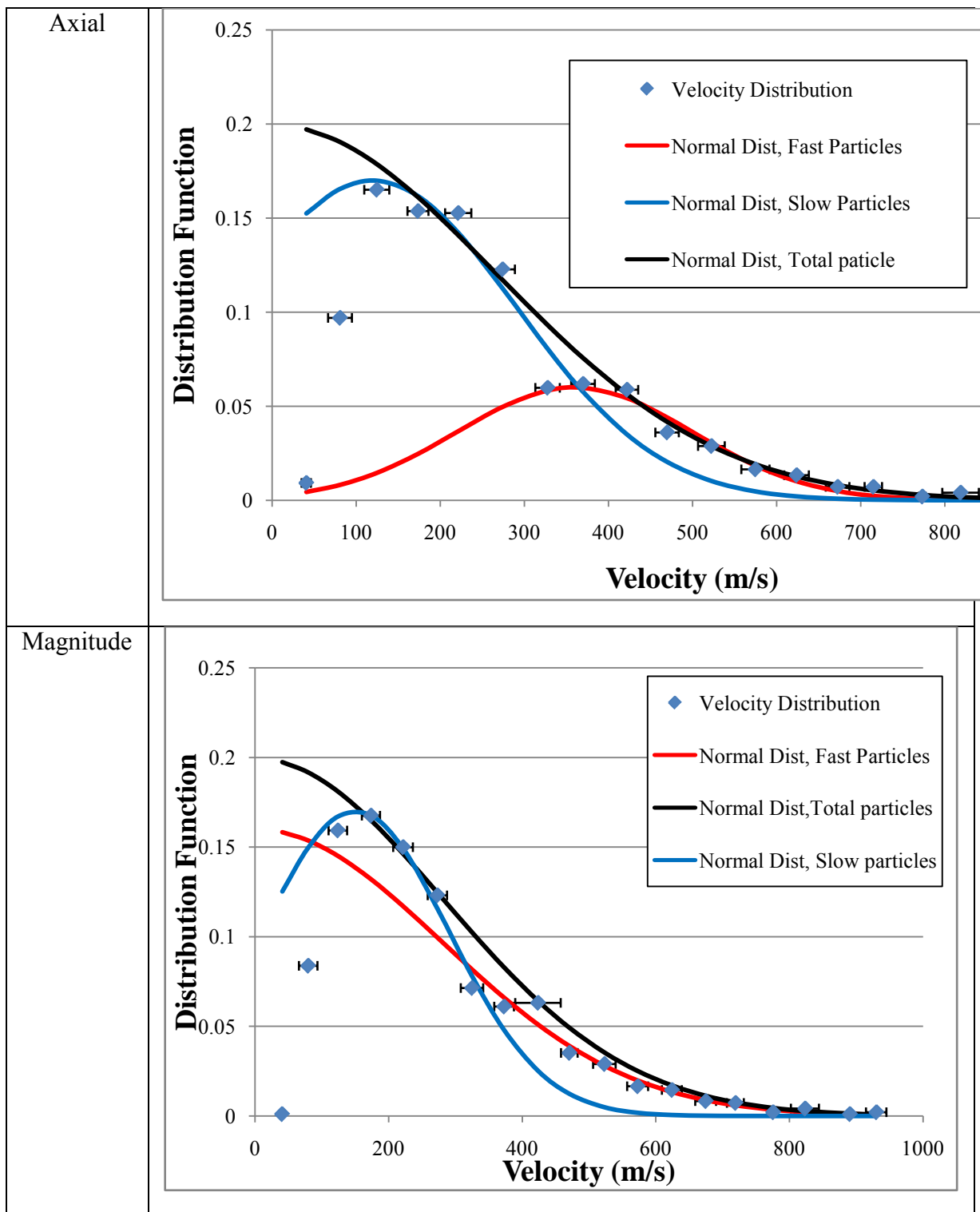
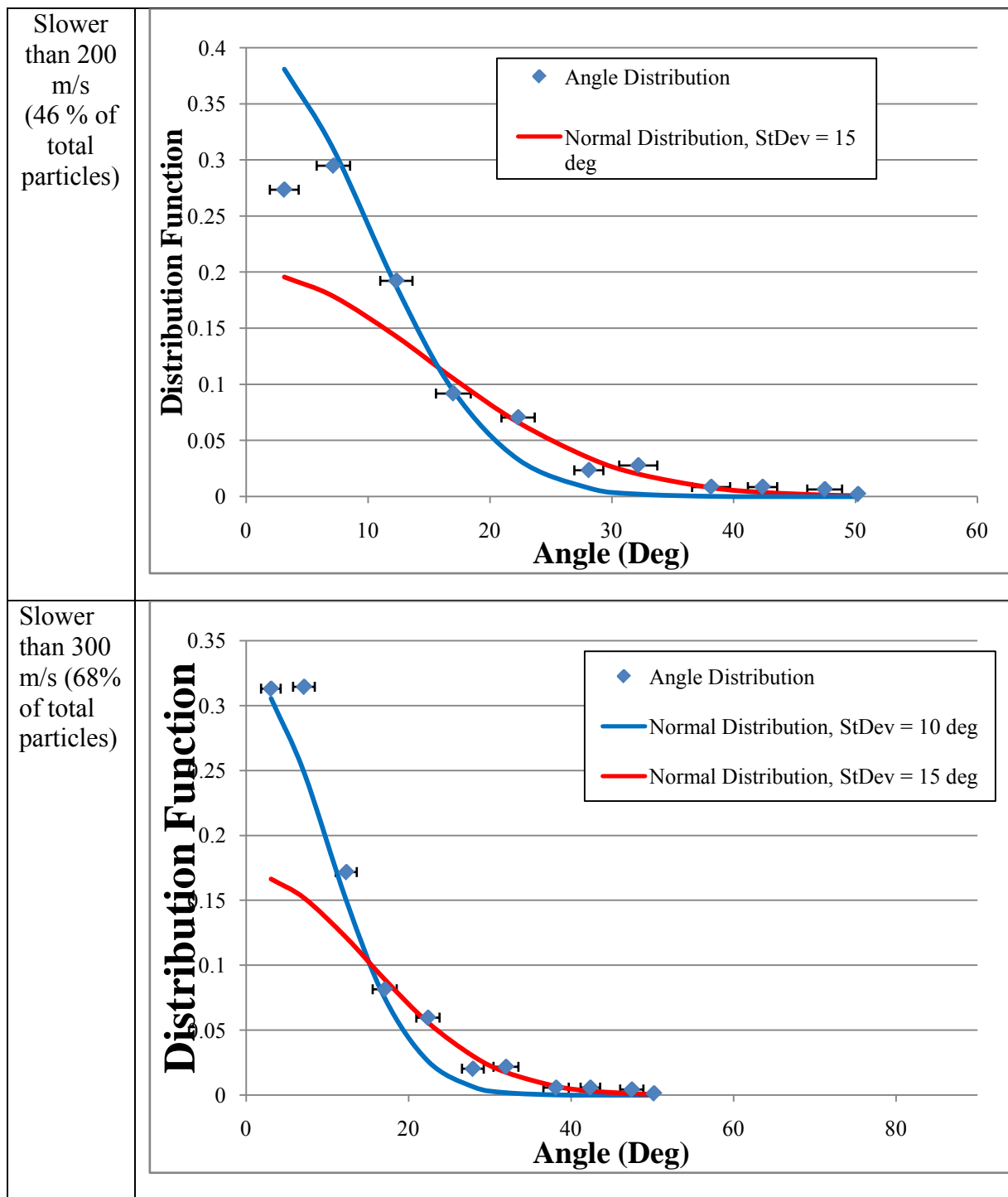


Figure 60 : Velocity Distribution for 8V (4.5 Joule)

Appendix C: Angle Distribution for Each Energy Level

5V (2.7 Joule)



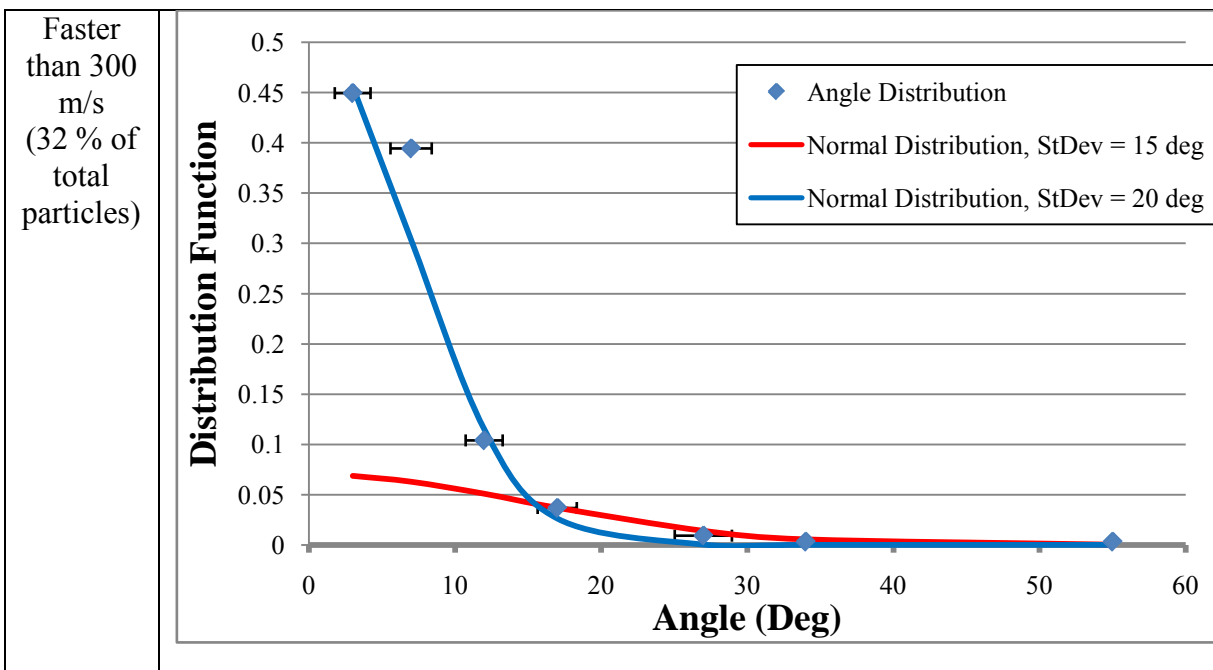
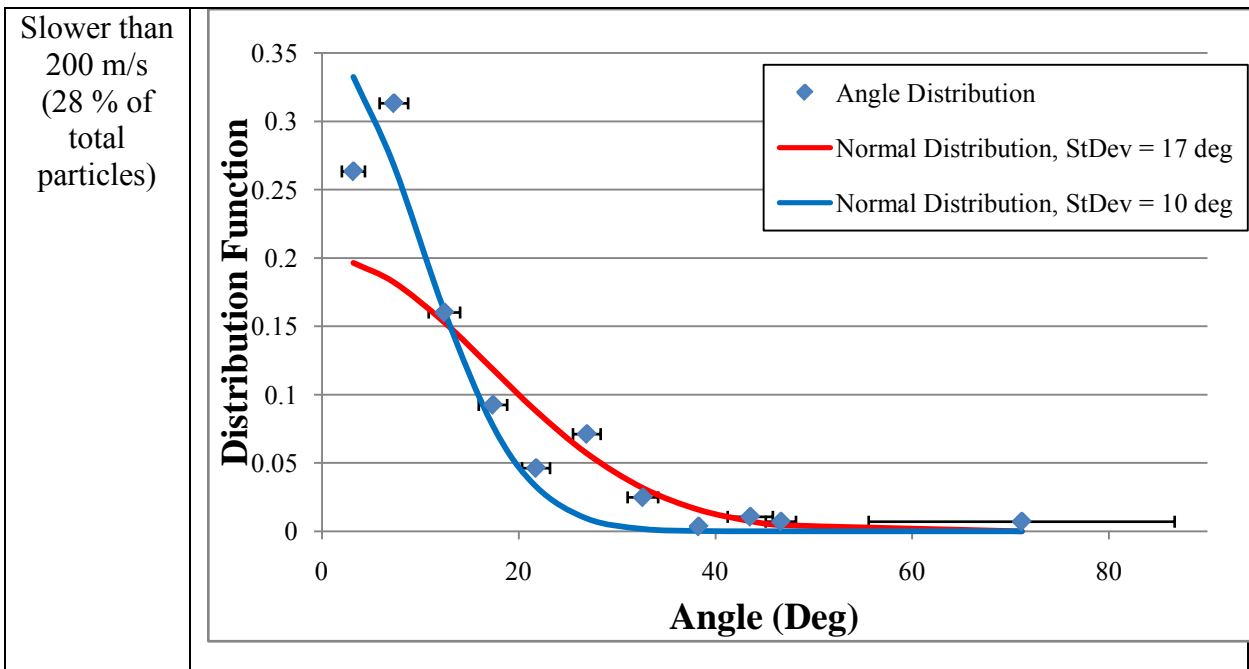


Figure 61 : Angle Distribution for 5V (2.7 Joule)

6V (3.4 Joule)



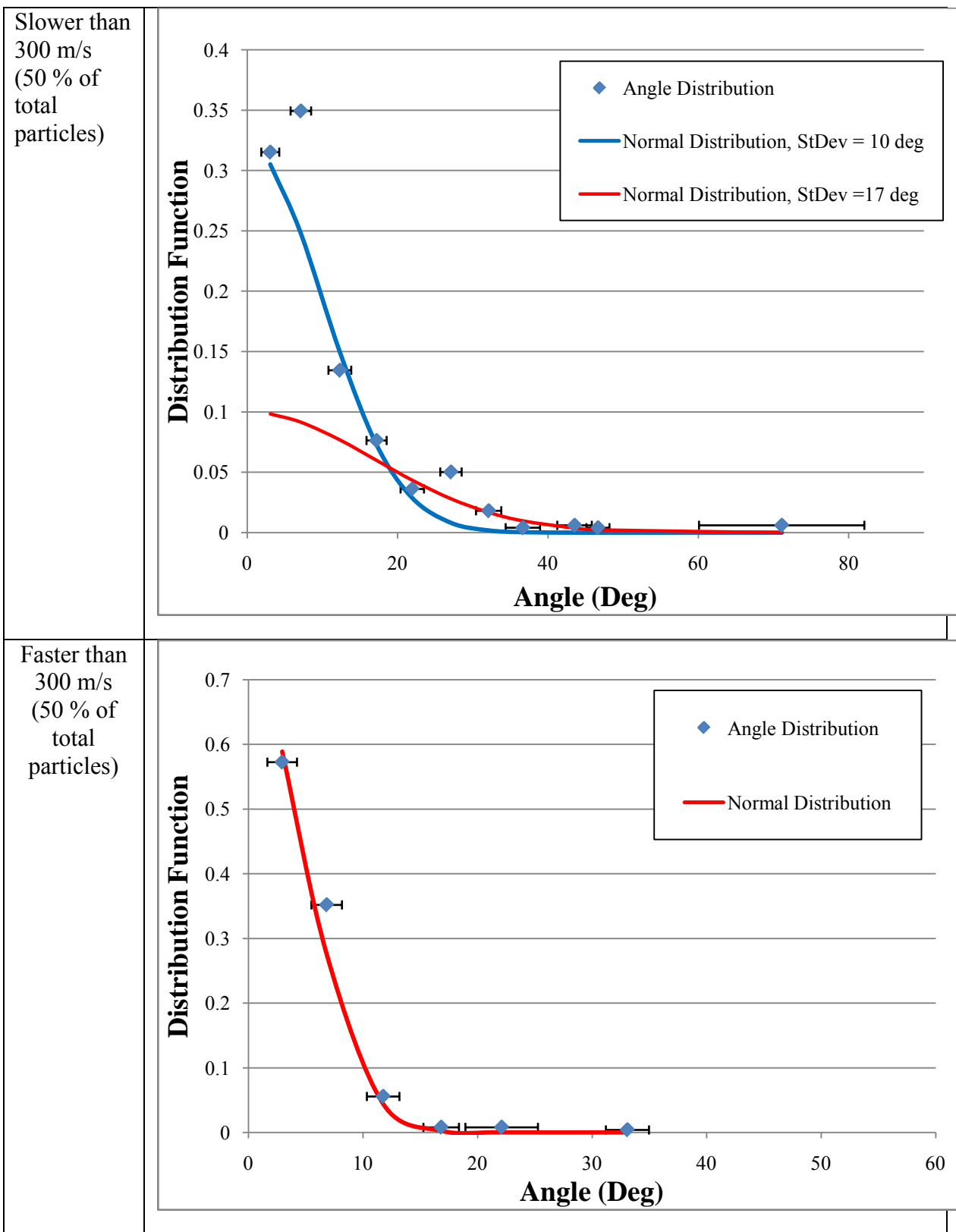
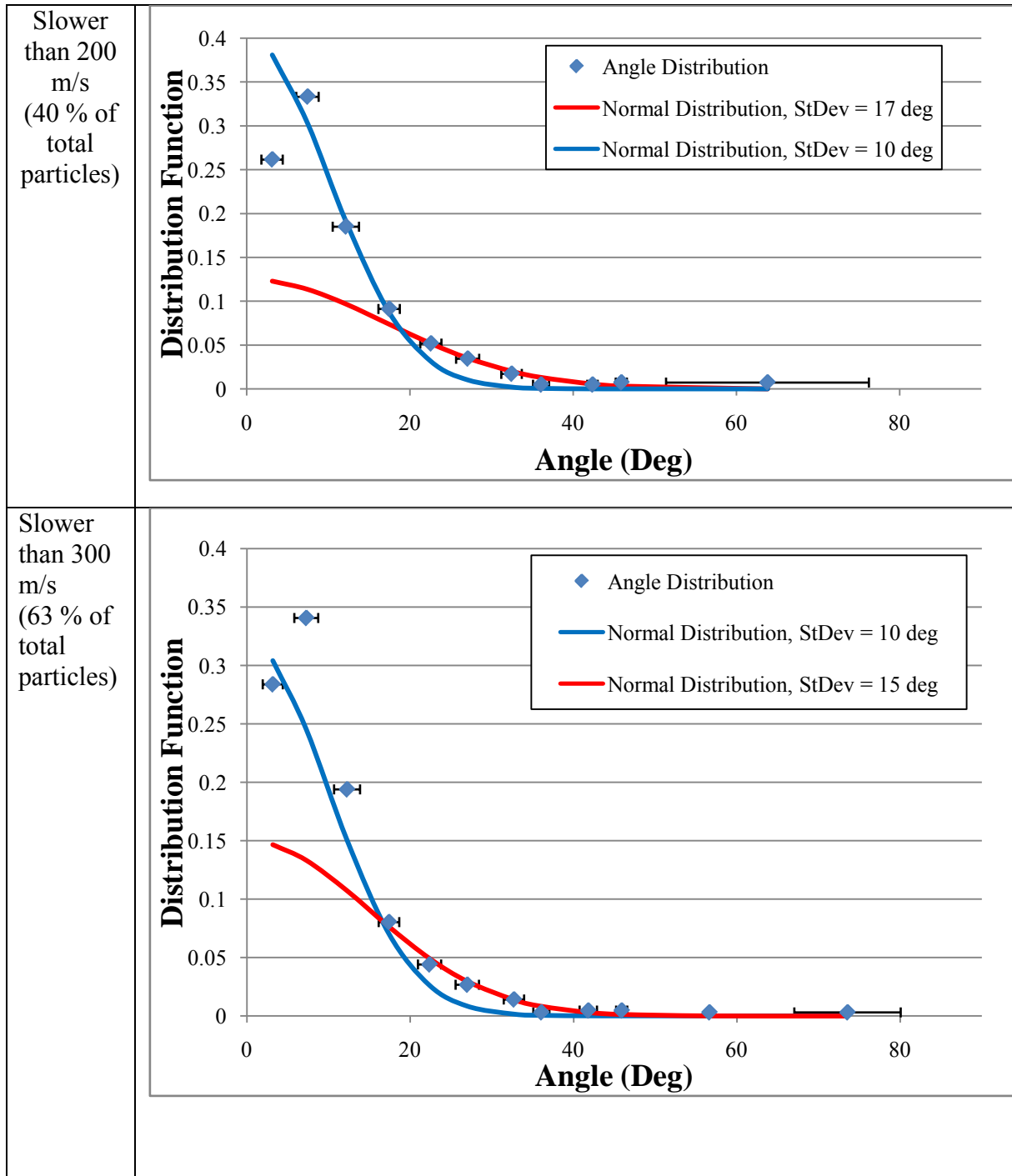


Figure 62 : Angle Distribution for 6V (3.4 Joule)

7V (4 Joule)



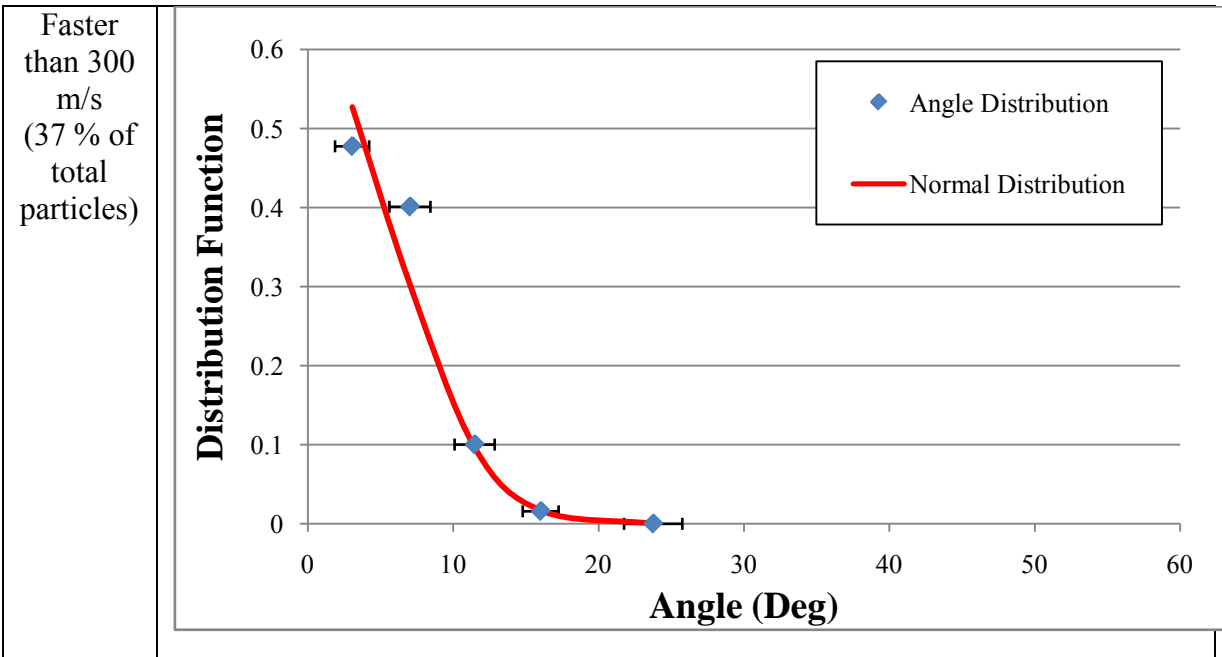
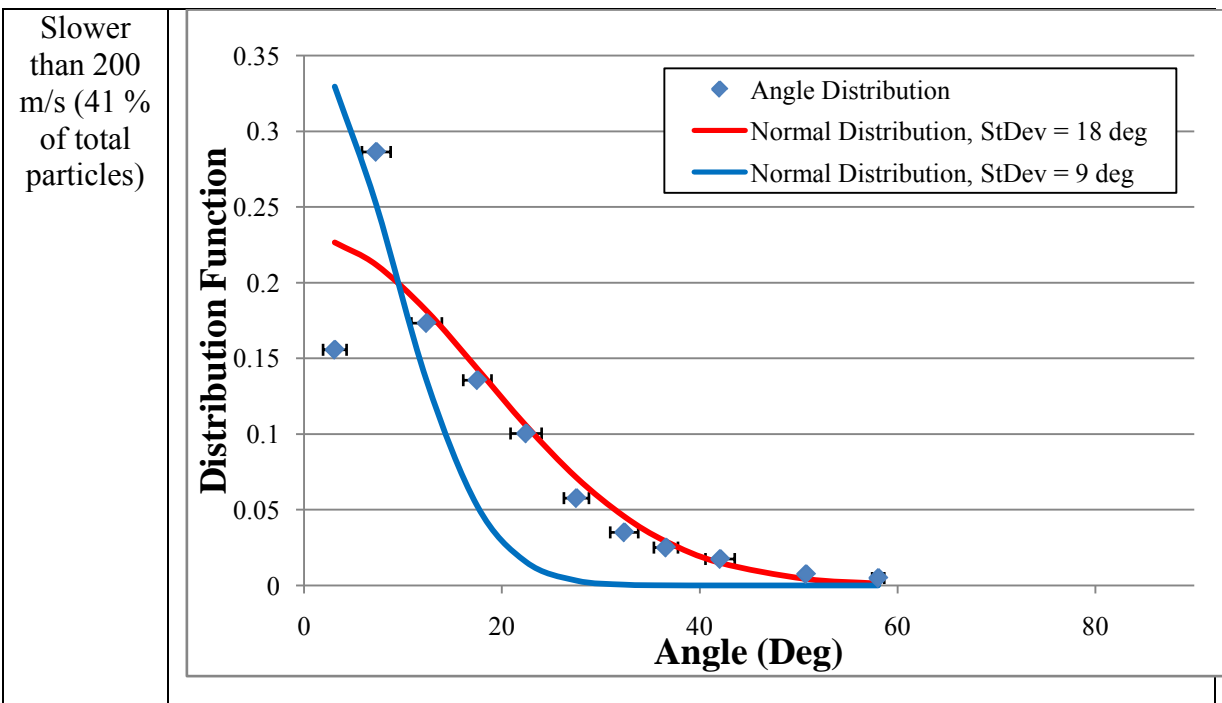


Figure 63 : Angle Distribution for 7V (4 Joule)

8V (4.5 Joule)



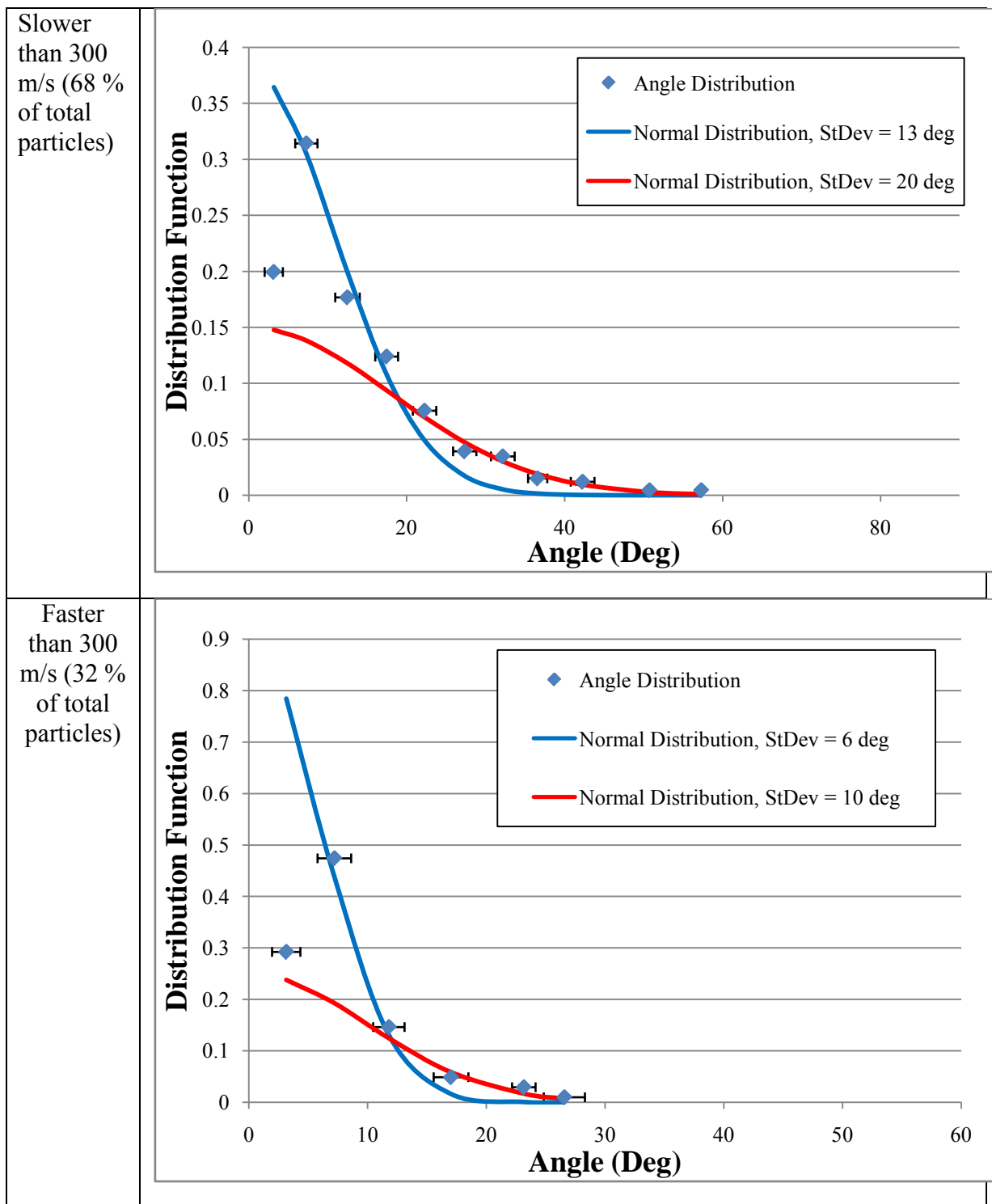


Figure 64 : Angle Distribution for 8V (4.5 Joule)

Vita

Captain Seo Myeongkyo graduated from R.O.K Air Force Academy in March 1998 with a Bachelor of Science degree in Aerospace Engineering. He was assigned to 36th TACG, Wonju Air Base as FAC (Forward Air Controller). In August 2007, he entered the Graduate School of Engineering and Management, Air Force Institute of Technology.

Bibliography

-
- ¹ Christopher D. Rayburn, Mark E. Campbell, and A. Thomas Mattick “Pulsed Plasma Thruster System for Microsatellites”, Journal Of Spacecraft And Rockets vol. 42, No. 1, January–February 2005
- ² Burton RL, Turchi P.J. “Pulsed Plasma Thruster”, J Prop Power 1998;14:716-35
- ³ W. Andrew Hoskins, Christopher Rayburn, and Charles Sarmiento” Pulsed Plasma Thruster Electromagnetic Compatibility: History, Theory, And The Flight Validation On Eo-1” 39th AIAA/ASME/SAE/ASEE Joint Propulsion Conference and Exhibit 20-23 July 2003, Huntsville, Alabama
- ⁴<http://www.busek.com>, Busek Co. Inc. 2007
- ⁵ Ronald W. Humble, Gary N. Henry, Wiley J. Larson, “Space propulsion analysis and design”, The McGraw-Hill Companies, Inc. 1995
- ⁶ R. Joseph Cassady, W. Andrew Hoskins, Mark Campbell and Christopher Raybum. “A Micro Pulsed Plasma Thruster (PPT) for the Dawgstar Spacecraft”, 2000
- ⁷ Gregory G. Spanjers, Daron R. Bromaghim, Capt. James Lake, Michael Dulligan.” AFRL MicroPPT Development for Small Spacecraft Propulsion”, 33rd Plasmadynamics and Lasers Conference 20-23 May 2002, Maui, Hawaii
- ⁸ Gregory G. Spanjers, Daron R. Bromaghim, Capt. James Lake, Michael Dulligan, David White, John H. Schilling, Stewart Bushman, Erik L. Antonsen, Rodney L. Burton, Michael Keidar, Iain D. Boyd. “AFRL MicroPPT Development for Small Spacecraft Propulsion”, 38th AIAA/ASME/SAE/ASEE Joint Propulsion Conference & Exhibit 7-10 July 2002, Indianapolis, Indiana
- ⁹ Bong Wie, David Murphy, “MicroPPT-Based Secondary/Backup ACS for a 160-m, 450-kg Solar Sail Spacecraft”, 41st AIAA/ASME/SAE/ASEE Joint Propulsion Conference & Exhibit 10 - 13 July 2005, Tucson, Arizona
- ¹⁰ Michael Keidar, Iain D. Boyd, Erik L. Antonsen, Rodney L. Burton, Gregory G. Spanjers, “Optimization Issues for a Micropulsed Plasma Thruster”, Journal Of Propulsion And Power Vol. 22, No. 1, January–February 2006
- ¹¹ Michael Keidar, Iain D. Boyd, Erik L. Antonsen, Gregory G. Spanjers, “Electromagnetic Effects in the Near-Field Plume Exhaust of a micro-Pulsed-Plasma Thruster”, Journal Of Propulsion And Power Vol. 20, No. 6, November–December 2004
- ¹² Sakir Tarsi, Richard D. Branam and Garrett Reed. ”Characterizing the Exhaust Plume of the Micro Pulsed Plasma Thrusters by High Speed Imagery”, Master’s Thesis, AFIT, 2007
- ¹³ Ceylan Kesene, Richard D Branam and Garrett Reed, “Contamination Study of micro-Pulsed Plasma Thrusters”, Master’s Thesis, AFIT, 2007
- ¹⁴ Adixen Vacuum Products Brochures and Technical Manuals
- ¹⁵ Agilent E3631A Triple Output DC Power Supply user guide, Agilent Technologies, Inc. 2000
- ¹⁶ High voltage power supplies, EMCO high voltage corporation. 2000
- ¹⁷ HV pulse model M10k-20 users manual, HV Pulse Technologies, Inc. 2007
- ¹⁸ Agilent 33120A Function Generator user’s guide, Agilent Technologies, Inc. 2000

¹⁹ Motion Studio Cross-platform User Manual

²⁰ IDT XS-4 Camera Brochure

²¹ Erwin Kreyszig, "Advanced Engineering Mathematics, 9th Edition", JOHN WILEY & SONS, INC.
2006

²² Michael Keidar and Iain D. Boyd, "Electromagnetic Effects in the Near Field Plume Exhaust of a Pulsed
Plasma Thruster", 37th AIAA/ASME/SAE/ASEE Joint Propulsion Conference and Exhibit, 8-11 July 2001

Salt Lake City, Utah

²³ W. A. Hoskins and R. J. Cassady, "Applications for Pulsed Plasma Thrusters and the Development of
Small PPTs for Microspacecraft", 36th AIAA/ASME/SAE/ASEE Joint Propulsion Conference and Exhibit
July 16-19, 2000 / Huntsville, Alabama

REPORT DOCUMENTATION PAGE			<i>Form Approved OMB No. 074-0188</i>
<p>The public reporting burden for this collection of information is estimated to average 1 hour per response, including the time for reviewing instructions, searching existing data sources, gathering and maintaining the data needed, and completing and reviewing the collection of information. Send comments regarding this burden estimate or any other aspect of the collection of information, including suggestions for reducing this burden to Department of Defense, Washington Headquarters Services, Directorate for Information Operations and Reports (0704-0188), 1215 Jefferson Davis Highway, Suite 1204, Arlington, VA 22202-4302. Respondents should be aware that notwithstanding any other provision of law, no person shall be subject to an penalty for failing to comply with a collection of information if it does not display a currently valid OMB control number.</p> <p>PLEASE DO NOT RETURN YOUR FORM TO THE ABOVE ADDRESS.</p>			
1. REPORT DATE (DD-MM-YYYY) 26 March 2009	2. REPORT TYPE Master's Thesis	3. DATES COVERED (From – To) October 2007 – March 2009	
4. TITLE AND SUBTITLE Characterizing The Exhaust Plume of The Three-Electrode Micro Pulsed Plasma Thrusters		5a. CONTRACT NUMBER	
		5b. GRANT NUMBER	
		5c. PROGRAM ELEMENT NUMBER	
6. AUTHOR(S) Seo, Myeongkyo, Capt. ROKAF		5d. PROJECT NUMBER	
		5e. TASK NUMBER	
		5f. WORK UNIT NUMBER	
7. PERFORMING ORGANIZATION NAMES(S) AND ADDRESS(S) Air Force Institute of Technology Graduate School of Engineering and Management (AFIT/EN) 2950 Hobson Way, Building 640 WPAFB OH 45433-8865		8. PERFORMING ORGANIZATION REPORT NUMBER AFIT/GSS/ENY/09-M07	
9. SPONSORING/MONITORING AGENCY NAME(S) AND ADDRESS(ES) Michael Huggins AFRL/RZS 4Draco Drive, Edwards AFB, CA 93524-7100 (phone : 661-275-5230)		10. SPONSOR/MONITOR'S ACRONYM(S) AFRL/RZS	
		11. SPONSOR/MONITOR'S REPORT NUMBER(S)	
12. DISTRIBUTION/AVAILABILITY STATEMENT APPROVED FOR PUBLIC RELEASE; DISTRIBUTION UNLIMITED.			
13. SUPPLEMENTARY NOTES			
14. ABSTRACT Three-electrode micro-PPTs are a new version of two electrode micro-PPTs devices. Performance predictions and contamination expectations are essential characteristics needed by satellite designers. In order to focus on thruster specific impulse, thrust and efficiency, measuring the exhaust velocity or impulse bit and propellant consumption rate is essential. While this is not always possible to measure directly, focusing on the ejected mass from the PPT provides significant information allowing determination of these performance statistics. Specifically, focusing on exhaust angle distribution and velocity of the exhaust particles is the emphasis of this work. The results show that the three-electrode micro-PPT is more reliable than two-electrode micro-PPT and the operating energy range from 2 to 4.5 Joule is proper value to operate it. This research also shows that the angle distribution is similar to previous mass deposition distributions and the faster particles have shallower angles than that of slower particles. Finally, the energy did not give appreciable effect on angle and velocity distributions and have the Isp value range from 25 to 36 sec from the average exit velocity.			
15. SUBJECT TERMS Three-electrode micro Pulsed Plasma Thruster(PPT), exhaust plume velocity, exit angle, contamination, high speed image			
16. SECURITY CLASSIFICATION OF:		17. LIMITATION OF ABSTRACT UU	18. NUMBER OF PAGES 115
a. REPORT U	b. ABSTRACT U	c. THIS PAGE U	19a. NAME OF RESPONSIBLE PERSON Richard Branam, LtCol, USAF
			19b. TELEPHONE NUMBER (Include area code) (937) 255-6565, ext 7485(Richard.Branam@afit.edu)

Standard Form 298 (Rev. 8-98)

Prescribed by ANSI Std. Z39-18